ISSN: 2591-7943

CHEMICAL REPORTS

VOLUME 1
ISSUE 1
JANUARY 2019

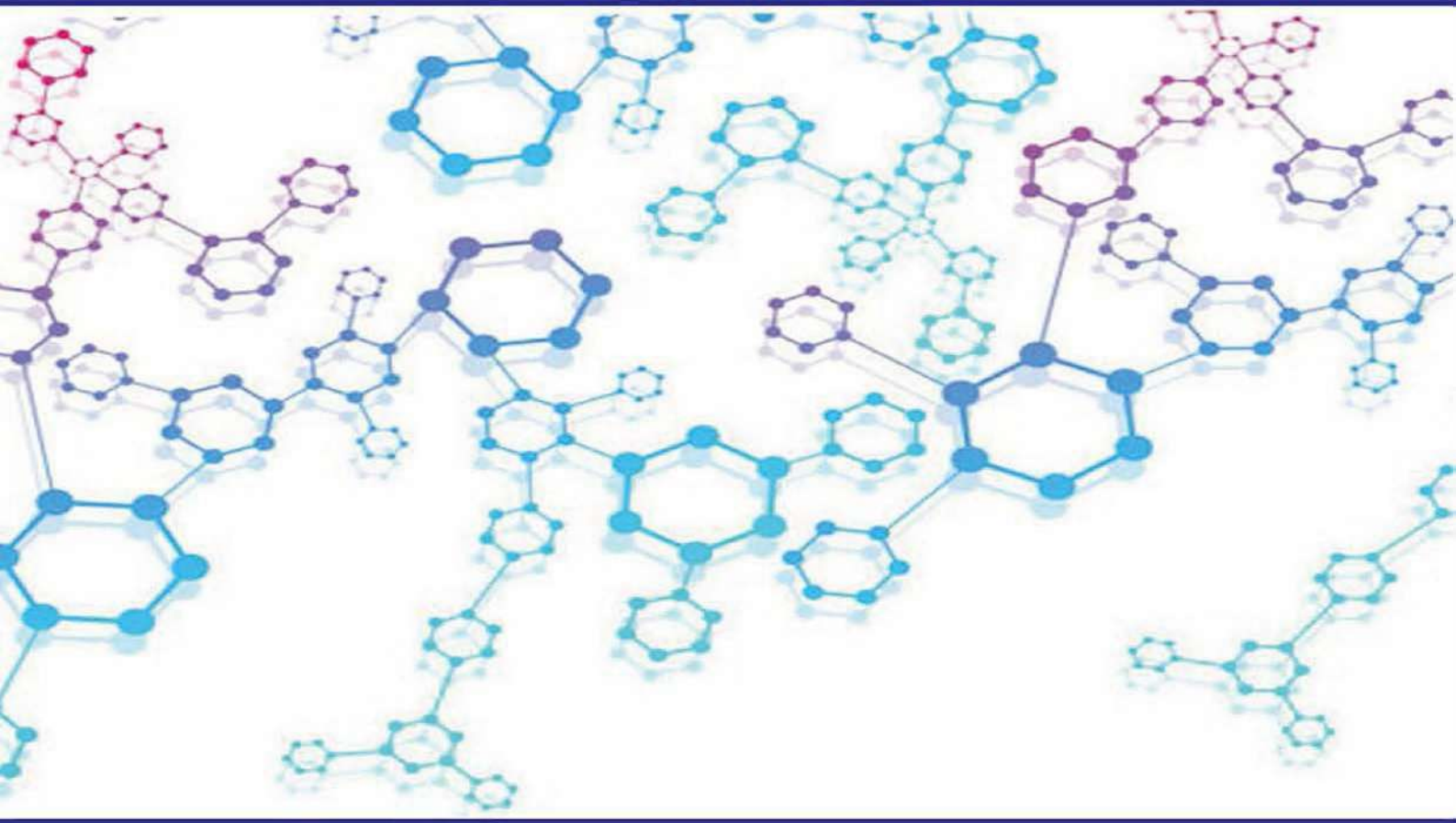

SyncSci PUBLISHING

Editorial Board

Editor-in-Chief

Editorial Board Members

Editorial Board Members

January 2019 | Volum 1 | Issue 1 | Page 1-50
http://www.syncsci.com/journal/index.php/CR

Chemical Reports

Contents

Chem Rep, 2018, 1(1), 1−2
DOI: 10.25082/CR.2018.01.001

EDITORIAL

New Trends in Nano−Engineering

Editor-in-Chief: Raffaele Barretta

With rapid developments of nano-engineering in the recent years, high-performance and multi-functional nano-materials, exhibiting new and enhanced physical and chemical properties, are introduced with innumerable conceivable applications. The recent advances in design, synthesis and characterization techniques of nano-materials have enabled the fabrication of modern nano-electro-mechanical systems (NEMS). Research breakthroughs in NEMS technology over the past decade have caused an increased interest in the analysis of structures at nano-scale, stimulated by the fact that control over these exclusive properties leads to development of concepts potentially resulting in new engineering applications.

Nanomaterials, such as carbon nanotubes and graphene sheets, have also attracted emergent interest since the isolation of graphene due to their exclusive structural, chemical and electronic properties and their astonishing competences in sensing and bio-sensing, energy conversion and storage and bio-medical applications. Nanomaterials can be also efficiently exploited as excellent components for reinforcement in nano-composites.

It is well established that nanostructures have discrete nature manifested in the form of atoms and interactions between atoms so that classical continuum mechanics can have limited success in describing size effects. The research community of engineering science has been vigorously trying to capture the size-dependent behaviour employing nonlocal elasticity theories, among other generalized continuum mechanics approaches.

Chemical Reports is an international research journal and invites contributions of original and new fundamental research. The journal aims at providing an international forum for the presentation of high-quality and rigorous research, interpretative reviews and discussion of original developments in chemical and mechanical engineering. Papers describing innovative theoretical proposals and new numerical methodologies and applications in nano-engineering are most welcome, such as those which demonstrate the transfer of techniques from other disciplines. Reports of carefully executed experiments, which are soundly interpreted, are also welcome.

The main aim of Chemical Reports is to generate bridges between the most innova-

Received: July 12, 2018; **Accepted:** July 13, 2018; **Published:** July 16, 2018

Correspondence to: Raffaele Barretta, Department of Structures for Engineering and Architecture, University of Naples Federico II, Italy; Email: rabarret@unina.it

Citation: Barretta R. New Trends in Nano−Engineering. *Chem Rep*, 2018, **1**(1):1−2

tive scientific developments and their potential applications in the fields of chemical and mechanical engineering applicable to nano-materials and nano-structures.

Potential topics of interest include but are not limited to the following:

- Chemical engineering
- Chemical technology
- Biochemical engineering and technology
- Green Chemistry
- Chemicals synthesis and process
- Chemicals structure
- Thermodynamics
- Reaction and catalysis
- Nanotechnology
- Chemical optimization
- Mechanics of nanostructures
- NEMS problems
- Nonlocal elasticity

Chem Rep, 2019, 1(1): 3-12
DOI: 10.25082/CR.2019.01.001

RESEARCH ARTICLE

A controlled, efficient and robust process for the synthesis of an epidermal growth factor receptor inhibitor: Afatinib Dimaleate

Pawan Kumar[1*] Premnath Dhande[1] Muhammad Taufiq F. Mazlee[1] Suhaila M. Yaman[1]
Nurul Syazwani Nadirah Binti Muhammad Syafiq Chandran[1] Mohd Zulfadli Bin Makhtar[1]
Dhramveer Singh Shekhawat[1] Sunil Vasudeorao Lanke[1] Ramesh Kumar[1] Sandeep Mhetre[1]

Abstract: A simple, controlled, robust and scalable three-stage manufacturing process of Afatinib Dimaleate was assessed and optimized leading to improved yield and quality. The synthetic process involves sequence of reactions as nitro-reduction, amidation and salification. The developed and optimized route was demonstrated on 300 g scale with over all isolated yield of 84% for Afatinib free base. The developed process has the capability to control not only the process related impurities but also the degradation impurities. One new impurity was identified during the process development studies and characterized as acetamide impunity, chemically known as (S)-N-(4-((3-chloro-4-fluorophenyl) amino)-7-((tetrahydrofuran-3-yl) oxy) quinazolin-6-yl) acetamide. Other impurities were identified as degradation impurities, Process impurities and were labeled as 1-(4-((3-chloro-4-fluorophenyl) amino)-7-(((S)-tetrahydrofuran-3-yl) oxy) quinazoline-6-yl)-5-Hydroxypyrrolidin-2-one (hydroxy impurity), Afatinib N-Oxide impurity and N4-(3-chloro-4-fluorophenyl)-7-[[(3S)-tetrahydro-3-furanyl] oxy]-4,6-quinazolinediamine (Intermediate-1).

Keywords: Afatinib Dimaleate, HPLC, degradation impurities, NMR, LC-MS, new process impurity, improved process

1 Introduction

Over the years many quinazoline derivatives were reported as epidermal growth factor receptor (EGFR) signal transduction pathway inhibitors and Afatinib Dimaleate[1] is one of them which is powerful, irreversible tyrosine kinase inhibitor of EGFR, with IC50 value (half-maximal inhibitory concentration) of 0.5nM, exhibits potent anti-tumor activity against non-small cell lung cancer (NSCLC) (https://www.medchemexpress.com). Afatinib [BIBW 2992; *N*- [4-[(3-chloro-4-fluorophenyl) amino]-7-[[(3*S*)-tetrahydro-3-furanyl]oxy]-6-quinazolinyl]-4-(dimethylamino)-2-butenamide] is an ATP-competitive anilinoquinazoline derivative harboring a reactive acrylamide group.[2–4] Afatinib Dimaleate is approved by the FDA as a first line

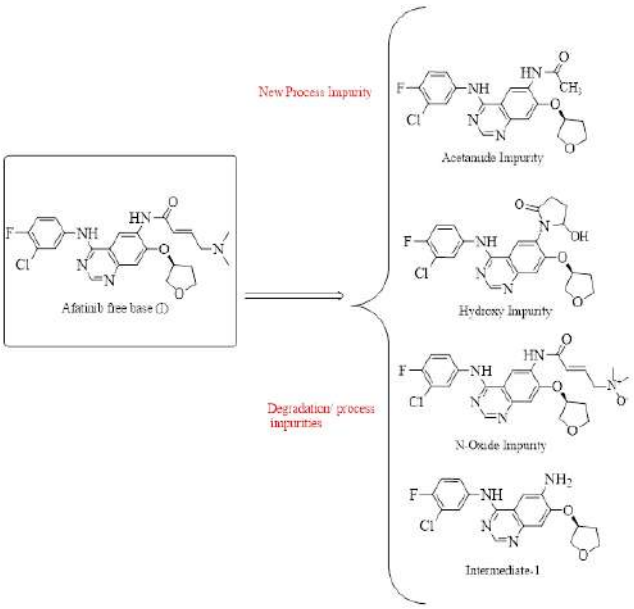

Figure 1. Graphicla abstract

Key features of the article:
1. Improved process for the synthesis of Afatinib Dimaleate.
2. Identification, synthesis and characterization of one new process impurity by NMR, LC-MS and HPLC.
3. Forced degradation studies as per ICH guidelines to have control on process impurities.
4. Developed HPLC method which is highly sensitive, specific, selective and robust for analysis.

Received: January 9, 2019 **Accepted:** January 30, 2019 **Published:** February 4, 2019

* **Correspondence to**: Pawan Kumar, Oncogen Pharma Sdn Bhd, No.3, Jalan Jururancang U1/21, Hicom Glenmarie Industrial Park, 40150 Shah Alam, Selangor, Malaysia; Email: pawan.kumar@oncogenpharma.com
[1] Oncogen Pharma Sdn Bhd, No.3, Jalan Jururancang U1/21, Hicom Glenmarie Industrial Park, 40150 Shah Alam, Selangor, Malaysia.

Citation: Kumar P, Dhande P, Mazlee MTF, *et al.* A controlled, efficient and robust process for the synthesis of an epidermal growth factor receptor inhibitor: Afatinib Dimaleate. *Chem Rep*, 2019, **1**(1):3-12.

treatment of patients detected with metastatic non-small cell lung cancer (NSCLC) with common epidermal growth factor receptor (EFGR) mutations as detected by an FDA-approved tests (Gilotrif FDA Label). It was designed to covalently bind and irreversibly block enzymatically active ErbB receptor family members.[5]

As per prior art methods very few synthetic procedures are reported for Afatinib Dimaleate and none of process has discussed clearly about the process impurities and their control measures.[6] Impurities in active pharmaceutical ingredient (API) are highly undesirable and in some cases can prove to be harmful to the patient. The International Conference on Harmonisation of Technical Requirements for Registration of Pharmaceuticals for Human Use (ICH) Q7 is a guidance for API manufacturers, mentions that impurities to be maintained below set limits.[7] Thus, it is pertinent to identify and characterize the impurities in API to develop suitable process where in their levels can be kept within permissible limits (FDA guidelines for good manufacturing practices for API). The impurity profile study should be carried out for any bulk drug to identify and characterize all the unknown impurities that are present at a level of above 0.05%. A comprehensive study has been undertaken to isolate and characterize these impurities by spectroscopic techniques. This research article describes the improved process for the synthesis of Afatinib Dimaleate, identification, isolation, synthesis and characterization of impurities that are present in the range of 0.08%-0.30% by area percent in the Afatinib Dimaleate.

During the analysis of laboratory batches of Afatinib Dimaleate by high performance liquid chromatography (HPLC) four different and major impurities were observed, one of them was identified as new process impurity, two of them as major degradant impurities and one of them as both process impurity or degradation impurity. The impurities were in the range of 0.08-0.30% along with drug substance. In regulatory terms, the level of impurities in drug substance is quite important for the drug approval and can show a significant impact on the quality and safety of drug. Thus, impurity profiling is the most concerning task in the modern pharmaceutical analysis especially when it comes to oncology drugs.[8]

None of processes reported in the prior art has explained the controlled measures for the listed impurities. Based on these views, our focus was to develop a highly effective, optimized and efficient process which should have all the control measures for these impurities, synthesize and characterize the new impurity and to control the degradation impurities in the drug substance. The structure of new impurity was presumed based on the liquid chromatograph-mass spectrometer (LC-MS)/MS data and confirmed its synthesis followed by spectroscopic analysis such as ^{1}H NMR, ^{13}C NMR, mass and IR. In addition to this, an effective and sensitive HPLC method was developed to separate and quantify all the related substance of Afatinib Dimaleate. To our knowledge this is the first study that comprehensive analysis of the potential impurities and degradation products in Afatinib Dimaleate has been done, including their synthesis and characterization.

2 Experimental

2.1 Chemicals and Reagents

The Afatinib Dimaleate was used from in-house sources as synthesized in Chemical Research and Development laboratory of Oncogen Pharma (Malaysia) Sdn Bhd. HPLC grade methanol, acetonitrile, OPA (85%), TEA and other chemical reagents were purchased from Merck & JT Baker. The solvent N, N-dimethylacetamide from sigma Aldrich (with appropriate specification). Milli-Q-Purified water by Milli-Q plus purification system from Millipore (Bradford, USA), was used during experimental studies. The process used deoxygenated water which was generated by purging nitrogen gas in the Milli-Q-water for 3 h. All the general chemicals were brought either from Merck Sdn Bhd., Malaysia or local chemical supplier. Solvents from Polyscientific Enterprise Sdn. Bhd. Malaysia. IR spectra were recorded with KBr pellets using Shimadzu FTIR Tracer-100 spectrophotometer, ^{1}HNMR and ^{13}CNMR were recorded in solvents $CDCl_3$, DMSO-d_6 and CD_3OD at 300MHz and 75MHz respectively using Bruker instrument. All the chemical shift values are reported in δ units downfield from TMS as internal standard. Differential scanning calorimetry (DSC) were performed using T. A. instrument model no. DSCQ20. X-Ray Diffraction pattern (XRD) analysis were performed using PANalytical instrument model no. Empyrean. Melting point were recorded using BUCHI melting point apparatus with model no. M-565.

2.2 Prior art method for the synthesis of Afatinib Dimaleate

The prior art method[9,10] for the synthesis of Afatinib Dimaleate involves the series of reaction wherein the compound 4-[(3-chloro-4-fluorphenyl) amino]-6-nitro-7-fluoro quinazoline **5**, was used as a starting material, substitution reaction of **5** with S-(3)-hydroxy tetrahydrofuran 6, in the presence of catalytical amount of potassium tert. butoxide resulted in 4-[(3-chloro-4-fluorophenyl) amino]-6-nitro-7-(S) -(tetrahydrofuran-3-

yl) oxy] quinazoline **7**, which on reduction at 6^{th} position of nitro group to resulted in corresponding amine **8**. which reacts with bromo crotonyl chloride to get intermediate **9**. Amination reaction of the **9** with dimethylamine affords Afatinib free base **2**. The entire reaction sequence is depicted below Figure 2.

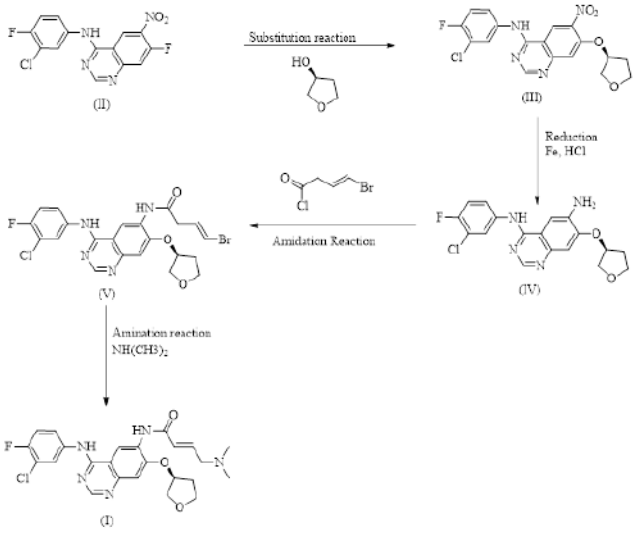

Figure 2. Prior art scheme

2.3 Synthetic Process for Afatinib Dimaleate

Synthesis of Afatinib Dimaleate was followed as per the scheme shown below:

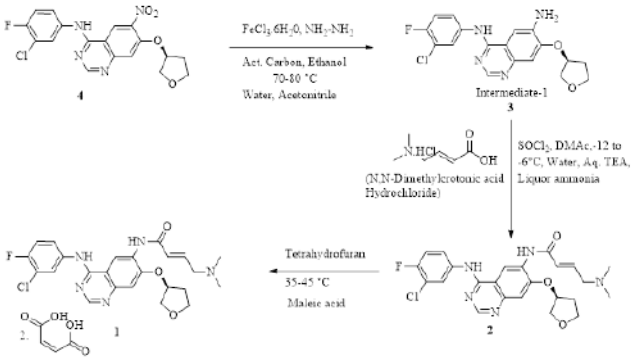

Figure 3. Synthetic scheme for Afatinib Dimaleate

2.4 Forced Degradation (FD) studies

Based the FD data it was easy to identify the possible degradants and their conditions and thus it became easy to establish their control measure in the process. The HPLC purity of control sample used for the study was 99.94% with impurities at about RRT 0.44 (0.01%), 0.50 (0.03%) and 0.81 (0.01%). All the FD study performed is summarized below as:

2.5 Oxidative Degradation

The Afatinib Dimaleate was treated with 5% hydrogen peroxide solution for 2 h at 70 °C. Few unknown peaks were observed at different RRT's with area percent ranging from 1.6% to 3.17%. During the laboratory development batches, one impurity at about RRT 0.49 was in concordant with impurity observed during oxidative degradation. Thus, based on the LC-MS data of that impurity it was concluded as Afatinib-N-oxide (3.17%) with m/z 524.2 (the actual molecular weight is 501.4), so it was confirmed as sodiated adduct of Afatinib-N-oxide. Thus, as per this analysis one of the impurities identified which need to be controlled in the process was Afatinib-N-Oxide. The HPLC chromatogram after before and after the oxidative degradation studies is shown in Figure 4:

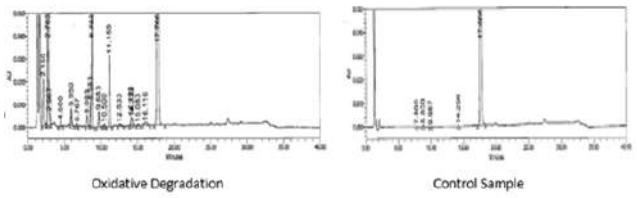

Figure 4. HPLC Chromatograms: Oxidative Degradation *Vs* Control Sample

2.6 Degradation under basic condition

The Afatinib Dimaleate was treated with 0.5N aqueous sodium hydroxide solution for 2 h at 70 °C. Different peaks were observed at about RRT 0.56 (11.03%), 0.74 (0.58%), 0.80 (1.51%) and 1.11 (0.20%). Among the list of impurities, two major impurities at about RRT 0.58 and 0.84 were in concordant with impurities observed regularly during laboratory development batches. Based on the LC-MS data of these RRT's, impurity at about RRT 0.56 was observed as hydroxy impurity with m/z 459.2 (the actual molecular weight is 458.1), so it was confirmed as protonated mass of hydroxy impurity and impurity at RRT 0.84 was observed as intermediate-1 with m/z of 375.1 (the actual molecular weight is 374.09), so it was confirmed as protonated mass of intermediate-1.Thus, as per this analysis two impurities identified which need to be controlled in the process was hydroxy impurity and intermediate-1. The HPLC chromatogram after before and after the basic degradation studies is shown in Figure 5:

2.7 Degradation under acidic condition

The Afatinib Dimaleate was treated with 1.0N aqueous Hydrochloric acid solution for 4 h at 70 °C. Only

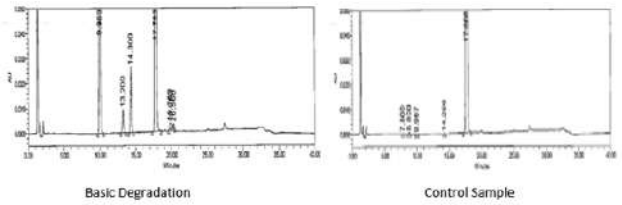

Figure 5. HPLC Chromatograms: Basic Degradation *Vs* Control Sample

one peak was observed as major degradant at about RRT 0.81 (9.20%). Since the impurity at RRT 0.81 was in concordant with the impurity observed constantly during laboratory development batches, so LC-MS was not performed. It is evident by the FD studies that intermediate-1 is the major degradant during both acidic and basic hydrolysis and is also the process impurity during the reaction. Thus, it needs to be controlled in such a way that the resulting sample should comply with ICH guidelines with actual limit not more than 0.10%. The HPLC chromatogram after before and after the acidic degradation studies is shown in Figure 6:

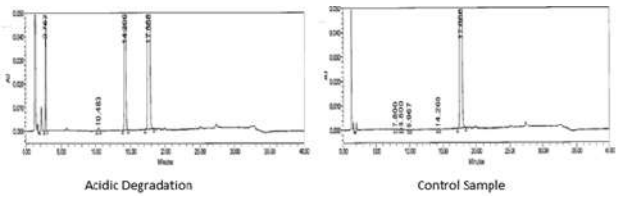

Figure 6. HPLC Chromatograms: Acidic Degradation *Vs* Control Sample

Based on forced degradation studies, three major impurities were identified in the process and control measure of those need to be established to comply the material as per ICH guidelines (all the probable impurities not more than 0.10%). The fourth impurity was new in the process and was identified based on the LC-MS data of developmental batches, which is explained later.

2.8 Synthesis of N-(3-chloro-4-fluorophenyl)-6-amino-7-[[(3S)-tetrahydro-3-furanyl] oxy]-4-quinazolinamine (Intermediate-1, 3)

In a clean and dry glass assembly, charged ethanol (4.5 L), (S)-N-(3-chloro-4-fluorophenyl)-6-nitro-7-((tetrahydrofuran-3-yl) oxy) quinazolin-4-amine, 4 (300.0 g, 0.7411 moles) and activated carbon (60 g), heated the suspension to 60-70 °C and added hydrazine hydrate (470 ml) and after addition raised the reaction temperature to 70-80 °C, monitored the reaction on HPLC (reaction time 1.0hr), added hyflo (5 g) in the reaction mass, stirred for 30-45 mins and then filtered the reaction mass through buchner funnel under hot conditions. Washed the entire bed with hot ethanol (300 ml). Concentrated the clear, pale green coloured mother liquor to 80-90% under vacuum not less than 640 mm Hg at 60-65 °C, added water (3000 ml) to the distilled residue, slurried the residue at ambient temperature for 30-45 minutes and filtered the solid. Washed the solid with water (100 ml.). Dried the solid under vacuum not less than 660 mm Hg at 60-65 °C for 4 hrs. Heated the dried solid with acetonitrile (2100 ml) at 55-65 °C and then gradually cooled to ambient temperature and then to 0-10 °C. Stirred the suspension for 45-60 mins at 0-10 °C. Filtered the solid, washed with chilled acetonitrile (300 ml.). Dried the wet solid under vacuum not less than 700 mm Hg at 60-65 °C for 10 h (moisture content 0.26% w/w) to afford 255.5g of title compound with HPLC Purity: 99.85%. ^{1}H-NMR (DMSO-d_6): δ 2.10 (m, 1H), 2.35 (m, 1H), 3.81 (dt, 1H), 4.00-3.94 (q, 3H), 5.20 (s, 1H), 5.77 (bs, 2H), 7.18 (s, 1H), 7.43-7.58 (m, 1H), 7.79-7.73 (m, 1H), 8.10 (dd, 1H), 8.57 (s, 1H), 10.33 (s, 1H), ^{13}C-NMR (DMSO-d_6): 32.32, 66.49, 71.91, 78.60, 101.23, 102.94, 109.42, 116.36, 116.65, 118.63, 118.87, 123.30, 123.40, 124.48, 135.82, 135.86, 137.47, 139.96, 147.60, 151.28, 152.14, 155.37, 156.08, Mass (M+H):375.0, IR (cm^{-1}): 1627, 1570, 1431, 1215, 1242, 1161, 3317, 856, 2862.

2.9 Synthesis of (E)-N-[4-(3-chloro-4-fluoroanilino)-7-[(3S)-oxolan-3-yl] oxyquinazolin-6-yl]-4-(dimethylamino)but-2-enamide (Afatinib free base, 2)

In a clean and dry glass assembly charged N, N-dimethylacetamide (2000ml), followed by N,N-dimethylcrotonic acid hydrochloride (154.6 g, 0.933 moles) to get suspension. Cooled the reaction mass to -12 to -6 °C and added thionyl chloride (155.3 g, 1.306 moles) dropwise in the reaction mass maintaining the reaction temperature. This part is labelled as solution-A. Dissolved intermediate-1 (250.0 g, 0.6670 moles) in N, N-dimethylacetamide (750 ml) and labelled as solution-B. Added solution-B in the solution-A at -12 to -6 °C within 20-25 minutes. After addition, immediately monitored the reaction on HPLC (intermediate-1, NMT: 0.15%). Quenched the reaction mass by adding aq. triethylamine (250 ml: TEA 100 ml and water 150 ml) dropwise in the reaction mass. Gradually, raised the reaction temperature to 20-25 °C. Diluted the reaction mass by adding water (250 ml.). Adjusted the pH of reaction mass using liquor ammonia (250 ml). Stirred the heterogenous reaction mass for 45-60 mins. Filtered

the precipitated solid and washed the solid with water (250 ml.). Suck dried the solid sufficiently under vacuum not less than 700 mm Hg and under nitrogen blanketing. Treated the sufficiently suck dried solid (moisture content NMT 5%) with mixed solvent system [dissolved the solid in tetrahydrofuran (1250 ml) at 25-30 °C and precipitated the solid by dropwise addition of water (3125ml) at 25-30 °C, gradually cooled the reaction mass to ambient temperature and further to 0-10 °C. Filtered the solid and washed the solid with tetrahydrofuran (50 ml.)]. Dried the solid under vacuum not less than 700 mm Hg without heating. Yield: 294.9 g (91% on theoretical basis), HPLC 99.87% with all impurities less than 0.10% by area percent. ^{1}H-NMR (DMSO-d_6): δ 2.15 (s, 1H), 2.35 (m, 1H), 3.10 (d, 2H), 3.79 (td, 1H), 3.94 (q, 1H), 4.01 (d, 2H), 5.29 (d, 1H), 6.60 (d, 1H), 6.80 (dt, 1H), 6.85 (t, 1H), 7.42 (t, 1H), 7.80 (m, 1H), 8.13 (dd, 1H), 8.52 (s, 1H), 8.96 (s, 1H), 9.44 (s, 1H), 9.81 (s, 1H); ^{13}C-NMR (DMSO-d_6): 32.32, 45.06, 59.69, 66.51, 71.92, 78.70, 107.92, 108.87, 116.18, 116.46, 122.34, 123.43, 125.72, 127.46, 136.80, 142.08, 148.59, 151.46, 153.10, 153.75, 154.68, 156.68; Mass (M+H): 486.0; IR (cm^{-1}): 1620, 1674, 1577, 1427, 1215, 1249, 1149, 1531, 3317, 817 and 2862. The developed process not only resulted in high quality Afatinib free base with all the impurities less than 0.10% but also resulted in novel polymorph[7,8] as designated by the following 2-theta values as tabulated in Table 1:

Table 1. 2-Theta values

2-theta values	d-spacing	Intensity
4.75	18.61	16.82
6.71	13.17	100.00
10.62	8.33	7.00
12.02	7.35	2.31
15.02	5.89	16.93
17.75	4.99	7.24
19.03	4.66	7.04
21.30	4.17	4.55
23.32	3.81	2.91
27.89	3.19	3.05

The XRD diffractogram is shown in the Figure 7.

2.10 Synthesis of (Z)-but-2-enedioic acid;(E)-N-[4-(3-chloro-4-fluoroanilino)-7-[(3S)-oxolan-3-yl]oxyquinazolin-6-yl]-4-(dimethylamino)but-2-enamide (Afatinib Dimaleate, 1)

In a clean and dry glass assembly charged tetrahydrofuran (2000 ml) and (E)-N-[4-(3-chloro-4-fluoroanilino)-7-[(3S)-oxolan-3-yl]oxyquinazolin-6-yl]-4-(dimethylamino)but-2-enamide, 2 (250.0 g, 0.5145 moles) to get suspension. Heated the reaction mass to 35-45 °C to get clear solution and added solution of maleic acid in tetrahydrofuran (122.45g, 1.054 moles in 750 ml tetrahydrofuran) maintaining the temperature. After precipitation of solid, gradually cooled the reaction mass to ambient temperature and further to 10-15 °C. Maintained the reaction mass at 10-15 °C for 60-90 mins, filtered the solid and washed with tetrahydrofuran (250ml). Dried the solid under vacuum not less than 700 mm Hg at 45-50 °C for 16 h. (m/c 0.45%). Yield: 328.8g (89% on theoretical basis), HPLC Purity: 99.90%. ^{1}H-NMR (DMSO-d_6): δ 2.36 and 2.14 (m, m, 2H), 2.83 (s, 6H), 3.78 (m, 1H), 4.01 and 3.92 (m, m, 5H), 5.32 (m, 1H), 6.14 (s, 4H), 6.80 (m, 2H), 7.28 (s, 1H), 7.44 (t, 1H), 7.78 (m, 1H), 8.09 (m, 1H), 8.59 (s, 1H), 8.96 (s, 1H), 9.76 (s, 1H), 10.03 (bs, 1H); ^{13}C-NMR (DMSO-d_6): 32.31, 42.11, 56.84, 66.51, 71.91, 78.93, 107.22, 108.57, 116.30, 116.59, 116.74, 118.58, 118.83, 122.71, 122.80, 123.93, 127.22, 131.59, 132.22, 133.35, 136.31, 136.35, 147.41, 151.80, 153.47, 153.60, 155.02, 156.99, 162.34, 166.92; Mass (M+H): 486.0; IR (cm^{-1}): 1616, 1681, 1573, 1427, 1492, 1192, 3344, 1249, 1149, 1527, 3317, 817, 1458, 2862 and 1350.

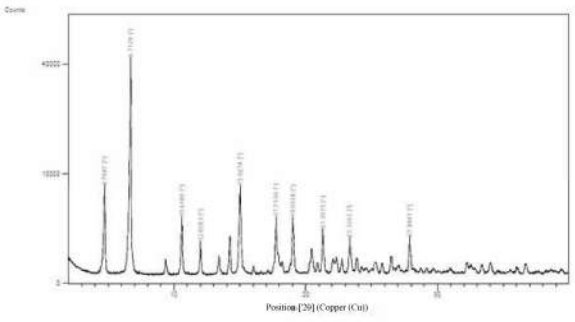

Figure 7. XRD Diffractogram of novel Afatinib free base

All the impurities discussed in the article is observed during the stage-02 (amidation step). Typical HPLC chromatogram of Afatinib dimaleate with all the process impurities formed in the process is shown in Figure 8. Detailed description of impurities observed during the process development studies of Afatinib dimaleate is discussed below:

2.11 Process impurities and their Structure elucidation

2.11.1 (S)-N-(4-((3-chloro-4-fluorophenyl) amino)-7-((tetrahydrofuran-3-yl) oxy) quinazolin-6-yl) acetamide (acetamide impurity)

During initial developmental batches a particular impurity at RRT 0.93 were observed constantly. The

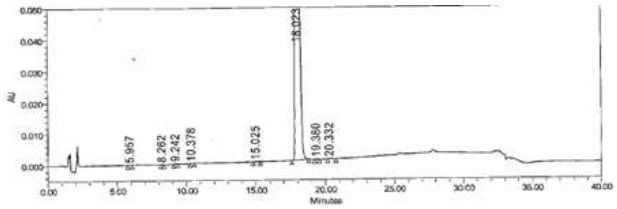

Figure 8. HPLC chromatogram of Afatinib Dimaleate

knowledge about the fragmentation pattern of impurities could acquire structural information and therefore taken further studies using MS/MS. Based on the initial characterization by LC-MS, the impurity manifested protonated molecular mass of m/z 417.11 (M+H) and two daughter ions as m/z 346.06 and m/z 304.05. The entire fragment pattern is shown below with chemical structures in Figure 9:

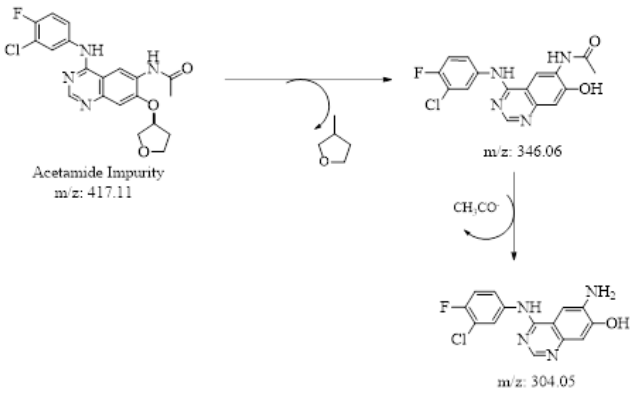

Figure 9. MS/MS of acetamide Impurity

The acetamide impurity was formed by reaction between acetic acid and intermediate-1. The speculation of impurity formation with acetic acid was confirmed by adding catalytic amount of acetic acid in amidation reaction which led to same impurity at about RRT 0.93. The source of acetic acid was identified as solvent N, N-dimethylacetamide which was the reaction media for amidation step. By titrimetric analysis and gas chromatography it was confirmed that catalytic amount of acetic acid was present in the solvent N, N-dimethylacetamide. Thus, the content of acetic acid was controlled in N, N-dimethylacetamide up to a level of 0.002%. However, that catalytical amount was not reflecting the actual percentage of impurity forming in the reaction mass. Even by controlling the amount of acetic acid in N, N-dimethylacetamide acetamide impurity was still observed. Later it was postulated that the N, N-dimethylacetamide is degrading into acetic acid in the reaction mass under acidic pH (source of acidity was excess of thionyl chloride) and presence of moisture (either from raw material or intermediate-1). To prove this postulation, a reaction was performed with excess quantity of thionyl chloride and elevated content of acetamide impurity was observed in the isolated solid. Thus, by controlling the acidity of reaction mass (by using the optimal quantity of thionyl chloride) and moisture in raw material and intermediate-1, this acetamide impurity was controlled up to a level of less than 0.04%.

2.12 Synthesis of Acetamide Impurity

In a clean and dry glass assembly added, dichloromethane (50 ml) followed by intermediate-1 (5.0 g) and acetic anhydride (1.49g, 0.0145 moles). Heated the reaction mass to 35-40 °C for 45-60 mins and monitored the reaction mass on HPLC. Distilled the reaction mass to dryness on rotavapor and slurried the distilled residue with n-heptane (50 ml). Filtered the solid, washed with n-heptane (25 ml). Dried the material in oven at vacuum not less than 660 mm Hg till constant weight. Yield: 3.0 g (60% on w/w basis). HPLC : 98.74%. The HPLC chromatogram of the prepared acetamide impurity is shown in Figure 10 and was characterized by NMR (^{1}H and ^{13}C), (Figure 11, Figure 12), Mass (Figure 13) and IR (Figure 14) as per the structure given below:

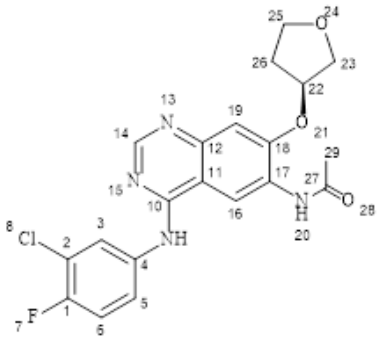

^{1}H-NMR (DMSO-d$_6$): NH (20) δ 9.77 (s, 1H), C14-H 9.33 (s, 1H), C16-H 8.81 (s, 1H), C19-H 8.52 (s, 1H), C3-H 8.13 (dd, 1H), C5-H 7.80 (m, 1H), C6-H 7.41 (t, 1H), NH (9) 7.16 (s, 1H), C22-H 5.27 (d, 1H), C23 and C25-Hb (3.94 (q, 1H), C31-H 3.10 (d, 1H), C26-Ha 2.33 (m, 1H), C29-H and C26-Hb 2.15 (s, 3H and 1H);

^{13}C-NMR (DMSO-d$_6$): C10 (168.68), C27 (156.67), C18 (153.73), C14 (153.1), C1 (151.46), C12 (148.61), C4 (136.74), C17 (127.62), C28 (123.44), C2 (122.34), C5 (118.71), C3 (118.46), C6 (116.46), C11 (116.18), C19 (108.8), C16 (107.92), C22 (78.61), C23 (71.93), C25 (66.5), C29 (32.34); **Mass (M+H)**: 417.11; **IR (cm^{-1})**: 1624, 1681, 1531, 1577, 1431, 1207, 1027, 1141, 3529, 3298, 817, 2881.

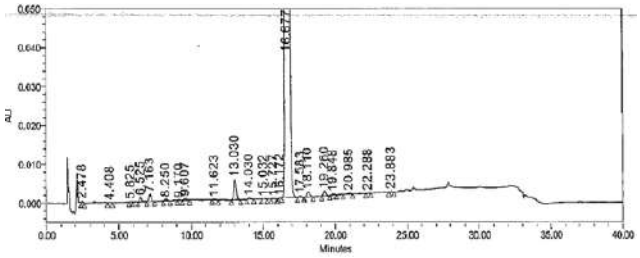

Figure 10. HPLC Chromatogram of acetamide impurity

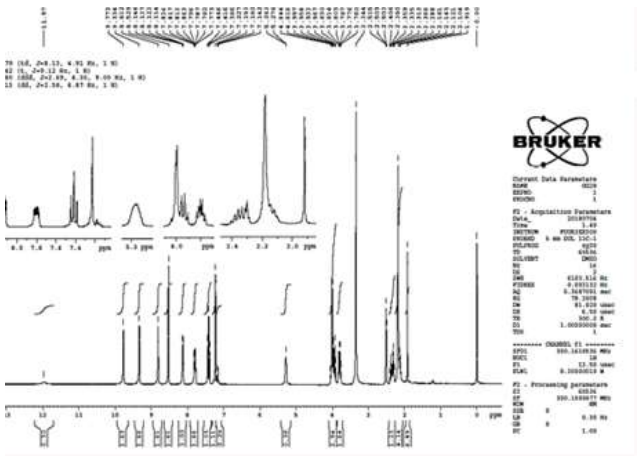

Figure 11. ^{1}H-NMR of acetamide impurity

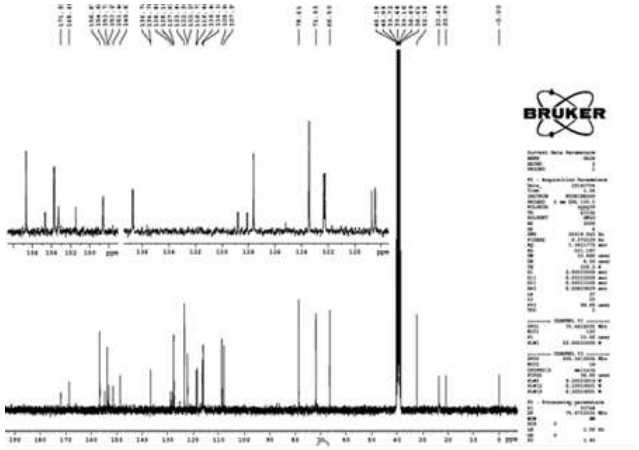

Figure 12. ^{13}C-NMR of acetamide impurity

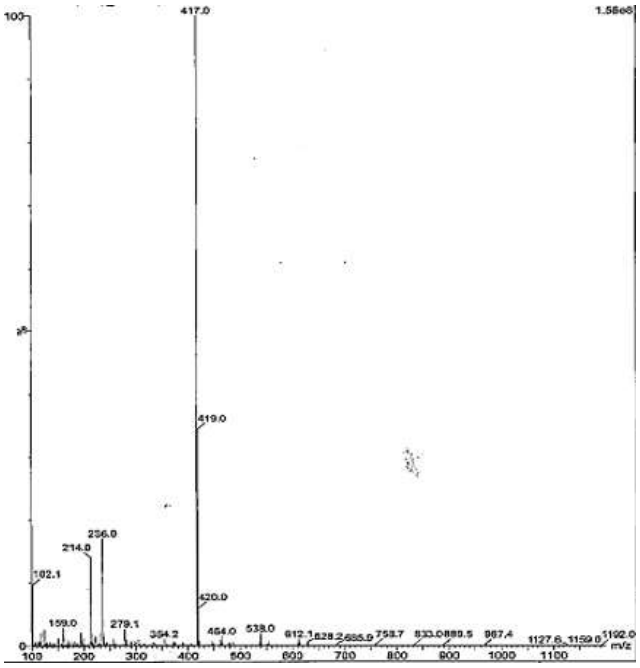

Figure 13. Mass chromatogram of acetamide

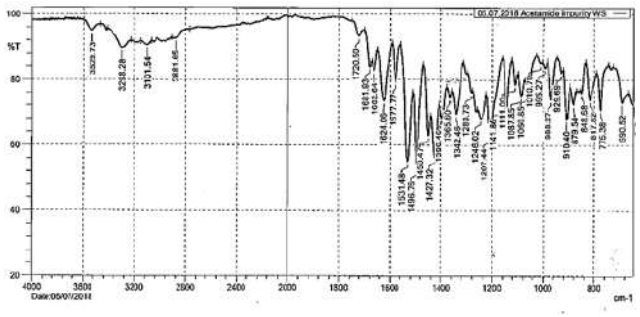

Figure 14. IR spectrum of acetamide impurity

2.12.1 1-(4-((3-chloro-4-fluorophenyl) amino)-7-((S)-tetrahydrofuran-3-yl) oxy) quinazoline-6-yl)-5-Hydroxypyrrolidin-2-one (hydroxy impurity)

As per the developed analytical method hydroxy impurity elutes at about RRT 0.58. The initial characterization was based on the LC-MS data. The mass spectrophotometer manifested protonated molecular mass of hydroxy impurity at m/z 459.2 (M+H). The typical mass chromatogram is shown below in Figure 15:

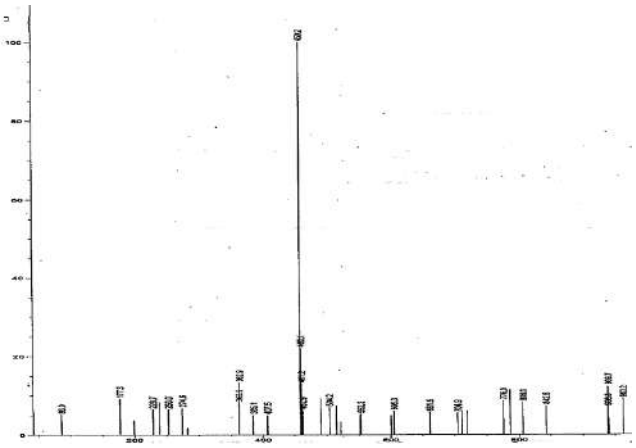

Figure 15. Mass chromatogram of Hydroxy impurity

2.12.2 Afatinib N-oxide

As per the developed analytical method Afatinib-N-oxide elutes at RRT 0.50. The initial characterization was based on the LC-MS data. The knowledge about the fragmentation pattern of impurities could acquire structural information and therefore taken further studies using MS/MS. The mass spectrophotometer manifested molecular mass of Afatinib-N-oxide at m/z 524.2 (M+Na) The mass chromatogram is represented in the Figure 16 as below:

2.13 High Performance Liquid Chromatography (analytical)

A waters HPLC system equipped with alliances 2695 series low pressure quaternary gradient pump along with photo diode array detector and auto sampler has been used for the analysis of samples. The data was collected and processed using waters "Empower 2" software. An Inertsil C18 (150* 4.6 mm, 5-Micron, GL Sciences, Japan) column was employed for the separation of impurities from Afatinib Dimaleate. The column eluent was monitored at 254 nm. A simple gradient reverse-phase HPLC method was optimized for the separation of impurities from Afatinib Dimaleate active pharmaceutical ingredient where the mobile phase was a mixture of 2

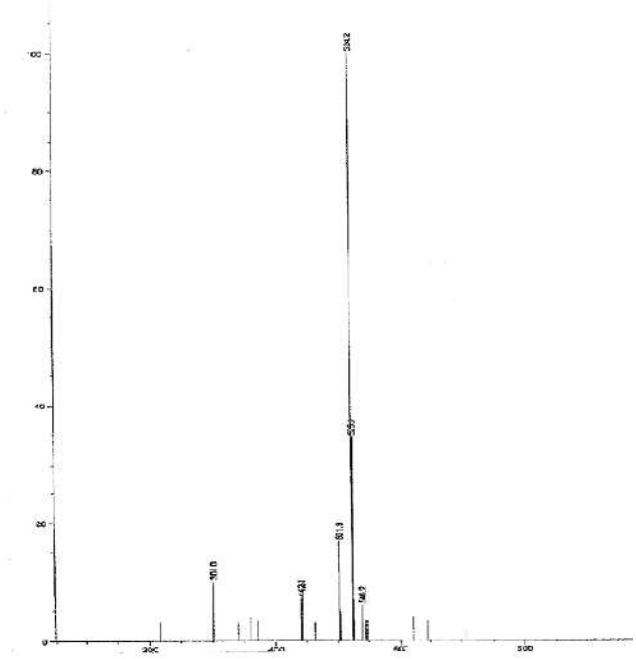

Figure 16. Mass chromatogram of Afatinib-N-oxide

mmol L^{-1} ammonium acetate and acetonitrile (composition of mobile phase 0.02M potassium dihydrogen phosphate and 1.0 g/L 1-octanesulphonicacid sodium salt and acetonitrile). Chromatography was performed at room temperature using at a flow rate of 1.0 mL min^{-1}. The chromatographic run time was 40 min. The result was analysed weight/weight (w/w) with respect to reference standard and all the total impurities were complying the ICH guidelines. The developed method was validated as per ICH guidelines with respect to precision, accuracy, linearity, robustness, specificity and system suitability.

2.14 Mass Spectrometry (LC-MS/MS)

LC-MS/MS analysis has been performed on API 2000, Mass Spectrometer. The analysis was performed in positive ionization mode with turbo ion spray interface. The parameters for ion source voltage IS = 5500 V, declustering potential, DP = 70 V, focusing potential, FP = 400 V, entrance potential, EP = 10 V were set with nebulizer gas as air at a pressure of 40 psi and curtain gas as nitrogen at a pressure of 25 psi. An Inertsil C18 (150 * 4.6 mm, 5-Micron, GL Sciences, Japan) column was used for the separation. The mobile phase is a mixture of 2 mmol L^{-1} ammonium acetate and acetonitrile with a flow rate of 1.0 mL min^{-1}.

2.15 NMR spectroscopy

The ^{1}H and ^{13}C NMR experiments were carried out at frequencies of 300 MHz and 75 MHz respectively,

in DMSO-d_6 at 25 °C temperature on a Varian-400 FT NMR spectrometer. ^{1}H and ^{13}C chemical shifts are reported on the d scale in ppm, relative to tetra methyl silane (TMS) δ 0.00 and $CDCl_3$ at 77.0 ppm in ^{13}C NMR respectively.

3 Results and discussion

Initial studies for the synthesis of Afatinib involves lot of efforts starting from selection of reducing agents to selection of solvent for amidation, selection of chlorinating agent for N, N-dimethylcrotonic acid hydrochloride, appropriate reaction temperature for chlorination and amidation, isolation procedure for Afatinib free base as it is highly unstable and degrades easily in the presence of moisture and oxygen. The main challenge was to isolate the Afatinib free base in highly pure and stable form, its purification (if required) and stability over the period. For the synthesis of Afatinib free base **2**, the entire study was divided in three parts, part-1 was the selection of solvent and chlorinating agent for the conversion of N, N-dimethylcrotonic acid hydrochloride to acid chloride, part-2 was the selection of solvent for amidation and addition mode and part-3 was the isolation of Afatinib free base. For part-1, based on the nature of reaction, all protic solvents were ruled out, during exploratory studies solvents such as toluene, ethyl acetate, acetonitrile and thereof were ruled out, the options left were polar aprotic solvents such as N, N-dimethylformamide, N-methylpyrrolidone (NMP) and N, N-dimethylacetamide. Out of these solvents only N, N-dimethylacetamide was feasible and effective, rest solvents were either charring the reaction or resulting in incomplete conversion. To select chlorinating agents, wide variety of reagents were available such as thionyl chloride, oxalyl chloride and thereof but with oxalyl chloride complete conversion of reaction was never achieved. Thus, based on effectiveness and cost thionyl chloride was opted as chlorinating reagent. By optimal quantification all other parameters such as reaction temperature, mode and rate of addition of chlorinating agent, the complete conversion of N, N-dimethylcrotonic acid hydrochloride to acid chloride was achieved in 1.0-1.5 h. For part-2, during exploratory studies it was observed that mixture of solvent is not capable for complete conversion (from **3** to **2**) so single solvent reaction was finalized and only N, N-dimethylacetamide was used throughout the reaction. Later the addition pattern was studied whether solution of **3** in acid chloride reaction mass or vice-versa. Based on exploratory studies, addition of acid chloride solution to **3** was generating lot of impurities (since acid chloride is highly unstable) and reaction time was longer (more than 3 h), so the idea was dropped, and the only feasible option was to add solution of **3** in acid chloride solution. By doing this, as soon as the addition of **3** was completed reaction complies with conversion rate of more than 99.5% and all the process as well degradation impurities were well within the controllable limit. For part-3, during the exploratory studies it was observed that quenching of thionyl chloride with water would be tedious during the scale up, thus it was suggested to reduce the pH of reaction mass followed by quenching with water. To follow this, aqueous triethylamine was used instead of water which would not only reduce the pH but would also quench the reaction mass. Since, **2** is in its hydrochloride form and to isolate it in pure form as base further pH adjustment is required. Lot of organic and inorganic bases were explored but based on the degradation data under basic condition, it was suggested to have that base which should not facilitate the degradation of **2.** Thus, based on the scientific logic and available data, 10-15% liquor ammonia was used and after pH adjustment, nitrogen was purged to remove the excess ammonia. This approach not only avoided the degradation of compound but also made the isolation of product in pure form with HPLC purity around 99.59% by area percent. Later, the **2** was treated with tetrahydrofuran and water to get compound with HPLC purity more than 99.80% and all listed process impurities less than 0.10%.

As per above establishment, synthesis of Afatinib dimaleate was completed in three steps starting from (S)-N-(3-Chloro-4-fluorophenyl)-6-nitro-7-((tetrahydrofuran-3-yl) oxy) quinazolin-4-amine **4**. The yield in every step is quantitative. The entire protocol is depicted in figure-1

3.1 Conclusion

Afatinib Dimaleate is a potent aromatase inhibitor drug used in the treatment of cancer diseases. The present research work describes an improved process wherein all impurities (known and unknown) are controlled to a level of 0.10%. New HPLC method was developed for the detection and separation of four process related impurities from Afatinib Dimaleate. The reported process explains the formation of new process impurity which needs to be controlled to achieve the material as per regulatory guidelines. All the four impurities detected using the new HPLC method and were characterized using LC-MS and NMR data.

References

[1] Walter C, Lahiri S, Bhaskar B M, *et al*. Polymorphic forms of Afatinib free base and Afatinib Dimaleate. 2015, WO2016/199076 A3.

[2] Solca F, Dahl G, Zoephel A, *et al*.Target binding properties and cellular activity of Afatinib (BIBW 2992), an irreversible ErbB family blocker, The Journal of Pharmacology and Experimental Therapeutics, 2012, **343**(2): 342-350. https://doi.org/10.1124/jpet.112.197756.

[3] Matioram RG, Channaveerayya H, Yadav M D, *et al*. Novel salts and polymorphic forms of Afatinib. 2011, WO 2012/121764 A1.

[4] Wang X, Goldstein D, Crowe PJ, *et al*. Next-generation EGFR/HER tyrosine kinase inhibitors for the treatment of patients with nonsmall-cell lung cancer harboring EGFR mutations: a review of the evidence. OncoTargets and Therapy, 2016, **9**:5461-5473.

[5] Himmelsbach F. Quinazoline derivatives and pharmaceutical compositions containing them. US Patent RE43431 E, 2012.

[6] Gilotrif (Afatinib)-FDA label (2003) https://www.accessdata.fda.gov/drugsatfda_docs/label/2018/201292s014lbl.pdf

[7] ICH Q7 Good Manufacturing Guidelines for API Manufacturing https://www.fda.gov/downloads/Drugs/%E2%80%A6/Guidances/ucm073497.pdf

[8] Handoo S, Arora V, Khera D, *et al*. A comprehensive study on regulatory requirements for development and filling of generic drugs globally. International Journal of Pharmaceutical Investigation, 2012, **2**(3): 99-105. https://dx.doi.org/10.4103/2230-973X.104392

[9] Soyka R, Rall W, Schnaubelt J, *et al*. Process for Preparing amino crotonyl compounds. US8426586 B2, 2006.

[10] Wissner A, Tsou R H, Johnson D B, *et al*. Substituted quinazoline derivative. US Patent 6251912, 1998.

Chem Rep, 2019, 1(1): 13-21
DOI: 10.25082/CR.2019.01.002

RESEARCH ARTICLE

Kinetics of the thermal disappearance of radicals formed during the radiolysis of L-α-anhydrous asparagine

Ana Neacsu[1*] Daniela Gheorghe[1]

Abstract: An EPR study of paramagnetic centers formed by irradiation of polycrystalline L-α-anhydrous asparagine (L-Asn) was performed. The EPR spectra of gamma irradiated samples at room temperature, shown the presence of three types of paramagnetic centers. A possible mechanisms of formation for the three radical species is suggested, based also on literature data. The kinetics of the disappearance of radicals during thermal annealing indicated a complex mechanism.

Keywords: L-α-anhydrous asparagine, ionizing radiation, paramagnetic centers, thermal disappearance, unpaired electron

1 Introduction

Amino acids which are the building blocks of proteins are among the simplest organic molecules of biological relevance and thus serve as convenient model systems in studies of radiation damage. Asparagine is an aminoacid that plays an imperative role in the metabolic control of some cell functions in nerve and in brain tissue and is used by many plants as a nitrogen reserve substance.[1] Asparagine is one of the 20 most common natural amino acids in living organisms. It has carboxamide as the side chain's functional group.

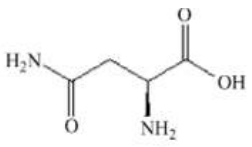

asparagine

Asparagine has a high propensity to hydrogen bond, since the amide group can accept two and donate two hydrogen bonds. The well-known deamidation of L-Asn was documented because of its occurrence in all tissues.[2]

Oxidative damage enhances L-Asn instability[3] which indicates a free radical route in asparagine degradation. L-Asn is a highly conserved amino acid in the family of cyclooxygenases, key enzymes in inflammation processes.[4] Since these enzymes function in conditions of oxidative stress, the behavior of L-Asn residue toward free radical is important. Even if they do not belong to the active site, these residues are important in maintaining the three dimensional structure of proteins by their participation in hydrogen bond network.[5]

Peptides containing asparagine residues undergo side chain cleavage during dissociative electron attachement and it was proposed that such losses could be used to ascertain the presence of this residue in unknown peptides.[6] It was shown that sequences containing asparagine residues are prone understood despite their importance in many biological (radioprotection, radiotherapy) and industrial processes (radiosterilization of food and drugs).

The analysis of EPR spectra of L-α- anhydrous asparagine irradiated in solid state indicated the certain existence of three radicals, stable at room temperature, two radicals resulted from decarboxylation and deamination processes and the third radical from expulsion of a hydrogen atom from the amidic group.

2 Experimental

Polycrystalline samples of L-α- anhydrous asparagine have been irradiated with gamma rays at the room temperature by using a ^{137}Cs source (Gammator type). The irradiation dose was 1.05×10^2 Gy/h. The EPR spectra

Received: January 29, 2019 **Accepted:** February 26, 2019 **Published:** March 1, 2019

*Correspondence to: Ana Neacsu, "Ilie Murgulescu" Institute of Physical Chemistry, 202 Spl. Independentei, Bucharest 060021, Romania; Email: anna_matache@yahoo.com
[1] "Ilie Murgulescu" Institute of Physical Chemistry, 202 Spl. Independentei, Bucharest 060021, Romania.

Citation: Neacsu A and Gheorghe D. Kinetics of the thermal disappearance of radicals formed during the radiolysis of L-α-anhydrous asparagine. *Chem Rep*, 2019, **1**(1):13-21

were recorded at room temperature with an EPR ART 6 instrument (IFIN Magurele) which operates in the X band with high frequency modulation of 100 kHz. The g factors were determined using the Mn^{2+} ion in CaO matrix as a standard.

3 Results and discussions

Asparagine similarly to all amino acids, having an acidic and a basic group, neutralize intramolecularly resulting a zwitterion structure.[7] Direct ionization of L-α- anhydrous asparagine molecules by gamma radiations it can be detected experimentally only at low temperatures (77 K) and should lead to the formation of a radical cation resulted from the expulsion of an electron followed by the formation of radical anion by the addition of the expelled electron. Regarding L-α- anhydrous asparagine, the location of the electron excess is considered to be on the carboxyl group.[8] The theoretical and EPR study conducted by Strzelczak et al.[9] upon irradiated anhydrous asparagines in polycristalline solid state revealed the existence of three radicals species stable at room temperature. The nature of the radicals was established based on the simulated structures of the three entities, and the theoretical spectrum obtained from the overlapping of the simulated spectra was identical to the experimental one. The structures of the three radicals resulting from the decarboxylation, deamidation and dehydrogenation processes during L-α- anhydrous asparagine irradiation will be presented in the radiolysis mechanism.

In Figure 1 is shown the EPR spectrum of L-α- anhydrous asparagine sample irradiated with a 4.7×10^4 Gy dose.

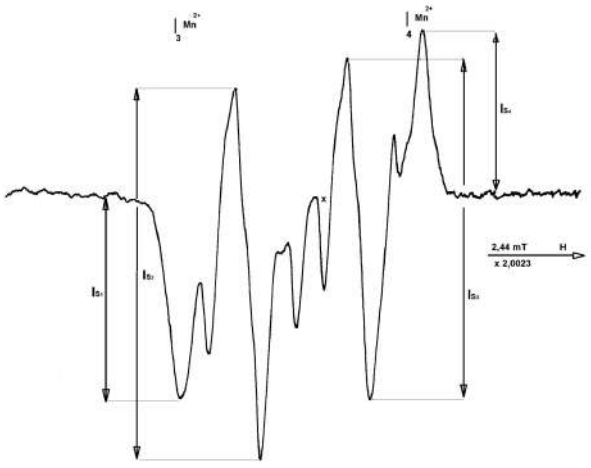

Figure 1. EPR spectrum of polycrystalline L-α- anhydrous asparagine sample irradiated with a 4.7×10^4 Gy dose

From Figure 1 it is found that the spectrum is complex consisting of 7 well solved components, two of the four central lines presenting high intensity. The chemical structure of the three radical entities can not be determined from the EPR spectra. There are two factors that make difficult the establishment of the chemical structure of the three radical species: first, the overlapping of the lines that form the spectrum of each radical and the second essential factor is the appropriate thermal resistance of the radicals. If the three paramagnetic centers had different thermal stabilities then, after heating the irradiated sample to a certain temperature, it would have to be noted the disappearance of some components accompanied by the significant modification of the spectrum structure. As will be seen in this study, this behavior is not found.

In Figure 2 is shown the spectrum of 4×10^4 Gy irradiated sample recorded before and after heating 140 minutes at 180°C.

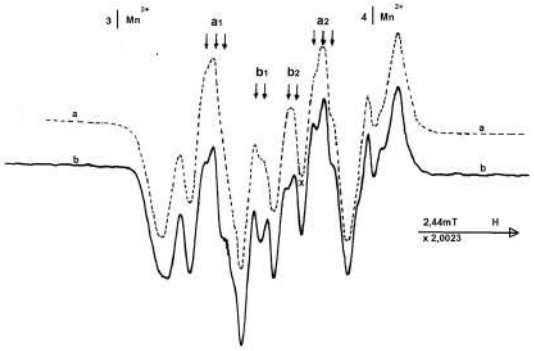

Figure 2. EPR spectrum of irradiated L-α-anhydrous asparagine sample; a) before heating b) after heating 140 minutes at 180°C

The results from Figure 2 is as the following:

(1) Both the shape of the spectrum and the number of spectral components of the irradiated sample after heating are identical to the unheated sample.

(2) It is noted that the four central components of the irradiated and heated sample have additional hyperfine splittings, marked with arrows.

(3) After heating the irradiated sample there is an accentuation of both the hyperfine splittings in three intensive components marked with a_1 and a_2 as well as the two splitting of the central lines marked with b_1 and b_2.

This behavior, correlated with the kinetic study to be presented, provides arguments for considering that three radical species whose spectra overlap are formed on L-α- anhydrous asparagine irradiation. Since each spectral line could belong to two radicals, in order to perform the kinetic study, the intensity decrease of the four main

components of the spectrum, noted Is_1, Is_2, Is_3, Is_4 (Figure 1) was noted, study conducted with both irradiation dose and heating temperature.

In order to obtain information on the increase of the radicals concentration versus the absorbed dose, it is shown in Figure 3, for example, the intensity variation of the two components Is_1 and Is_2 versus irradiation dose.

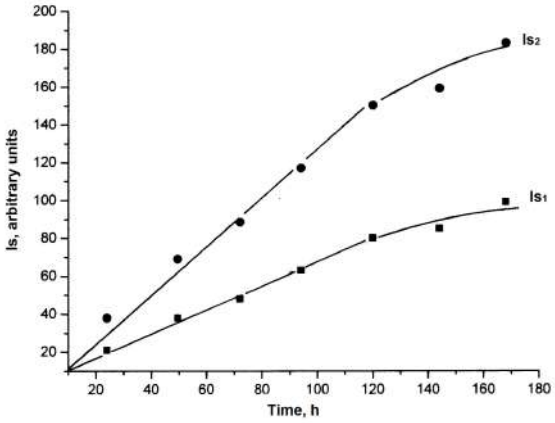

Figure 3. Variation of irradiation times (4.2×10^2 Gy/h dose rate) of Is_1 and Is_2 signals intensities of the EPR spectrum of irradiated L-α-anhydrous asparagine samples

From Figure 3 is is noted a linear increase of the two signals intensities versus irradiation dose, up to 5×10^4 Gy, followed by a tendency to a constant value, for high doses. The signals are proportional to the amount of radicals in the irradiated samples. Since the radical concentration is a function of the absorbed dose, the substance may serve as a dosimeter material. The L-α-anhydrous asparagines radicals are unusually stable because of the crystalline forme and the pure dry crystals, the signal loss is only about 3% during an year after irradiation. The substance has a linear dose response from 1 Gy up to 5×10^4 Gy. Using EPR spectroscopy as a detection method, the peak to peak amplitude Is_2 and Is_3 of the central spectral lines is proportional to the radical concentration which is proportional to the absorbed dose. The tendency to a constant value after a certain absorbed dose proves that as the concentration of radicals increases, the number of those that disappear under the action of the radiation increases too. When a constant concentration of radicals is reached, this means that the rates of the two processes become equal.

The study of the thermal behavior of the radicals formed during the radiolysis of the L-α- anhydrous asparagine, required firstly, plotting of the reaction isochronous. For this purpose, an irradiated sample with a dose of 4×10^4 Gy of L-α- anhydrous asparagine was gradually heated 5 minutes in stepwise (each step= 10°C), from room temperature up to the temperature of the complete disappearance of radicals.

After each isothermal heating temperature, the EPR spectrum of the sample was recorded under the same conditions at all temperatures. The results are shown in Figure 4.

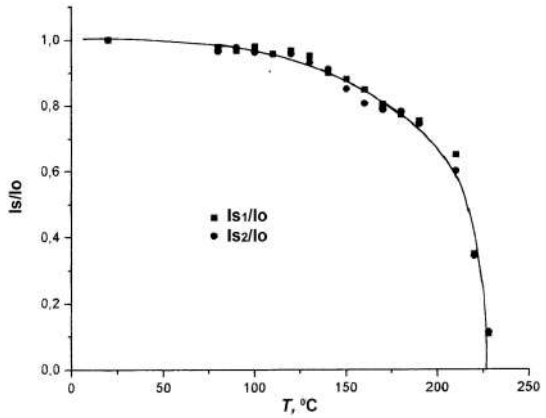

Figure 4. Isochronous variation of the EPR spectrum Is_1 and Is_2 signal intensities (arbitrary units) versus heating temperature of a 4×10^4 Gy irradiated L-αanhydrous asparagine

Figure 4 shows that although the isochronous heating was performed on a wide temperature range, the radicals dissapearance until 150°C does not occur. From this temperature it can be seen a slow decrease of the signals intensities Is_1 and Is_2 and then at 200°C the decrease occurs suddenly, the complete disappearance of the radicals under the mentioned work conditions taking place around 220°C, very close to the melting temperature of the sample.

The kinetic study of the paramagnetic centers thermal annealing required the plotting in isothermal conditions of the radicals concentrations variation, respectively the peak to peak signal intensity of the four components of the spectrum, Is_1, Is_2, Is_3, Is_4, versus isothermal heating time.

The temperatures for performing the thermal dissapearance study of radicals complied with the conditions imposed by the chemical kinetics: for the low temperature the process of disappearance should be at least 50% and for the upper maximum temperature, the rate of radicals dissapearance should not be too high in order to carry out a sufficient number of determinations required to establish the reaction order.

In these conditions the intensity of the Is_1, Is_2, Is_3, Is_4 components of the EPR spectra was measured versus the isothermal heating time at 180°C, 190°C, 200°C and 207°C. To highlight the influence of the temperature increase on the thermal annealing rate of the radicals formed in the irradiated samples, it is shown in Figure 5

the decrease of the Is_2 EPR signal versus time, at the four temperatures 180°C, 190°C, 200°C and 207°C.

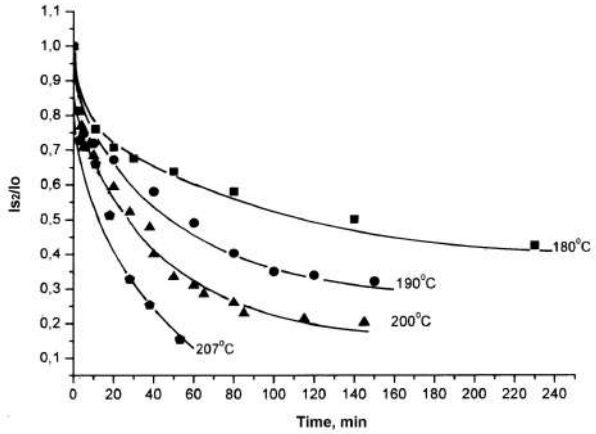

Figure 5. Isothermal variation of the intensity of the EPR signal Is_2 at the temperatures: 180°C, 190°C, 200°C, 207°C

The shape of the curves from Figure 5 shows that the higher the heating temperature of the irradiated samples of L–α-anhydrous asparagines was, the faster was the decrease of the radicals concentration. The four isotherms from Figure 5 present the same shape, firstly showing a high radicals concentration decrease then the tendency to a constant value and finally a decrease as the heating temperature increases. For long times of heating, the radical concentration tends to a constant value, which decreases as the heating temperature increases.

The explanation of the above-mentioned phenomenon is due to the increase of the mobility of the radical species with the temperature rise: when the thermal energy received from the outside exceeds that of the radicals with the surrounding molecules, they detach from the occupied position in the network and enter the reaction through different mechanisms depending on the temperature as will be shown from the kinetic study. The tendency to a constant value shows that at each temperature there are still radicals that do not disappear because they have higher thermal resistance being more strongly trapped in the crystalline network. Similar results were found by performing the same experiment on other irradiated organic substances[10] and inorganic ones.[11,12]

In order to study the kinetics of the thermal disappearance of radicals, we tried to fit our data in integral equations, used in chemical kinetics. For determining the reaction order and calculate the rate constants, the integral kinetic equations for all fractional and integers orders were plotted using the graphic method. The reaction order was established from the graphical representation which gave a straight line, the other representations were curves. For calculating the rate constants it was used the dimensionless parameter ($R=Is/I_0$) relative intensity instead concentration, I_0 representing the initial intensity of the signal recorded at room temperature and Is the intensity of the same signal recorded after each isothermal heating time.

Regarding the kinetic study, it should be noted that the establishment of the global reaction order was made from the graphical representation of the kinetic equation which gave a straight line having the highest correlation coefficient. The same order was found at the same temperature for all four components. At 180 °C the highest correlation coefficient was obtained from the R^{-2} graphic representation versus the isothermal heating time. This behavior was found for all four Is_1, Is_2, Is_3, Is_4 spectral components. For example, Figure 6 shows R^{-2} versus to isothermal heating time at 180°C for Is, proving that a third order kinetic was checked.

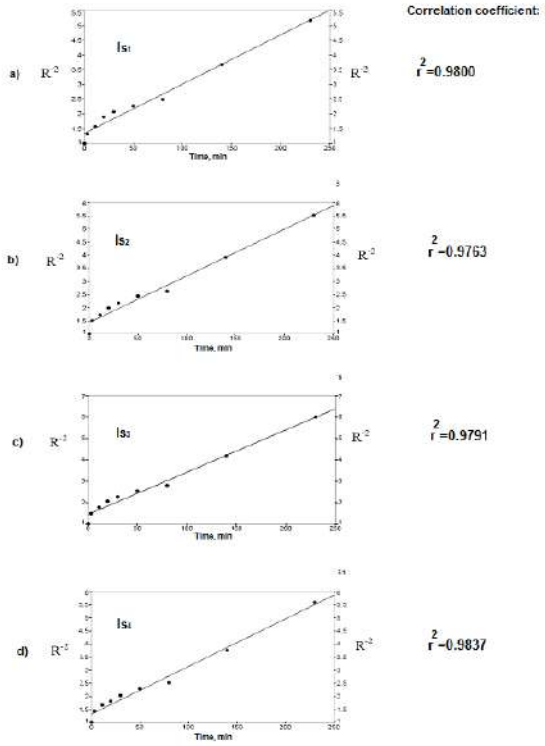

Figure 6. Variation of R^{-2} versus isothermal heating time at 180°C for all four components of the L-α-anhydrous asparagines spectrum

At 190°C, a high correlation coefficient was obtained from the $R^{-3/2}$ representation versus time, proving that the thermal annealing process of the radicals at this temperature verifies a fractional kinetic of 2.5 order (Figure 7).

At 200°C, the R^{-1} representation versus the heating time for all four components straight lines were obtained, proving that the thermal disappearance of the radicals follows a second order kinetics. Figure 8 exemplifies this

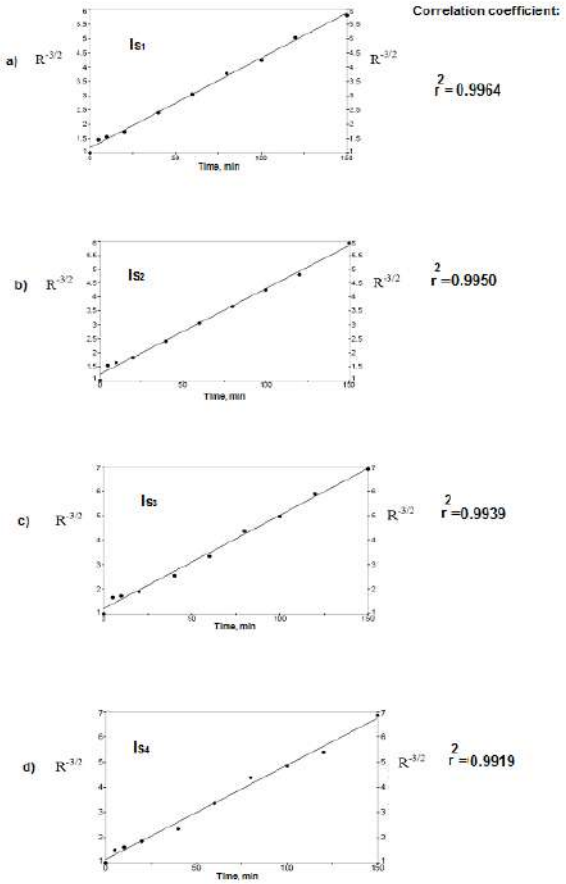

Figure 7. Variation of $R^{-3/2}$ versus isothermal heating at 190°C, for L-α-anhydrous asparagine sample, irradiated with a 7×10^3 Gy dose

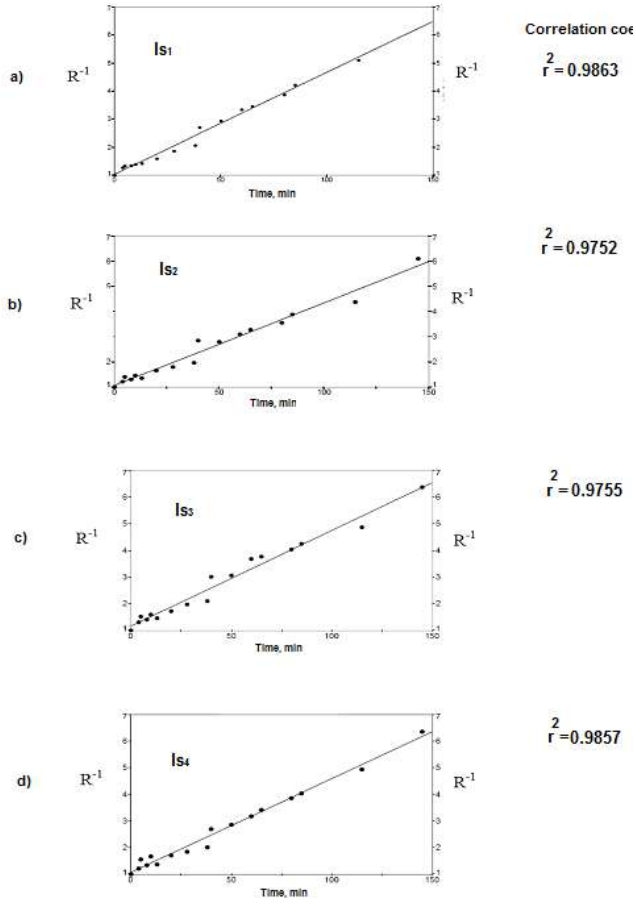

Figure 8. Variation of R^{-1} versus isothermal heating time at 200°C for L-α-anhydrous asparagine sample, irradiated with a 7×10^3 Gy dose

representation.

At 207°C, the logarithm of the relative intensity (lnR) plot versus time for the four components shown in a straight lines, confirming that the disappearance of the radical entities present a kinetic of the first order (Figure 9).

The values of the rate constants calculated from the slopes of the graphical representations corresponding to the global reaction orders: 3, 2.5, 2, 1 for all four spectral components are listed in Table 1.

The results of the kinetic study lead to the following conclusions:

(1) The most important finding is the variation of the reaction order. As the temperature rise from 180°C to 207°C, over a temperature range of about 30°C, the reaction order gradually decreased from 3 to 1.

(2) The high reaction orders of 3, 2.5, 2 from 180°C, 190°C, 200°C prove that the process of the radicals thermal dissapearance is complex, this means that the three radicals disappear through several reactions involving different mechanisms.

(3) The high values of the reaction orders (3, 2.5, 2) found, evidenced that three radical entities are formed on L-α-anhydrous asparagine irradiation.

The results of the thermal disappearance study of the trapped radicals in the crystalline lattice that occurs when heating the irradiated samples proves that the rate of this process, namely the reaction order, is influenced by the nature of the radicals having different thermal resistance. Indeed, increasing the temperature, the vibration of the crystalline network constituents increases and produces the weakening of the bonds that keep the radicals trapped.

Due to the large variation of the reaction order, the activation energy corresponding to a particular order could not be determined over a narrow temperature range.

At 170°C, none of the known kinetics equations were verified. This behavior is a particular case, proving that the thermal annealing process is strongly influenced by a physical one, which best respects the so-called "step-disappearance".[13]

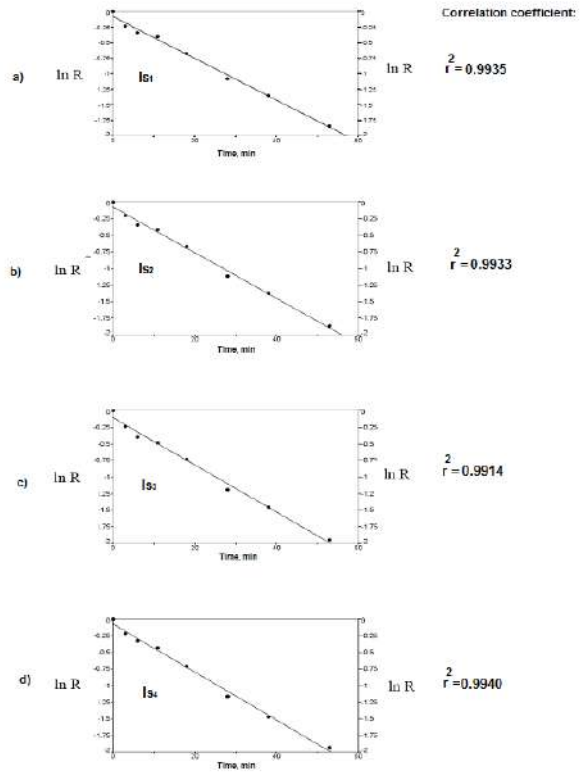

Figure 9. Variation of lnR versus isothermal heating time at 200°C for L-α-anhydrous asparagine sample, irradiated with a 7×10^3 Gy dose

The kinetic of the disappearance of the radicals formed in the irradiated samples of L-α-anhydrous asparagine and heated to 170°C could be explained using "the steps" model developed by Waite.[14,15] According to this model, the disappearance of radicals with a random space distribution involves two processes: a rapid process of recombination of nearby entities and a slow recombination process that occur due to vacancies formed after the diffusion of radicals within the network. Both processes lead to two approximations that are in the form of the second order kinetic equations. For example, the variation of the R^{-1} ratio versus the isothermal heating time at 170°C for the four main components of the EPR spectrum is shown in Figure 10.

From the slopes of the straights lines plotted, the rate constants k_{A1}, k_{A2}, k_{A3}, k_{A4} for the rapid process and k_{B1}, k_{B2}, k_{B3}, k_{B4} for the slow process were calculated, the values are listed in Table 2.

Comparing the values of the rate constants determined according to the Waite model[14] for the four intense components of the EPR spectrum, the following observations are noted:

(1) The initial recombination process of the radicals is about 10 times faster than that of diffusion (kA - 10 kB)

(2) The values of the rate constants corresponding to the components Is_1- Is_4, Is_2 - Is_3respectively, are close to one another.

(3) The rate constants of the Is_2 and Is_3 central components of the initial thermal annealing process have higher values than the initial ones of the Is_1 and Is_4 side components.

In conclusion, the high values of the reaction order presented above, highlighted at 170°C kinetic study, are reliable proof that the ESR spectra of the L-α-anhydrous asparagines irradiated samples result from the overlapping spectra of three stable radicals at room temperature, specified in the radiolysis mechanism.

4 Radiolysis mechanism

In the literature there is only one information regarding the radical species formed on L–α-anhydrous asparagines irradiation[9] which contains the overlapping simulated three radicals spectra with the experimental EPR spectrum.

Direct ionization of the L-α-anhydrous asparagine molecule leads to the formation of the $Asn(COO)^{\cdot+}$ radical cation having the spin density located on the deprotonated carboxyl group. This species being unstable, dis-

Table 1. The orders and rate constants of reactions of thermal disappearance of the paramagnetic centers formed on the irradiation of the L-α-anhydrous asparagine, calculated for the four main components of the ESR spectrum at 180°C, 190°C, 200°C and 207°C

Temp, °C	Reaction order	k (s^{-1})				k, (s^{-1})
		I_{s1}	I_{s2}	I_{s3}	I_{s4}	
180 °C	3	2.78×10^{-4}	2.95×10^{-4}	3.28×10^{-4}	3.01×10^{-4}	$3.00\times10^{-4}\pm0.21$
190 °C	2.5	5.23×10^{-4}	5.15×10^{-4}	6.35×10^{-4}	6.21×10^{-4}	$5.73\times10^{-4}\pm0.63$
200 °C	2	6.05×10^{-4}	5.45×10^{-4}	5.96×10^{-4}	5.85×10^{-4}	$5.82\times10^{-4}\pm0.26$
207 °C	1	5.58×10^{-4}	5.73×10^{-4}	5.91×10^{-4}	6.01×10^{-4}	$5.80\times10^{-4}\pm0.19$

appears following two pathways that produce decarboxylation: first is CO_2 expulsion from the $Asn(COO)^{\cdot+}$ paramagnetic center accompanied by R_1 radical formation, a process that can occur simultaneously with ionization, the second pathway is the deprotonation of the amino group of $Asn(COO)^{\cdot+}$ radical followed by formation of the unstable radical $Asn(COO)^{\cdot}$ which decarboxylates to form the radical R_1'. The decarboxylation process is experimentally proven highlighting the CO_2 formation in L-α-anhydrous asparagine irradiated samples using gas chromatography method.[9]

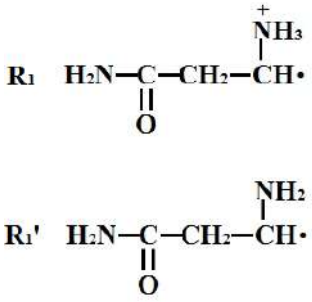

The existence of the two intense components of the EPR spectrum marked with a_1 and a_2 (Figure 2) could be attributed to the R_1 and R_1' entities since the odd electron located on the carbon atom interacts with α proton. After heating the irradiated sample, it is noted the three hyperfine splitting accentuation of the two spectral lines proving the increase of the odd electron interaction with the nitrogen atom of the amino group linked to the same carbon atom. The mass spectrometry study of similar structure amino acids by Zubavichus[16] led to the conclusion that the most unstable functional group of L-α-anhydrous asparagine is the amidic one. The direct ionization of L-α-anhydrous asparagine[9] also leads to the radical cation $Asn\ (CONH_2)^{\cdot+}$ formation having the spin density located on the amide group. This entity is unstable and the analysis of the experimental data obtained by ESR method as well as the calculation of the bonds dissociation energies[9] showed that the $Asn\ (CONH_2)^{\cdot+}$ radical cation performs the amide bond cleavage leading to R_2 radical formation.

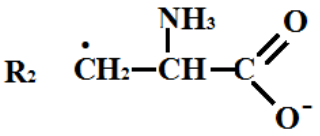

In the EPR spectrum of the irradiated L-α-anhydrous asparagine samples it was found the formation of four components resulted from the splitting of the two central lines marked with b_1 and b_2. This finding could be an argument to assign them to the R_2 radical due to the odd electron interaction with two non-equivalent α protons.

The radiolysis mechanism of L-α- anhydrous asparagine irradiated in the solid state at room temperature must include the formation of a radical anion.

In the primary interaction process, the expelled electron from the ionizing radiation after thermalization is captured by the carboxyl group of a parent molecule located at a certain distance from the ionizing site to form the $Asn^{\cdot-}$ anion.

In this radical, having an excess of negative charge, mutually neutralizes the positive charge of the amino group with the additional electron of the carboxyl group.

The entity resulting from this intramolecular electron transfer being unstable removes a hydrogen atom from the amino group. The hydrogen atom due to high reactivity extracts another hydrogen atom from the methylene group of the L-α-anhydrous asparagine molecule chain to form the deprotonated radical having the R_3 structure.[17]

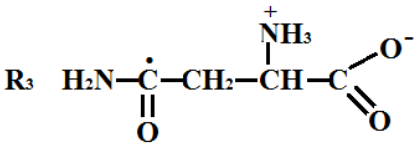

The formation of the R_3 radical is sustained by Strzelczak simulated spectrum.[9] In the present study, the formation of radicals R_1, R_2, R_3 through L-α- anhydrous asparagine irradiation at room temperature is justified by the kinetic results of thermal dissapearance characterized by superior and fractional order: the third order kinetics

Table 2. The rate constants for the radicals dissapearance at 170°C second order kinetics, according Waite model

170 °C							
I_{s1}	I_{s4}	I_{s1}	I_{s4}	I_{s2}	I_{s3}	I_{s2}	I_{s3}
$k_{A1}\times10^4$	$k_{A4}\times10^4$	$k_{B1}\times10^5$	$k_{B4}\times10^5$	$k_{A2}\times10^4$	$k_{A3}\times10^4$	$k_{B2}\times10^5$	$k_{B3}\times10^5$
3.15	3.05	2.71	2.87	4.01	4.33	1.74	2.43

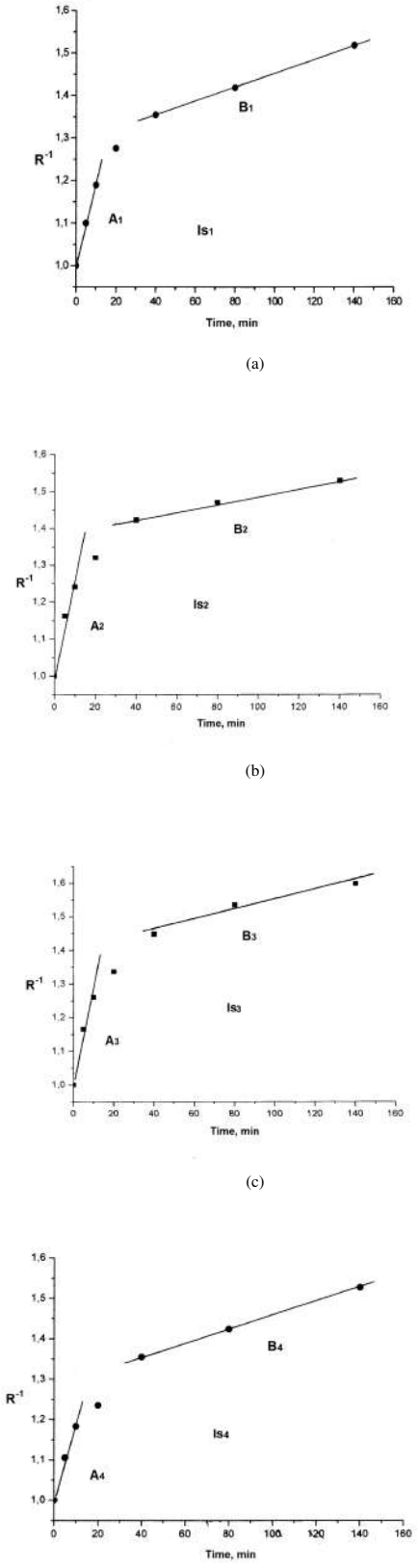

(a)

(b)

(c)

(d)

Figure 10. Variation of the R^{-1} ratio versus the isothermal heating time at 170°C for the disapearance of the radicals formed in L-α-anhydrous asparagines sample irradiated with a dose rate of 3×10^4 Gy, (a) Is_1, (b) Is_2, (c) Is_3, (d) Is_4

at 180°C proves the involvement of the three radicals. Decreasing the reaction order with temperature increasing is due to the disappearance of radicals with higher thermal resistance.

5 Conclusions

The primary process of L-α- anhydrous asparagine radiolysis consists in formation of two radical species: a radical cation and a radical anion. Theoretical and EPR study[9] have shown that at room temperature the radical cation decarboxylates and deamides to form the radicals R_1 and R_2, and the radical anion expels a hydrogen atom from the amide group and generates the radical R_3. From the present study of the thermal annealing of radicals it was found the following kinetic behaviors: higher reaction order and their gradual decrease from 3 to 1 with increasing temperature. The results of the kinetic study are a confirmation of the three radical species formation reported in the literature.

References

[1] Lund P. Nitrogen Metabolism in Mammalian, Applied Science, Barking, 1981.

[2] Robinson EN and Robinson BA. Deamidation of human proteins. Proceedings of the National Academy of Sciences, 2001, **98**(22): 12409-12414. https://doi.org/10.1073/pnas.221463198

[3] Hipkiss AR. On the "struggle between chemistry and biology during aging"-implications for DNA repair, apoptosis and proteolysis, and a novel route of intervention. Biogerontology, 2001, **2**(3): 173-178. https://doi.org/10.1023/A:1011599321168

[4] Bambai B, Rogee CE, Stec B, *et al*. Role of Asn-382 and Thr-383 in activation and inactivation of human prostaglandin H synthase cyclooxygenase catalysis. The Journal of Biological Chemistry, 2003, **279**: 4084-4092. https://doi.org/10.1074/jbc.M304762200

[5] Vijayakumar M, Qian H and Zhou HX. Hydrogen bonds between short polar side chains and peptides backbone: prevalence in proteins and effects on helix-forming propensities. Proteins, 1999, **34**: 497-507. https://doi.org/10.1002/(SICI)1097-0134(19990301)34:4⟨497::AID-PROT9⟩3.0.CO;2-G

[6] Cooper HJ, Hudgins RR, Hakanson K, *et al*. Characterization of amino acid side chain losses in electron capture dissociation. Journal of The American Society for Mass Spectrometry, 2002, **13**: 241-249. https://doi.org/10.1016/S1044-0305(01)00357-9

[7] Zhang P, Han S, Zhan Y, *et al*. Neutron spectroscopic and Raman studies of interaction between water and proline. Journal of Chemical Physics, 2008, **345**: 196-199.

[8] Box HC, Freund GH, Lilga TK, *et al*. Hyperfine couplings in primary radiation products. Journal of Chemical Physics, 1975, **63**: 2059-2063. https://doi.org/10.1063/1.431543

[9] Strzelczak G, Berges J, Housee-Levin C, *et al*. EPR spectroscopy and theoretical study of -irradiated asparagine and aspartic acid in solid state. Biophysical Chemistry, 2007, **125**: 92-103. https://doi.org/10.1016/j.bpc.2006.06.017

[10] Contineanu M. Thermal decay kinetics of the radicals generated during the radiolysis of polyacrylamide (PAA) hydrolized to different extents. Revue Roumaine de Chimie, 1996, **41**(9): 703-711.

[11] Contineanu M and Neacu A. Radical species formed by gamma radiolysis of polycrystalline telluric acid. Revue Roumaine de Chimie, 2006, **51**(11):1069-1078.

[12] Contineanu M and Neacu A. $PbCrO_4$ radiolysis impurified with CrO_3. Revista de Chimie (Bucharest), 2006, **57**(7): 706-710.

[13] Tria JJ, HoelD and Johnsen HR. The kinetics of radical decay in crystalline amino acids. 7. Monohydrates. Journal of Physical Chemistry, 1979, **83**(24): 3174-3179. https://doi.org/10.1021/j100487a022

[14] Waite RT. Theoretical Treatment of the Kinetics of Diffusion-Limited Reactions. Physical Review, 1957, **107**(2): 463-475. https://doi.org/10.1103/PhysRev.107.463

[15] Yung Y and Lee S. Equivalence of the radical recombination rate theories of Waite and Szabo. Chemical Physics Letters, 1994, **231**: 429-438. https://doi.org/10.1016/0009-2614(94)01282-2

[16] Zubavichus Y, Fuchs O, Weinhardt L, *et al*. Denlinger J D, Grunze M, Soft X-Ray-Induced Decomposition of Amino Acids: An XPS, Mass Spectrometry, and NEXAFS Study. Radiation Research, 2004, **161**(3): 346-358. https://doi.org/10.1667/RR3114.1

[17] Close MD, Fouse WG and Bernhard AW. ESR and ENDOR study of single crystals of L-asparagine-H_2O x-irradiated at room temperature. The Journal of Chemical Physics, 1977, **66**(4): 1534-1540. https://doi.org/10.1063/1.434117

Chem Rep, 2019, 1(1): 22-35
DOI: 10.25082/CR.2019.01.003

RESEARCH ARTICLE

Resultant gradient information, kinetic energy and molecular virial theorem

Roman F. Nalewajski

Abstract: Resultant *gradient*-information is introduced and applied to problems in chemical reactivity theory. This local measure of the structural information contained in (complex) wavefunctions of electronic states is related to the system overall kinetic energy combining the modulus (probability) and phase (current) contributions. The grand-ensemble representation of thermodynamic equilibria in open systems demonstrates the physical equivalence of the variational energetic and information principles. It is used and to relate the populational derivatives of *ensemble*-average functionals in both these representations, which represent reactivity criteria for diagnosing the charge-transfer (CT) phenomena. Their equivalence is demonstrated by using the in situ potential and hardness descriptors to predict the direction and optimum amount of CT. The virial theorem is generalized into thermodynamic quantities and used to extract the kinetic energy component from qualitative energy profiles in the bond-formation and (*exo/endo*)-ergic reactions. The role of electronic kinetic energy in such chemical processes is reexamined, the virial theorem implications for the Hammond postulate of reactivity theory are explored, and variations of the *structural*-information in chemical processes are addressed. The maximum thermodynamic information rule is formulated and "production" of the *gradient*-information in chemical reactions is addressed. The Hammond postulate is shown to be indexed by the geometric derivative of resultant *gradient*-information at transition-state complex.

Keywords: bond formation, chemical reactivity, grand ensemble, information theory, resultant information, virial theorem

1 Introduction

The Quantum Information Theory (QIT)[1–4] has been shown to provide a solid, unifying basis for understanding - in chemical terms - the electronic structure of molecules, and explaining general trends in their chemical behavior,[5–8] . Thermodynamic energy principle has been interpreted as physically equivalent rule for the resultant content of the overall *gradient*-information in electronic wavefunction, the dimensionless descriptor related to the state average kinetic energy. In the *grand*-ensemble both these variational principles determine the equilibrium state of an open molecular system. This equivalence parallels the same predictions resulting from the minimum-energy and maximum-entropy principles of the ordinary thermodynamics[9] . It explains the proportionality relations between energetic and informational criteria of chemical reactivity, measured by the corresponding populational derivatives of the *ensemble*-average functionals.

The QIT transcription of the variational principle for the electronic (thermodynamic) energy thus allows one to interpret reactivity criteria as the associated populational derivatives of the state resultant *gradient*-information (dimensionless kinetic energy) content. The latter combines the classical (probability) and nonclassical (current) contributions,due to the modulus and (local) phase components of the molecular wavefunction, respectively. The proportionality between the resultant *gradient*-information and the system kinetic energy also suggests the use of molecular virial theorem[10] in general reactivity considerations[5–8] .

To paraphrase Prigogine[11] , the electron density alone carries the information reflecting a "static" structure of "being", missing a "dynamic" structure of "becoming" contained in the state phase or current distributions. Both these manifestations of the electronic "organization" in molecular systems ultimately contribute to overall measures of the structural entropy or information content in generally complex wavefunctions, reflected

Received: March 4, 2019 **Accepted:** March 22, 2019 **Published:** March 25, 2019

***Correspondence to**: Roman F. Nalewajski, Department of Theoretical Chemistry, Jagiellonian University, Gronostajowa 2, 30-387 Cracow, Poland; Email: nalewajs@chemia.uj.edu.pl

Citation: Nalewajski RF. Resultant gradient information, kinetic energy and molecular virial theorem. *Chem Rep*, 2019, **1**(1): 22-35.

by the *resultant* QIT concepts[1–4] . Their classical contributions, conceptually rooted in Density Functional Theory (DFT)[12–17] , probe the entropic content of incoherent (disentangled) local "events", while the nonclassical terms provide the information supplement due to the coherence (entanglement) of such local events. The resultant measures allow one to distinguish the information content of states generating the same electron density but differing in their phase/current distributions, *e.g.*, the bonded (entangled) and nonbonded (disentangled) states of molecular fragments[18–27] .

The classical Information Theory (IT) of Fisher and Shannon[28–35] has been successfully applied to generate the chemical interpretation of molecular probability distributions,[36–39] . Information principles have been explored[5–8,40–45] and density pieces attributed to Atoms-in-Molecules (AIM) have been approached,[36–39,43–47] providing the information basis for the intuitive (stockholder) division of Hirshfeld[48] . Patterns of chemical bonds in molecules have been extracted from electronic orbital communications,[1,36–38,49–59] and entropy/information densities have been explored.[1,36–38,60,61] The nonadditive Fisher information[1,36–38,62,63] has been linked to the Electron Localization Function (ELF)[64–66] of modern DFT. This analysis has also formulated the Contragradience (CG) probe[1,36–38,67] for spatial localization of chemical bonds, and the Orbital Communication Theory (OCT) of the chemical bond has identified the *bridge*-bonds originating from the cascade propagations of information between AIM, which involve intermediate orbitals.[1,38,68–73] The DFT-based approaches to classical issues in reactivity theory[74–80] use the *energy*-centered arguments in justifying the observed reactivity preferences. It is the main purpose of this work to show that general reactivity rules can be alternatively treated using the *resultant*-information/*kinetic*-energy concepts of QIT.

We begin with a short summary of the overall *gradient*-information concept. The resultant QIT descriptor will be introduced and its classical and nonclassical components identified. Populational derivatives of its thermodynamic, *ensemble*-average value generate alternative indices of chemical reactivity, adequate in predicting both the direction and magnitude of electron flows in donor-acceptor systems[5–8] . The molecular virial theorem will be used to generate the information perspective on the bond-formation and the Hammond[81] postulate of reactivity theory. The theorem will be generalized to cover the *ensemble*-average energy components and the role of electronic kinetic energy or the resultant *gradient*-information in chemical processes will be examined. Physical equivalence of the energy and information reactivity descriptors in the *grand*-ensemble representation of *thermodynamic*-equilibria will be stressed, the relation between energetic and information reactivity indices will be examined, and the "production" of the overall structural information in chemical reactions will be addressed.

2 Resultant *gradient*-information and kinetic energy of electrons

Consider a general (complex) quantum state $|\psi\rangle$ of an electron described by the associated wavefunction in position representation,

$$\psi(r) = \langle r|\psi\rangle = R(r)exp[i\phi(r)] \tag{1}$$

with $R(\boldsymbol{r})$ and $\varphi(\boldsymbol{r})$ denoting its modulus and phase components, respectively. They determine the particle probability distribution,

$$p(r) = \psi(r)^{*}\psi(r) = R(r)^{2} \tag{2}$$

and the current density

$$\begin{aligned} j(r) &= [\hbar/(2mi)][\psi(r)^{*}\nabla\psi(r) - \psi(r)\nabla\psi(r)^{*}] \\ &= (\hbar/m)\,p(r)\,\nabla\phi(r) \equiv p(r)V(r) \end{aligned} \tag{3}$$

The effective velocity $\boldsymbol{V}(\boldsymbol{r})$ of this probability "fluid" measures the current-per-particle and reflects the state *phase*-gradient:

$$V(r) = j(r)/p(r) = (\hbar/m)\nabla\phi(r) \tag{4}$$

The average Fisher's[28] measure of the *classical gradient*-information for locality events contained in the electronic probability density $p(\boldsymbol{r})$ is reminiscent of von Weizscker's[82] inhomogeneity correction to density-functional for the kinetic-energy:

$$\begin{aligned} I[p] &= \int p(r)[\nabla lnp(r)]^{2}dr \equiv \int p(r)I_{p}(r)dr \\ &= 4\int [\nabla R(r)]^{2}dr \equiv I[R] \end{aligned} \tag{5}$$

Here $p(\boldsymbol{r})$ $I_p(\boldsymbol{r})$ denotes functional's overall density with $I_p(\boldsymbol{r})$ = $[\nabla \ln p(\boldsymbol{r})]^2$ standing for the associated density-per-electron. The amplitude form I[R] reveals that this classical descriptor reflects a magnitude of the state *modulus*-gradient. It characterizes an effective "narrowness" of the probability distribution, *i.e.*, a degree of determinicity in particle's position.

This *classical* functional of the *gradient*-information in probability distribution generalizes naturally into the of the quantum state $|\psi\rangle$, which combines the modulus

(probability) and phase (current) contributions.[1,18–22,62] It is defined by quantum expectation value of the Hermitian operator $\hat{\mathrm{I}}(r)$ of the overall gradient information[62] ,related to electronic *kinetic*-energy operator $\hat{T}(r)$,

$$\begin{aligned}\hat{I}(r) &= -4\Delta \ = (2i\nabla)^2 = \ (8m/\hbar^2)\hat{T}(r) \equiv \sigma\hat{T}(r)\\ \hat{T}(r) &= -\left[\hbar^2/\left(2m\right)\right]\nabla^2\end{aligned} \tag{6}$$

The integration by parts then gives the following expression for the average (resultant) *gradient*-information contained in quantum state $|\psi\rangle$:

$$\begin{aligned}I[\psi] &= \langle\psi|\hat{I}|\psi\rangle = -4\int \psi(r)^{*}\Delta\psi(r)dr\\ &= 4\int|\nabla\psi\left(r\right)|^2 dr \equiv \int p(r)I_{\psi}(r)d\mathbf{r}\\ &= I\left[p\right] + 4\int p(r)[\nabla\phi\left(r\right)]^2 dr\\ &\equiv \int p(r)[I_p\left(r\right) + I_{\phi}\left(r\right)]d\mathbf{r}\\ &\equiv I\left[p\right] + I[\phi] \equiv I[p,\phi]\\ &= I\left[p\right] + (2m/h)^2\int p(r)^{-1}j(r)^2 dr\\ &\equiv I\left[p\right] + I\left[j\right] \equiv I\left[p,j\right]\end{aligned} \tag{7}$$

This quantum *gradient*-information concept $I[\psi]$ = $I[p,\varphi]$ = $I[p,\boldsymbol{j}]$ is seen to combine the classical (probability) contribution $I[p]$ of Fisher and the corresponding nonclassical (phase/current) supplement $I[\varphi] = I[j]$. It also reflects the particle average (dimensionless) kinetic energy $T[\psi]$:

$$I[\psi] = \sigma\langle\psi|\hat{\mathrm{T}}|\psi\rangle T[\psi] = \sigma T[\psi] \tag{8}$$

The above *one*-electron development can be straightforwardly generalized into general *N*-electron state $|\Psi(N)\rangle$, exhibiting electron density $\rho(\boldsymbol{r})$= $Np(\boldsymbol{r})$, where $p(\boldsymbol{r})$ stands for its probability (shape) factor. The corresponding information operator then combines terms due to each electron,

$$\hat{I}(N) = \sum_{i=1}^{N}\hat{I}(r_i) = \sigma\sum_{i=1}^{N}\hat{T}(r_i) \equiv \sigma\hat{T}(N) \tag{9}$$

and determines the (dimensionless) average *gradient*-information as its expectation value proportional to the state average kinetic energy $T(N)$.

$$\begin{aligned}I(N) &= \left\langle\psi\left(N\right)|\hat{I}\left(N\right)\ |\psi\left(N\right)\right\rangle\\ &= \sigma\left\langle\psi\left(N\right)|\hat{T}\left(N\right)|\ \psi\left(N\right)\right\rangle = \sigma T(N)\end{aligned} \tag{10}$$

In the given electron (orbital) configuration specified by a single Slater determinant $\Psi(N) = |\psi_1\psi_2\ \ldots\psi_N|$, *e.g.*, in the familiar Hartree-Fock of Kohn-Sham theories, these *N*-electron descriptors combine the additive contributions due to all (singly occupied: $n_s = 1$), molecular orbitals (MO) $\psi = (\psi_1, \psi_2, \ldots, \psi_N) = \{\psi_s\}$:

$$\begin{aligned}T(N) &= \sum\nolimits_s n_s\langle\psi_s|\hat{T}|\psi_s\rangle \equiv \sum\nolimits_s n_s T_S\\ &= \sigma^{-1}\sum\nolimits_s n_s\langle\psi_s|\hat{I}|\psi_s\rangle \equiv \sigma^{-1}\sum\nolimits_s n_s I_s\end{aligned} \tag{11}$$

In the analytical LCAO MO representation, when these occupied MO are expressed as linear combinations of the (orthogonalized) atomic orbital (AO) basis $\chi = (\chi_1, \chi_2, \ldots, \chi_k, \ldots)$,

$$|\psi\rangle = |\chi\rangle C, C = \langle\chi|\psi\rangle = \{C_{k,s} = \langle\chi_\kappa|\psi_s\rangle\} \tag{12}$$

the average gradient information contained in $\Psi(N)$, for the unit matrix of MO occupations, $\mathbf{n} = \{n_s\delta_{s,s'} = \delta_{s,s'}\}$, thus reads:

$$\begin{aligned}I(N) &= \sum\nolimits_s n_s\langle\psi_s|\hat{I}|\psi_s\rangle\\ &= \sum\nolimits_\kappa\sum\nolimits_l\{\sum\nolimits_s C_{k,s}n_s C^{*}_{s,l}\}\langle\chi_l|\hat{I}|\chi_\kappa\rangle\\ &\equiv \sum\nolimits_k\sum\nolimits_l\gamma_{k,l}\mathrm{I}_{l,k} = tr(\gamma\mathrm{I})\end{aligned} \tag{13}$$

Here, the AO representation of the resultant *gradient*-information operator,

$$\mathrm{I} = \{I_{k,l} = \langle\chi_k|\hat{I}|\chi_l\rangle = \sigma\langle\chi_k|\hat{T}|\chi_l\rangle \equiv \sigma T_{k,l}\} \tag{14}$$

and the Charge/Bond-Order (CBO) (density) matrix of LCAO MO theory,

$$\gamma = CnC^{\dagger} = \langle\chi|\psi\rangle n\langle\psi|\chi\rangle \equiv \langle\chi|\hat{P}_{\psi}|\chi\rangle \tag{15}$$

represents the AO-representation of the projection operator onto the occupied MO-subspace,

$$\begin{aligned}\hat{P}_{\psi} &= N[\sum\nolimits_s|\psi_s\rangle(n_s/N)\langle\psi_s|]\\ &\equiv N[\sum\nolimits_s|\psi_s\rangle P_s\langle\psi_s|] \equiv N\hat{\mathrm{d}}\end{aligned} \tag{16}$$

proportional to the density operator $\hat{\mathrm{d}}$ of the configuration MO "ensemble".

This expression for the average overall *gradient*-information assumes thermodynamic-like form, as trace of the product of CBO matrix, the AO representation of the (occupation-weighted) MO projector, which establishes the configuration density operator $\hat{\mathrm{d}}$, and the corresponding AO matrix of the Hermitian operator for the resultant *gradient*-information, related to the system electronic kinetic energy. In this MO "ensemble" averaging the AO information matrix **I** constitutes the *quantity*-matrix, while the CBO (density) matrix γ pro-

vides the "geometrical" *weighting*-factors reflecting the system electronic state. It has been argued elsewhere that elements of the CBO matrix also generate amplitudes of electronic communications between molecular AO "events".[1,36–38,49–59] This observation adds a new angle to interpreting the average-information expression as the *communication*-weighted (dimentionless) kinetic energy of the system electrons[83] .

A separation of the *modulus*- and *phase*-components of general *N*-electron states calls for wavefunctions yielding the specified electron density[14] . It can effected using the Harriman-Zumbach-Maschke (HZM)[84,85] construction of DFT, which uses *N* (complex) *equidensity orbitals*, each separately generating the *molecular* probability distribution $p(\boldsymbol{r})$ and exhibiting the *density*-dependent spatial phase which safeguards the MO orthogonality.

3 Grand-ensemble description of molecular equilibria

In an *open* molecule M(v), identified by the external potential $v(\boldsymbol{Q})$ of the Born-Oppenheimer (BO) approximation for the molecular geometry $\boldsymbol{Q}$ specified by coordinates of the fixed nuclei of the system constituent atoms, the populational derivatives of the average electronic energy or the resultant *gradient*-information call for the *grand*-ensemble representation of thermodynamic equilibria.[5–8,15,86,87] A molecule is then coupled to a hypothetical (macroscopic) electron reservoir R(μ) exhibiting the chemical potential μ, and the heat bath B(T) identified by its absolute temperature T in the composite (macroscopic) system

$$M(\mu,T;v) = [R(\mu)M(v)B(T)] \tag{17}$$

where the vertical *broken* lines separating subsystems symbolize their freedom to exchange electrons or energy. The average number of electrons in such an *externally*-open molecule,

$$\begin{aligned} \langle \mathrm{N} \rangle_{ens.} \equiv N &= tr(\hat{D}\hat{N}) = \sum\nolimits_i P_i N_i \\ \sum\nolimits_i P_i &= 1, \quad P_i \geqslant 0 \end{aligned} \tag{18}$$

exhibits a continuous (fractional) spectrum of values, thus justifying the very concept of the populational (N) *derivative* itself. Here,

$$\hat{N} = \sum\nolimits_i \sum\nolimits_j |\psi_j(N_i)\rangle N_i \langle \psi_j(N_i)| \tag{19}$$

stands for the particle-number operator in Fock's space and the density operator identifies the equilibrium statistical mixture of the system stationary states $\{|\psi_j[N_i,v]\rangle \equiv |\psi_j{}^i\rangle\}$,

$$\hat{D}(\mu,T;v) = \sum\nolimits_i \sum\nolimits_j |\psi_j(N_i)\rangle P_j{}^i(\mu,T;v) \langle \psi_j(N_i)| \tag{20}$$

eigenstates of Hamiltonians $\{\hat{\mathrm{H}}(N_i,v) \equiv \hat{\mathrm{H}}_i\}$ for different (integer) numbers of electrons $\{N_i \equiv i\}$ corresponding to energies $\{E_j[N_i,v] \equiv E_j{}^i\}$,

$$\begin{aligned} &\hat{H}(N_i,v)|\psi_j[N_i,v]\rangle = E_j(N_i)|\psi_j[N_i,v]\rangle \\ &or \quad \hat{H}|\psi_j{}^i\rangle = E_j{}^i|\psi_j{}^i\rangle \end{aligned} \tag{21}$$

these (pure) quantum states appear in the *grand*-ensemble with the (*externally*-imposed) equilibrium thermodynamic probabilities $\{P_j{}^i(\mu, T; v) \equiv P_j{}^i \geq 0\}$ and the "condensed" probability in Equation 18 is obtained by the partial summation over eigenstates of $\hat{\mathrm{H}}_i$: $P_i = \sum_j P_j{}^i$.

Such electronic N-derivatives are involved in definitions of the system Charge Transfer (CT) criteria of chemical reactivity,[15,74–79] *e.g.*, the chemical potential (negative electronegativity)[15,86–90] or the hardness (softness)[91] and Fukui Function (FF)[92] descriptors of electrons. They are thus definable only for the *mixed*-state of the molecular (microscopic) system M(v), *e.g.*, that corresponding to the thermodynamic equilibrium imposed by intensities (μ, T) characterizing the external (macroscopic) subsystems R(μ) and B(T) in M(μ, T; v), $\mu = \mu_R$ and $T = T_B$, *i.e.*, for the equilibrium *grand*-canonical density operator of Equation 20: $\hat{\mathrm{D}}_{eq.} \equiv \hat{D}(\mu,T;v)$.

The *grand*-canonical intensities determine the ensemble thermodynamic potential, called the *grand*-potential, given by the corresponding Legendre-transform[9] of the *ensemble*-average energy

$$\begin{aligned} \langle E \rangle_{ens.} \equiv E[\hat{D}] &\equiv E(N,S;v) = tr(\hat{D}\hat{H}) \\ &= \sum\nolimits_i \sum\nolimits_j P_j{}^i E_j{}^i \end{aligned} \tag{22}$$

$$\begin{aligned} \Omega &= E - (\partial E/\partial N)N - (\partial E/\partial S)S \\ &= E[\hat{D}] - \mu N[\hat{D}] - TS[\hat{D}] \end{aligned} \tag{23}$$

It minimizes at the optimum *state*-probabilities $\{P_j{}^i(\mu,T;v)\} \equiv \boldsymbol{P}_{eq.}(\mu,T;\boldsymbol{Q})$:

$$\begin{aligned} \min_{\hat{\mathrm{D}}} \Omega[\hat{\mathrm{D}}] &= \Omega[\hat{\mathrm{D}}(\mu,T;v)] \\ &= E[\hat{\mathrm{D}}_{eq.}] - \mu N[\hat{\mathrm{D}}_{eq.}] - TS[\hat{\mathrm{D}}_{eq.}] \\ &\equiv \Omega(\mu,T;v) \Rightarrow P_{eq.}(\mu,T;Q) \end{aligned} \tag{24}$$

As indicated in the preceding equation, the ensemble parameters μ and T ultimately determine the associ-

ated optimum probabilities of the (pure) stationary states $\{|\psi_j[N_i,v]\rangle\}$, eigenstates of Hamiltonians $\{\hat{\mathrm{H}}_i\}$,

$$\{P_j{}^i(\mu,\mathrm{T};v) = \Xi^{-1}exp[\beta(\mu N_i - E_j{}^i)]\} \equiv P_{eq.}(\mu,T;Q) \quad (24\text{-}1)$$

which define the equilibrium density operator of Equation 20 for the specified geometrical structure $\boldsymbol{Q}$. Here Ξ stands for the *grand*-ensemble partition function, k_B denotes the Boltzmann constant, and $\beta = (k_BT)^{-1}$.

The *electronically*-relaxed, equilibrium ensemble probabilities thus satisfy the following relations between the probability "gradients" for the adopted molecular geometry $\boldsymbol{Q}$:

$$\left.\frac{\partial\Omega(P,Q)}{\partial P}\right|_{P_{eq.}} = 0 \quad \text{or}$$
$$\left.\frac{\partial E(P,Q)}{\partial P}\right|_{P_{eq.}} = \mu\left.\frac{\partial N(P)}{\partial P}\right|_{P_{eq.}} + T\left.\frac{\partial S(P)}{\partial P}\right|_{P_{eq.}} \quad (25)$$

where the explicit dependence of on nuclear coordinates $\boldsymbol{Q}$, resulting from the external potential contribution in the ensemble Hamiltonians $\{\hat{H}_i\}$,also influences eigenvalues$\{E_j{}^i\}$.

The *grand*-potential corresponds to replacing the "extensive" *state*-parameters, of the average values of the particle number $\boldsymbol{N} = N[\hat{\mathrm{D}}]$ and thermodynamic entropy[93]

$$S[\hat{D}] = tr(\hat{D}\hat{S}) = -k_B\sum_i\sum_j P_j{}^i lnP_j{}^i$$
$$\hat{S} = -k_B\sum_i\sum_j |\psi_j{}^i\rangle lnP_j{}^i\langle\psi_j{}^i| \quad (26)$$

bytheir "intensive" conjugates: the chemical potential μ and absolute temperature *T*, respectively. This Legendre-transform includes these "intensities" as Lagrange multipliers enforcing, at the minimum of , the constraints of the specified values of the system *ensemble*-average values of the conjugate "extensive" parameters: the system overall number of electrons,

$$\langle N\rangle_{ens.} = N[\hat{D}_{eq.}] = \sum_i[\sum_j P_j{}^i(\mu,T;v)]N_i = \sum_i P_i(\mu,T;v)N_i = \langle N(\mu,T;v)\rangle_{ens.} = N[\mu,T;v] = N \quad (27)$$

and of thermodynamic (von Neumann's[93]) entropy:

$$\langle S\rangle_{ens.} = S[\hat{D}_{eq.}] = -k_B\sum_i\sum_j P_j{}^i(\mu,T;v)lnP_j{}^i(\mu,T;v) = \langle S(\mu,T;v)\rangle_{ens.} = S(\mu,T) = S \quad (28)$$

In equilibrium state the prescribed average extensive descriptors *N* and *S* also uniquely identify the externally-imposed state intensities, $\mu = \mu(N,S)$and$T = T(N,S)$, and hence also the equilibrium energy function

$$E[\hat{D}_{eq.}] = \langle E(\mu,T;v)\rangle_{ens.} = \sum_i\sum_j P_j{}^i(\mu,T;v)\langle\psi_j{}^i|\hat{H}_i|\psi_j{}^i\rangle = \sum_i\sum_j P_j{}^i(\mu,T;v)E_j{}^i = E(\mu,T) \equiv E(N,S) \quad (29)$$

It allows one to formally identify the intensive parameters as its partial derivatives with respect to the constrained values of the extensive state-variables:

$$\mu = \left(\frac{\partial E}{\partial N}\right)_S\Big|_{\hat{\mathrm{D}}_{eq.}} \text{ and } T = \left(\frac{\partial E}{\partial S}\right)_N\Big|_{\hat{\mathrm{D}}_{eq.}} \quad (30)$$

In the $T\rightarrow 0$ limit[15,86,87] only two *ground*-states ($j = 0$), $\{|\psi_0{}^i\rangle, |\psi_0{}^{i+1}\rangle\}$, corresponding to the neighboring integers "bracketing" the given (fractional) $\langle N\rangle_{ens.} = N$, $N_i \leq \langle N\rangle_{ens.} \leq N_i + 1$, appear in the equilibrium statistical mixture. Their ensemble probabilities for the specified

$$\langle N\rangle_{ens.} = iP_i + (i+1)(1-P_i) = N \quad (31)$$

then read:

$$P_i = 1 + i - N \equiv 1 - \omega \text{ and } P_{i+1} = N - i \equiv \omega \quad (32)$$

The continuous energy function *E*(*N*,*S*) then consists of the straight-line segments between the neighboring integer values of *N*. This implies constant values of the chemical potential in all such admissible ranges of the average electron number and μ-discontinuity at $N = N_i$(integer).[15,86,87]

The *ensemble*-average value of the resultant *gradient*-information,

$$\langle I\rangle_{ens.} \equiv I[\hat{D}_{eq.}] = tr\,[\hat{D}_{eq.}\hat{I}] = \sum_i\sum_j P_j{}^i(\mu,T;v)\langle\psi_j{}^i|\hat{I}(N_i)|\psi_j{}^i\rangle \equiv \sum_i\sum_j P_j{}^i(\mu,T;v)I_j{}^i$$
$$I_j{}^i = (8m/\hbar^2)\langle\psi_j{}^i|\hat{T}(N_i)|\psi_j{}^i\rangle \equiv \sigma T_j{}^i \quad (33)$$

is related to the *ensemble*-average kinetic energy $\boldsymbol{T}$:

$$\begin{aligned}\langle T\rangle_{ens.} &\equiv I[\hat{D}_{eq.}] = tr(\hat{D}_{eq.}\hat{T}) \\ &= \sum_i\sum_j P_j{}^i(\mu,T;v)\langle\psi_j{}^i|\hat{T}(N_i)|\psi_j{}^i\rangle \\ &\equiv \sum_i\sum_j P_j{}^i(\mu,T;v)T_j{}^i = \sigma^{-1}\langle I\rangle_{ens.}\end{aligned} \tag{34}$$

The proportionality constant results from relation between the associated electronic operators:

$$\begin{aligned}\hat{T}(N_i) &= \frac{-\hbar^2}{2m}\sum_{k=1}^{N_i}\nabla_k^2 \qquad and \\ \hat{I}(N_i) &= -4\sum_{k=1}^{N_i}\nabla_k^2\end{aligned} \tag{35}$$

Therefore, the thermodynamic rule of Equation 24, for the minimum of the constrained average value of electronic energy can be alternatively interpreted as the corresponding extremum principle for the *ensemble*-average (resultant) *gradient*-information:[5–8,36–38,40]

$$\begin{aligned}&\sigma \min_{\hat{\mathrm{D}}}\Omega[\hat{\mathrm{D}}] = \sigma\Omega[\hat{\mathrm{D}}_{eq.}] \\ &= I[\hat{\mathrm{D}}_{eq.}] + \sigma\{W[\hat{\mathrm{D}}_{eq.}] - \mu N[\hat{\mathrm{D}}_{eq.}] - TS[\hat{\mathrm{D}}_{eq.}]\}\end{aligned} \tag{36}$$

where the *ensemble*-average value of the system overall potential energy,

$$W[\hat{\mathrm{D}}_{eq.}] = V[\hat{\mathrm{D}}_{eq.}] + U[\hat{\mathrm{D}}_{eq.}] \tag{37}$$

combines the nuclear-attraction ($V[\hat{\mathrm{D}}_{eq.}]$) and electron-repulsion ($U[\hat{\mathrm{D}}_{eq.}]$) contributions. This information principle is seen to contain an additional constraint of the fixed potential energy, $\langle W\rangle_{ens.} = \boldsymbol{W}$, multiplied by the Lagrange multiplier

$$\lambda_W = -\sigma = \left(\frac{\partial I}{\partial W}\right)_{N,S}\Big|_{\hat{\mathrm{D}}_{eq.}} \equiv K \tag{38}$$

besides the remaining constraints, now multiplied by the "scaled" conjugate intensities[5–8] : information "*potential*"

$$\xi \equiv \sigma\mu = \left(\frac{\partial I}{\partial N}\right)_{W,S}\Big|_{\hat{\mathrm{D}}_{eq.}} \tag{39}$$

information "*temperature*"

$$\tau \equiv \sigma T = \left(\frac{\partial I}{\partial S}\right)_{W,N}\Big|_{\hat{\mathrm{D}}_{eq.}} \tag{40}$$

The conjugate thermodynamic principles, for constrained extrema of the ensemble energy,

$$\delta\Big(E[\hat{\mathrm{D}}] - \mu N[\hat{\mathrm{D}}] - TS[\hat{\mathrm{D}}]\Big)_{\hat{\mathrm{D}}_{eq.}} = 0 \tag{41}$$

and its overall *gradient*-information,

$$\delta\left(I[\hat{\mathrm{D}}] - \kappa W[\hat{\mathrm{D}}] - \xi N[\hat{\mathrm{D}}] - \tau S[\hat{\mathrm{D}}]\right)_{\hat{\mathrm{D}}_{eq.}} = 0 \tag{42}$$

have the same optimum-probability solutions of Equation 25. This manifests the physical equivalence of the energetic and "entropic" principles in determining the equilibrium states in thermodynamics[9] .

Several N-derivatives of the *ensemble*-average electronic energy or of the resultant *gradient*-information define useful and adequate CT criteria of chemical reactivity.[15,74–79] The physical equivalence of the energy and information principles indicates that such concepts are mutually related, being both capable of describing the electron-transfer phenomena in donor-acceptor systems[5–8] . The above ensemble interpretation also applies to diagonal and mixed *second* derivatives of the electronic energy or its kinetic-energy (information) component, which involve the population differentiation.

In *energy*-representation the *chemical hardness*[91] , the "diagonal" populational *second*- derivative of the ensemble energy, reflects the *N*-derivative ofchemical potential,

$$\eta = \left(\frac{\partial^2 E}{\partial N^2}\right)_S\Big|_{\hat{\mathrm{D}}_{eq.}} = \left(\frac{\partial\mu}{\partial N}\right)_S\Big|_{\hat{\mathrm{D}}_{eq.}} > 0 \tag{43}$$

while the *information* "hardness" reflects the *N*-derivative of information "*potential*"[5–8] :

$$\omega = \left(\frac{\partial^2 I}{\partial N^2}\right)_{W,S}\Big|_{\hat{\mathrm{D}}_{eq.}} = \left(\frac{\partial\xi}{\partial N}\right)_{W,S}\Big|_{\hat{\mathrm{D}}_{eq.}} = \sigma\eta > 0 \tag{44}$$

The positive signs of these diagonal population derivatives assure the *external* stability of an open M(v), with respect to hypothetical electron flows between molecular system and its reservoir. They indeed imply an increase (a decrease) of the global energetic and information "intensities" coupled to $\boldsymbol{N}$, μ and ξ, in response to perturbations created by the initial electron inflow (outflow). This accords with the Le Chtelier and Le Chtelier-Braun principles of thermodynamics[9] , that spontaneous responses in system intensities to the initial population displacements diminish effects of the primary perturbations.

By the *cross*-differentiation identity the "*mixed*" *second*-derivative of the ensemble energy, measuring the system global FF[92] , can be alternatively interpreted as either the response in global chemical potential per unit

displacement in the external potential, or the density response per unit populational displacement.

$$f(r) = \left(\frac{\partial^2 E}{\partial N \partial v(r)}\right)_S\Big|_{\hat{\mathrm{D}}_{eq.}} = \left(\frac{\partial \mu}{\partial v(r)}\right)_S\Big|_{\hat{\mathrm{D}}_{eq.}} = \left(\frac{\partial \rho(r)}{\partial N}\right)_S\Big|_{\hat{\mathrm{D}}_{eq.}} \quad (45)$$

The associated mixed derivative of the resultant gradient information in the *grand*-ensemble similarly reads:

$$\varphi r = \left(\frac{\partial^2 I}{\partial N \partial v(r)}\right)_{W,S}\Big|_{\hat{\mathrm{D}}_{eq.}} = \left(\frac{\partial \xi}{\partial v(r)}\right)_{W,S}\Big|_{\hat{\mathrm{D}}_{eq.}} = \sigma \left(\frac{\partial \rho(r)}{\partial N}\right)_{W,S}\Big|_{\hat{\mathrm{D}}_{eq.}} = \sigma\, f(r) \quad (46)$$

It has been argued elsewhere[5–8] , that the *in situ* measures of these energy and information derivatives constitute fully equivalent descriptors of electron flows between the polarized subsystems. These CT phenomena in the polarized reactive system $\mathrm{R}^+ = (\mathrm{A}^+|\mathrm{B}^+)$, containing the *mutually*-closed and molecularly polarized *acceptor* (acid, A) and *donor* (basis, B) reactants $\{\alpha^+\}$, are described by populational derivatives: the substrate chemical potentials $\mu_R{}^+ = \{\mu_a{}^+\}$ and elements of the hardness matrix $\eta_R{}^+ = \{\eta\alpha_{,\beta}\}$. These descriptors again call for the *grand*-ensemble representation of the polarized (*externally*-open) reactants, in contact with their separate (macroscopic) electron reservoirs $\{R_a\}$. They represent the electron population $\{N_a \equiv N_a\}$ derivatives of the *ensemble*-average electronic energy in R^+, $E[\{N_\beta\}, v] \equiv E_v(\{N_\beta\})$, the microscopic subsystem in the macroscopic (composite) system,

$$\begin{aligned} M_R{}^+ &= (M_A{}^+|M_B{}^+) \\ &= (R_A A^+|B^+ R_B) \\ &\equiv (R_A M(v)^+ R_B) \end{aligned} \quad (47)$$

where the solid and broken vertical lines separating subsystems again denote their mutual closeness and openness, respectively, with respect to hypothetical flows of electrons. They are calculated for the fixed molecular external potential $v(\boldsymbol{Q})$ reflecting the "frozen" molecular geometry $\boldsymbol{Q}$.

The *in situ* descriptors of CT are thus derived from the corresponding partials of the system *ensemble*-average energy with respect to *ensemble*-average electron populations $\{\mathrm{N}_a\}$ on (*externally*-open) *molecular*-subsystems $\{\alpha^+\}$ in the (*mutually*-closed) *composite* fragments $\{M_a{}^+ = (a^+ R_a)\}\ of\ M_R{}^+$:

$$\begin{aligned} \mu_a &\equiv \partial E_v(\{N_\gamma\})/\partial N_a \\ \eta_{\alpha,\beta} &= \partial^2 E_v(\{N_\gamma\})/\partial N_\alpha \partial N_\beta = \partial \mu_\alpha/\partial \mathrm{N}_\beta \\ &= \partial \mu_\beta/\partial \mathrm{N}_\alpha = \eta_{\beta,\alpha} \end{aligned} \quad (48)$$

The optimum amount of the (fractional) CT is determined by the difference in chemical potentials of the (equilibrium) polarized reactants in R^+,

$$\mu_{CT} = \partial E_v\left(N_{CT}\right)/\partial N_{CT} = \mu_{\mathrm{A}}{}^+ - \mu_{\mathrm{B}}{}^+ < 0 \quad (49)$$

which defines the effective CT-gradient, and the *in situ* hardness (η_{CT}) or softness (S_{CT}) for this process,

$$\begin{aligned} \eta_{CT} &= \partial \mu_{CT}/\partial N_{CT} \\ &= (\eta_{\mathrm{A,A}} - \eta_{\mathrm{A,B}}) + (\eta_{\mathrm{B,B}} - \eta_{\mathrm{B,A+}}) \equiv \eta_{\mathrm{A}}{}^{\mathrm{R}} + \eta_{\mathrm{B}}{}^{\mathrm{R}} \\ &\equiv {\Sigma_{CT}}^{-1} \end{aligned} \quad (50)$$

representing the effective CT-Hessian and its inverse, respectively. The optimum amount of the *inter*-reactant CT,

$$N_{CT} = -\mu_{CT} S_{CT} = -\mu_{CT}/\eta_{CT} \quad (51)$$

then generates the associated (2^{nd}-order) stabilization energy:

$$E_{CT} = \mu_{CT} N_{CT}/_2 = -{\mu_{CT}}^2 S_{CT}/_2 < 0 \quad (52)$$

The corresponding CT-derivatives of the average *gradient*-information in AB systems similarly involve the *in situ* information potential,

$$\xi_{CT} = \partial I\left(N_{CT}\right)/\partial N_{CT} = \xi_A{}^+ - \xi_B{}^+ = \sigma \mu_{CT} \quad (53)$$

and the associated hardness descriptor, the inverse of the information softness θ_{CT},

$$\omega_{CT} = \partial \xi_{CT}/\partial N_{CT} \equiv {\theta_{CT}}^{-1} = \sigma \eta_{CT} = \sigma\ {S_{CT}}^{-1} \quad (54)$$

In terms of these information descriptors the amount of CT in the acid-base system reads:

$$\begin{aligned} N_{CT} &= -\xi_{CT}/\omega_{CT} = -\xi_{CT}\theta_{CT} \\ &= -\mu_{CT}/\eta_{CT} = -\mu_{CT} S_{CT} \end{aligned} \quad (55)$$

Thus, the *in situ* populational derivatives (ξ_{CT}, $\omega_{CT} = {\theta_{CT}}^{-1}$) of the *ensemble*-average measures of the (resultant) *gradient*-information functionals, provide alternative reactivity descriptors, fully equivalent to the chemical potential and hardness/softness indices (μ_{CT}, $\eta_{CT} = {S_{CT}}^{-1}$) of the energy representation. This demonstrates the physical equivalence of the energy and information treatments of CT phenomena in molecular systems. One thus concludes

that the resultant *gradient*-information, the quantum generalization of the classical Fisher measure, indeed constitutes a reliable basis for an "entropic" description of reactivity phenomena.

4 Virial theorem implications

The virial theorem for the stationary electronic states $|\psi_j{}^i\rangle = |\psi_j[N_i,v]\rangle$ in molecules reflects homogeneities of the kinetic and potential energy contributions in such *pure* quantum states,

$$T_j{}^i = \langle\psi_j{}^i|\hat{T}(N_i)|\psi_j{}^i\rangle \text{ and } W_j{}^i = \langle\psi_j{}^i|\hat{W}(N_i,v)|\psi_j{}^i\rangle$$
$$\hat{W}(N_i,v) = \sum_{k=1}^{N_i}[v(k) + \frac{1}{2}\sum_{l\neq k} g(k,l)]$$
$$= \hat{V}(N_i,v) + \hat{U}(N_i,v) \tag{56}$$

with respect to the uniform scaling of the system electronic and nuclear positions. Here, $g(k,l)$ denotes the repulsion between electrons k and l, and the state electronic energy in $|\psi_j{}^i\rangle$

$$E_j{}^i = \langle\psi_j{}^i|\hat{H}_i|\psi_j{}^i\rangle = T_j{}^i + W_j{}^i \tag{57}$$

In BO approximation both this average energy and its components are parametrically dependent upon molecular geometry specified by the fixed (Cartesian) coordinates $\boldsymbol{Q}$ of the nuclei, and so are the energy differences with respect to the adopted reference, *e.g.*, the Separated Atoms Limit (SAL) or the separated reactants,

$$\begin{aligned} E_j{}^i(Q) &= T_j{}^i(Q) + W_j{}^i(Q) \quad \textit{and} \\ \Delta E_j{}^i(Q) &= \Delta T_j{}^i(Q) + \Delta W_j{}^i(Q) \end{aligned} \tag{58}$$

The molecular virial theorem for the pure stationary state in BO approximation reads[10] :

$$2T_j{}^i(Q) + W_j{}^i(Q) + Q\cdot[\partial E_j{}^i(Q)/\partial Q]$$
$$\equiv 2T_j{}^i(Q) + W_j{}^i(Q) + Q\cdot\nabla_Q E_j{}^i(Q) = 0 \tag{59}$$

It extracts the kinetic and potential components of the overall electronic energy for the current geometrical structure of the molecular system,

$$\begin{aligned} T_j{}^i(Q) &= -E_j{}^i(Q) - Q\cdot\nabla_Q E_j{}^i(Q) \quad \textit{and} \\ W_j{}^i(Q) &= 2E_j{}^i(Q) + Q\cdot\nabla_Q E_j{}^i(Q) \end{aligned} \tag{60}$$

or similarly partitions the relative energies $\Delta E_j{}^i(\boldsymbol{Q})$ of Equation 58.

These relations assume a particularly simple form for the energetical *profiles*, sections of the BO Potential Energy Surface (PES), *e.g.*, the energy function in diatomics, for which the internuclear distance R uniquely specifies the molecular geometry, or along the reaction-coordinate (RC) $\boldsymbol{R}_c$ in chemical processes, with the trajectory arc-length $P = |\boldsymbol{R}_c|$ determining the reaction-progress variable. In diatomics the virial theorem expressed in terms of energy changes relative to SAL reads:

$$\begin{aligned} &2\Delta T_j{}^i(R) + \Delta W_j{}^i(R) + R[d\Delta E_j{}^i(R)/dR] = 0 \quad or \\ &\Delta T_j{}^i(R) = -\Delta E_j{}^i(R) - R[d\Delta E_j{}^i(R)/dR] \\ &\qquad = -d[R\Delta E_j{}^i(R)]/dR \quad and \\ &\Delta W_j{}^i(R) = 2\Delta E_j{}^i(R) + R[d\Delta E_j{}^i(R)/\partial R] \\ &\qquad = R^{-1}d[R^2\Delta E_j{}^i(R)]/dR \end{aligned} \tag{61}$$

The virial theorem is satisfied in each stationary state $|\psi_j{}^i\rangle$ of the molecular system under consideration. Therefore, it is also obeyed by the *ensemble*-average components corresponding to thermodynamic equilibria. Indeed, multiplying Equation 59 and Equation 60 by the *ensemble*-probabilities $\{P_j{}^i(\mu,T;v)\} \equiv \boldsymbol{P}(\mu,T;\boldsymbol{Q})\}$, from the *grand*-canonical equilibrium principle of Equation 24 and Equation 25, and summing over all stationary states involved in this statistical mixture gives directly the associated thermodynamic relations:

$$\begin{aligned} &2T(Q) + W(Q) + Q\cdot\nabla_Q E(Q) = 0 \quad or \\ &T(Q) = -E(Q) - Q\cdot\nabla_Q E(Q) \quad and \\ &W(Q) = 2E(Q) + Q\cdot\nabla_Q E(Q) \end{aligned} \tag{62}$$

They determine both the system thermodynamic energy,

$$E[\hat{D}_{eq.}] = T[\hat{D}_{eq.}] + W[\hat{D}_{eq.}] \tag{63}$$

its kinetic component $T[\hat{D}_{eq.}] = \sigma^{-1}I[\hat{D}_{eq.}]$ proportional to the associated overall *gradient*-information descriptor $I[\hat{D}_{eq.}]$, and the *ensemble*-average potential energy

$$\begin{aligned} W[\hat{D}_{eq.}] &= \langle W\rangle_{ens.} = tr\,(\hat{D}_{eq.}\hat{W})Q_{eq.} \\ &= \sum_i\sum_j P_j{}^i(\mu,T;v)\langle\psi_j{}^i|\hat{W}(N_i,v)|\psi_j{}^i\rangle \\ &\equiv \sum_i\sum_j P_j{}^i(\mu,T;v)W_j{}^i \end{aligned} \tag{64}$$

One observes that this generalized, *mixed*-state partitioning also includes the *pure*-state relations of Equation 58 and Equation 59 as the special (*micro*-canonical) case corresponding to $P_j{}^i = 1$ and $\{P_{l\neq j}^{k\neq i} = 0\}$.

Let us briefly examine some implications of this general balance between the kinetic and potential components of the thermodynamic value of electronic energy. For the *energy*-minimum geometry $Q_{eq.}(E) = Q_{eq.}$, determined by the vanishing gradient of thermodynamic

energy,

$$\nabla_Q E|_{eq.} = 0 \tag{65}$$

the thermodynamic virial relations simplify:

$$\begin{aligned} &T\left(Q_{eq.}\right) = -E\left(Q_{eq.}\right) = \sigma^{-1} I\left(Q_{eq.}\right) \quad and \\ &W\left(Q_{eq.}\right) = 2E\left(Q_{eq.}\right) \end{aligned} \tag{66}$$

For such a *geometrically*-relaxed structure the *minimum*-energy principle of thermodynamics thus implies the thermodynamic *maximum*-information rule in QIT:

$$\begin{aligned} \{min_P[E\left(P\right)]_{\mu,T;Qeq.} &\Rightarrow max_P[I\left(P\right)]_{\mu,T;Qeq.}\} \\ &\Rightarrow P(\mu,T;Q)\} \end{aligned} \tag{67}$$

Inother words, in thermodynamic (*electronically*-relaxed) equilibrium the *geometrically*-relaxed molecular systems assume the maximum resultant *gradient*-information related to its average kinetic energy. This information principle complements the familiar *maximum*-entropy rule of ordinary thermodynamics[9] .

It should be observed that the *energy*-optimum structure $\boldsymbol{Q}_{eq.}(E\ )$ of Equation 65 differs from that determined by the vanishing geometric gradient of the *grand*-potential,

$$\left.\frac{\partial\Omega(P,Q)}{\partial Q}\right|_{\bar{Q}_{eq.}} = 0 \ \Rightarrow\ Q_{eq.}(\Omega) = \bar{Q}_{eq.} \neq Q_{eq.} \tag{68}$$

since then

$$\begin{aligned} \left.\frac{\partial E(P,Q)}{\partial Q}\right|_{\bar{Q}_{eq.}} &= \mu \left.\frac{\partial N(P)}{\partial Q}\right|_{\bar{Q}_{eq.}} + T \left.\frac{\partial S(P)}{\partial Q}\right|_{\bar{Q}_{eq.}} \\ &= \left(\mu\frac{\partial N(P)}{\partial P} + T\frac{\partial S(P)}{\partial P}\right)\left(\frac{\partial P}{\partial Q}\right)\Bigg|_{\bar{Q}_{eq.}} \end{aligned} \tag{69}$$

Consider now the *pure*-state (*micro*-canonical) case summarized by the virial relations of Eqs. Equation 58-60, which allow to extract the kinetic-energy/gradient-information differences from the corresponding energy profiles. Elsewhere[7,8] we have examined the BO energy profiles corresponding to the *bond*-formation process, A + B = AB (see Figure 1), and the bimolecular chemical-reaction, A + B $\rightarrow$ R^z $\rightarrow$ C + D (see Figure 2), where R^z denotes the Transition-State (TS) complex, in order to examine the accompanying changes in the resultant gradient information. Let us summarize some general conclusions of this analysis.

Figure 1 presents qualitative plots reflecting variations with internuclear distance of the ground-state *bond*-energy and its *kinetic*-energy contribution. The BO potential $\Delta E(R)$ and its *kinetic*-energy component $\Delta T(R)$ also reflecting variations in (resultant) gradient-information $\Delta I(R) = \sigma\Delta T(R)$, relative to SAL, allow one to examine the energy/information variations with *inter*-nuclear distance R in the bond formation process. It follows from the figure that during a mutual approach by the constituent atoms the kinetic-energy/gradient-information is first diminished relative to the SAL reference, due to the *longitudinal* Cartesian component of the kinetic energy, associated with the "z" direction (along the bond axis).[94,95] At the equilibrium distance R_e the resultant information rises above the SAL value, due to the dominating increase in *transverse* components of the kinetic energy, corresponding to "x" and "y" directions perpendicular to the bond axis. Therefore, at the equilibrium bond length R_e the chemical bond gives rise to a net *increase* in the resultant *gradient*-information relative to SAL, where electrons of each atom experience the external potential of only its own nucleus. This reflects a relatively more compact electron distribution in a molecule, where electrons move in the field of both nuclei.

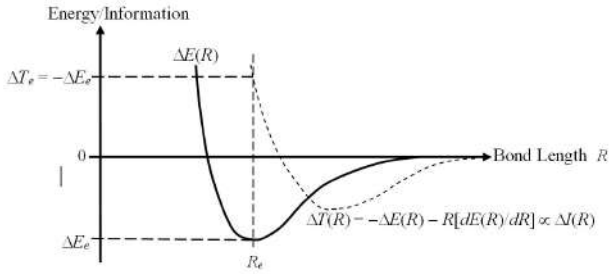

Figure 1. Qualitative diagram of variations in the BO electronic energy $\Delta E(R)$ (solid line) with the internuclear distance R in a diatomic molecule, and of its kinetic energy component from the virial-theorem partitioning, $\Delta T(R) = -d/dR[R\Delta E(R)]$ (broken line), also reflecting the state resultant *gradient*-information $\Delta I(R) = \sigma\Delta T(R)$

Another interesting case of variations in molecular geometry is the (intrinsic) reaction coordinate $\boldsymbol{R}_c$, or equivalently the *progress*-variable (*arc*-length) P along this trajectory, for which the virial relations assume the diatomic-like form (see Figure 2). Let us again examine the virial theorem decomposition of the corresponding energy profile along the $\boldsymbol{R}_c$-section of PES, $\Delta E(\boldsymbol{R}_c) \equiv \Delta E(P)$, in an elementary bimolecular reaction, to which the qualitative Hammond[81] postulate of reactivity theory applies. Again, the *ground*-state *virial*-theorem decomposition can be used to extract qualitative plots of the resultant *gradient*-information from the energy profiles corresponding either to *endo*- or *exo*-ergic reactions (upper panel), or to the energy-*neutral* chemical process on symmetric PES (lower panel).

The qualitative rule of Hammond is seen to be fully

indexed by the sign of the geometric, *P*-derivative of the average resultant-information at the TS complex.[5,8–10] More specifically, this postulate emphasizes a relative resemblance of the reaction TS complex $R^{\ddagger}$ to its substrates (products) in the *exo*-ergic (*endo*-ergic) reactions, while for the vanishing reaction energy the position of TS complex is predicted to be located symmetrically between substrates and products. In other words, the activation barrier appears "early" in the *exo*-ergic reactions, *e.g.*, $H_2 + F \rightarrow H + HF$, with the reaction substrates being only slightly modified in $R^{\ddagger} \approx [A - - - B]$, both electronically and geometrically. Accordingly, in the *endo*-ergic bond-breaking-bond-forming process, e.g., $H + HF \rightarrow H_2 + F$, the barrier is "late" along the reaction *progress*-variable *P* and the activated complex resembles more the reaction *products*: $R^{\ddagger} \approx [C - - - D]$. This qualitative statement has been subsequently given several more quantitative formulations and theoretical explanations, based upon both the energetic and entropic arguments[96–103].

The energy profile along the reaction "progress" coordinate *P*,

$$\Delta E\left(P\right) = E\left(P\right) - E\left(P_{substrates}\right) \tag{70}$$

is directly "translated" by the molecular virial theorem into the associated displacement in its kinetic-energy contribution,

$$\Delta T\left(P\right) \;\; = T\left(P\right) - T\left(P_{substrates}\right) \tag{71}$$

proportional to the corresponding change in the system resultant *gradient*-information:

$$\Delta I\left(P\right) \;\; = I\left(P\right) - I\left(P_{substrates}\right) \;\; = \sigma \Delta T\left(P\right) \tag{72}$$

$$\begin{aligned} \Delta T\left(P\right) \;\; &= -\Delta E\left(P\right) - P[d\Delta E\left(P\right)/dP] \\ &= -d[P\Delta E\left(P\right)]/dP \end{aligned} \tag{73}$$

The energy profiles $\Delta E(P)$ in the *endo*- or *exo*-directions, for the positive and negative reaction energy

$$\Delta E_r = E\left(P_{products}\right) - E\left(P_{substrates}\right) \tag{74}$$

respectively, thus determine uniquely the associated profiles of kinetic-energy (or resultant-information): $\Delta I(P) = \sigma \Delta T(P)$. A reference to qualitative plots in Figure 2 shows that the latter indeed distinguishes these two directions by the sign of its geometrical derivative at $R^{\ddagger}$:

$$\begin{aligned} &endo - direction: \\ &\{(dI/dP)_{\ddagger} > 0 \quad and \quad (dT/dP)_{\ddagger} > 0, \quad \Delta E_r > 0 \\ &energy - neutral: \\ &(dI/dP)_{\ddagger} = 0 \quad and \quad (dT/dP)_{\ddagger} = 0, \quad \Delta E_r = 0 \\ &exo - direction: \\ &(dI/dP)_{\ddagger} < 0 \quad and \quad (dT/dP)_{\ddagger} < 0, \quad \Delta E_r < 0 \end{aligned} \tag{75}$$

This demonstrates that the ground-state RC-derivative $dI/dP|_{\ddagger}$ of the resultant *gradient*-information at TS complex, proportional to $dT/dP|_{\ddagger}$, can serve as an alternative detector of the reaction energetic character: its positive/negative values identify the positive/negative reaction energy ΔE_r in *endo*/*exo*-ergic reactions, exhibiting the late/early activation barriers, respectively; the neutral case ($\Delta E_r = 0$ or $dT/dP|_{\ddagger} = 0$) exhibits an equidistant position of TS between the reaction substrates and products on a symmetrical potential energy surface, e.g., in the hydrogen exchange reaction $H + H_2 \rightarrow H_2 + H$.

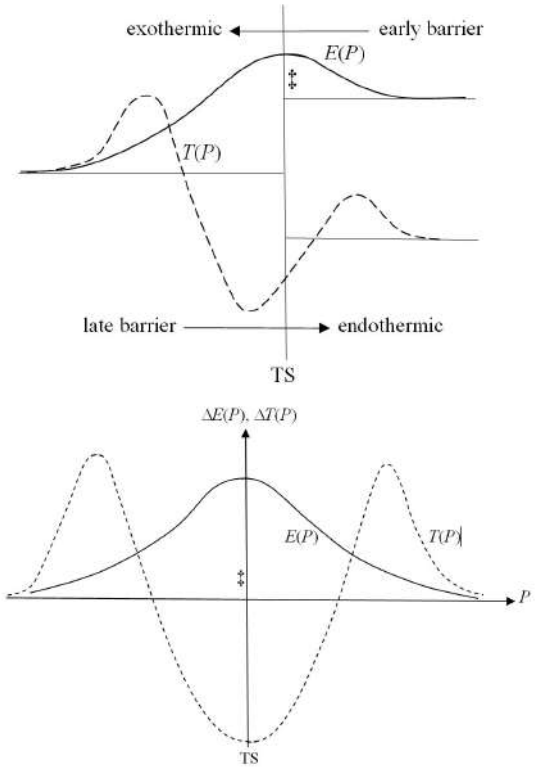

Figure 2. Variations of the BO total electronic energy (ΔE) and its kinetic energy component (ΔT) in the *exo*-ergic ($\Delta E_r < 0$) and *endo*-ergic ($\Delta E_r > 0$) reactions (upper Panel), and for the symmetrical PES ($\Delta E_r = 0$) (lower Panel)

Since the forces acting on nuclei in the equilibrium, separated reactants or products vanish, the reaction energy ΔE_r of Equation 74 determines the corresponding change in the resultant *gradient*-information,

$$\Delta I_r = I\left(P_{products}\right) - I\left(P_{substrates}\right) = \sigma \Delta T_r \tag{76}$$

proportional to the associated variation in the electronic

kinetic energy:

$$\Delta T_r = T\left(P_{products}\right) - T\left(P_{substrates}\right) \; = -\Delta E_r \tag{77}$$

The virial theorem thus implies a net *decrease* of the resultant *gradient*-information in *endo*-ergic processes, $\Delta I_r(endo) \propto$ -$\Delta E_r(endo) < 0$, its increase in *exo*-ergic reactions, $\Delta I_r(exo) \propto$ -$\Delta E_r(exo) > 0$, and a conservation of the overall *gradient*-information in the energy-*neutral* chemical rearrangements: $\Delta I_r(neutral) \propto$ -$\Delta E_r(neutral) = 0$.

One recalls that the classical part of this information displacement probes an average change in the spatial inhomogeneity of electron density. Therefore, the *endo*-ergic processes, requiring a net supply of energy to the reactive system R, give rise to relatively *less*-compact electron distributions in reaction products,comparedto substrates. Accordingly, the *exo*-ergic transitions, with a net release of energy from R, generate on average more concentrated electron distributions in products, and no such a change is predicted in energy-*neutral* case.

5 Conclusion

In this overview we have explored qualitative reactivity applications of the resultant information measure in QIT. First, the concept of the overall *gradient*-information in specified quantum state, which combines the classical (probability) and nonclassical (phase/current) contributions, has been introduced as the expectation value of the corresponding (Hermitian) *information*-operator related to that of electronic kinetic energy. We have then explored the *thermodynamic*-average measure and its variational principle in the *grand*-ensemble. The *electron*-population derivatives, information reactivity descriptors of CT phenomena in donor-acceptor systems, have been examined, the physical equivalence of variational principles for *ensemble*-averages of energy and information (*kinetic*-energy) in thermodynamics has been emphasized, and the relation between the *in situ* energy and information CT criteria have been examined.

The proportionality relation between the resultant *gradient*-information and kinetic energy of electrons indicates that the latter plays a more important role in chemical reactivity than previously thought. The electronic energy and information/kinetic-energyrepresent alternative descriptors of molecular equilibria. They generate physically equivalent and adequate reactivity criteria for describing CT phenomena in the acid-base systems. Since for representative *energy*-profiles this component is readily available from the molecular virial theorem, we have briefly examined the theorem general implications for changes in the overall information content of equilibrium molecular structures, the *bond*-formation process, and the Hammond postulate of reactivity theory. The principle of the maximum thermodynamic information has been formulated and the dependence in chemical processes of the change in the overall *gradient*-information upon the reaction energy has been addressed. The Hammond postulate has been shown to be quantitatively indexed by the geometrical information derivative at TS complex.

References

[1] Nalewajski RF. Quantum information theory of molecular states. Nova Science Publishers, New York, 2016.

[2] Nalewajski RF. Complex entropy and resultant information measures. J Math Chem, 2016, **54**: 1777-1782. https://dx.doi.org/10.1007/s10910-016-0651-6

[3] Nalewajski RF. On phase/current components of entropy/information descriptors of molecular states. Mol Phys, 2014, **112**: 2587-2601. https://dx.doi.org/10.1080/002689762014897394

[4] Nalewajski RF. Quantum information measures and their use in chemistry. Current Phys Chem, 2017, **7**: 94-117 https://dx.doi.org/10.2174/1877946806666160622075208

[5] Nalewajski RF. On entropy/information description of reactivity phenomena. In Advances in mathematics research vol 26, Baswell AR Ed). Nova Science Publishers, New York, in press, 2019.

[6] Nalewajski RF. Information description of chemical reactivity. Current Physical Chemistry, in press, 2019.

[7] Nalewajski RF. Role of electronic kinetic energy resultant gradient information) in chemical reactivity. J Mol Model Z. Latajka issue), submitted, 2019

[8] Nalewajski RF. Understanding electronic structure and chemical reactivity. In The Application of Quantum Mechanics in the Reactivity of Molecules, Sousa S Ed). Applied Sciences, submitted, 2019.

[9] Callen HB. Thermodynamics: an introduction to the physical theories of equilibrium thermostatics and irreversible thermodynamics. Wiley, New York, 1962.

[10] Nalewajski RF. Virial theorem implications for the minimum energy reaction paths. Chem Phys, 1980, **50**: 127-136. https://dx.doi.org/10.1016/0301-0104808087032-7

[11] Prigogine I. From being to becoming: time and complexity in the physical sciences. Freeman WH & Co, San Francisco, 1980.

[12] Hohenberg P and Kohn W. Inhomogeneous electron gas. Phys Rev, 1964, **136B**: 864-971. https://dx.doi.org/10.1103/PhysRev136B864

[13] Kohn W and Sham LJ. Self-consistent equations including exchange and correlation effects. Phys Rev, 1965, **140A**: 133-1138. https://dx.doi.org/10.1103/PhysRev140A1133

[14] Levy M. Universal variational functionals of electron densities, first-order density matrices, and natural spin-orbitals and solution of the v-representability problem. Proc Natl Acad Sci USA, 1979, **76**: 6062-6065. https://dx.doi.org/10.1073/pnas76126062

[15] Parr RG and Yang W. Density-functional theory of atoms and molecules. Oxford University Press, New York, 1989.

[16] Dreizler RM and Gross EKU. Density functional theory: an approach to the quantum many-body problem. Springer, Berlin, 1990. https://dx.doi.org/10.1007/978-3-642-86105-5

[17] Nalewajski, RF (ed). Density functional theory I-IV, Topics in Current Chemistry, 1996, vols(180-183). https://dx.doi.org/10.1007/3-540-61091-X https://dx.doi.org/10.1007/3-540-61131-2

[18] Nalewajski RF. Exploring molecular equilibria using quantum information measures. Ann Phys (Leipzig), 2013, **525**: 256-268. https://dx.doi.org/10.1002/andp201200230

[19] Nalewajski RF. On phase equilibria in molecules. J Math Chem, 2014, **52**: 588-612. https://dx.doi.org/10.1007/s10910-013-0280-2

[20] Nalewajski RF. Quantum information approach to electronic equilibria: molecular fragments and elements of non-equilibrium thermodynamic description. J Math Chem, 2014, **52**: 1921-1948. https://dx.doi.org/10.1007/s10910-014-0357-6

[21] Nalewajski RF. Phase/current information descriptors and equilibrium states in molecules. Int J Quantum Chem, 2015, **115**: 1274-1288 https://dx.doi.org/10.1002/qua24750

[22] Nalewajski RF. Quantum information measures and molecular phase equilibria. In Advances in mathematics research vol 19, Baswell AR Ed). Nova Science Publishers New York, **2015**: 53-86.

[23] Nalewajski RF. Phase description of reactive systems. In Conceptual density functional theory, Islam N, Kaya S eds). Apple Academic Press, Waretown, **2018**: 217- 249. https://dx.doi.org/10.1201/b22471-8

[24] Nalewajski RF. Entropy continuity, electron diffusion and fragment entanglement in equilibrium states. In Advances in mathematics research vol 22, Baswell AR ed). Nova Science Publishers, New York, **2017**: 1-42.

[25] Nalewajski RF. On entangled states of molecular fragments. Trends in Physical Chemistry, 2016, **16**: 71-85.

[26] Nalewajski RF. Chemical reactivity description in density-functional and information theories. In Chemical concepts from density functional theory, Liu S ed). Acta Physico-Chimica Sinica, 2017, **33**: 2491-2509.

[27] Nalewajski RF. Information equilibria, subsystem entanglement and dynamics of overall entropic descriptors of molecular electronic structure. J Mol Model (Chattaraj PK issue), 2018, **24**: 212-227. https://dx.doi.org/10.1007/s00894-018-3699-3

[28] Fisher RA. Theory of statistical estimation. Proc Cambridge Phil Soc, 1925, **22**: 700-725. https://dx.doi.org/10.1017/S0305004100009580

[29] Frieden BR. Physics from the Fisher information a unification. Cambridge University Press, Cambridge, 2004. https://dx.doi.org/10.1017/CBO9780511616907

[30] Shannon CE. The mathematical theory of communication. Bell System Tech J, 1948, **27**: 379-493. https://dx.doi.org/10.1002/j1538-73051948tb00917x

[31] Shannon CE, Weaver W. The mathematical theory of communication. University of Illinois, Urbana, 1949.

[32] Kullback S, Leibler RA. On information and sufficiency. Ann Math Stat, 1951, **22**: 79-86. https://dx.doi.org/10.1214/aoms/1177729694

[33] Kullback S. Information theory and statistics. Wiley, New York, 1959.

[34] Abramson N. Information theory and coding. McGraw-Hill, New York, 1963.

[35] Pfeifer PE. Concepts of probability theory. Dover, New York, 1978.

[36] Nalewajski RF. Information theory of molecular systems. Elsevier, Amsterdam, 2006.

[37] Nalewajski RF. Information origins of the chemical bond. Nova Science Publishers, New York, 2010.

[38] Nalewajski RF. Perspectives in electronic structure theory. Springer, Heidelberg, 2012. https://dx.doi.org/10.1007/978-3-642-20180-6

[39] Nalewajski RF and Parr RG. Information theory, atoms-in-molecules and molecular similarity. Proc Natl Acad Sci USA, 2000, **97**: 8879-8882. https://dx.doi.org/10.1073/pnas97168879

[40] Nalewajski RF. Information principles in the theory of electronic structure. Chem Phys Lett, 2003, **272**: 28-34. https://dx.doi.org/10.1016/S0009-26143300335-X

[41] Nalewajski RF. Information principles in the Loge Theory. Chem Phys Lett, 2003, **375**: 196-203. https://dx.doi.org/10.1016/S0009-26143300802-9

[42] Nalewajski RF and Broniatowska E. Information distance approach to Hammond Postulate. Chem Phys Lett, 2003, **376**: 33-39. https://dx.doi.org/10.1016/S0009-26143300915-1

[43] Nalewajski RF and Parr RG. Information-theoretic thermodynamics of molecules and their Hirshfeld fragments. J Phys Chem A, 2001, **105**: 7391-7400. https://dx.doi.org/10.1021/jp004414q

[44] Nalewajski RF. Hirschfeld analysis of molecular densities: subsystem probabilities and charge sensitivities. Phys Chem Chem Phys, 2002, **4**: 1710-1721. https://dx.doi.org/10.1039/b107158k

[45] Parr RG, Ayers PW and Nalewajski RF. What is an atom in a molecule? J Phys Chem A, 2005, **109**: 3957-3959. https://dx.doi.org/10.1021/jp0404596

[46] Nalewajski RF and Broniatowska E. Atoms-in-Molecules from the stockholder partition of molecular two-electron distribution. Theoret Chem Acc, 2007, **11**7: 7-27. https://dx.doi.org/10.1007/s00214-006-0078-4

[47] Heidar-Zadeh F, Ayers PW, Verstraelen T, *et al*. Information-theoretic approaches to Atoms-in-Molecules: Hirshfeld family of partitioning schemes. J Phys Chem A, 2018, **122**: 4219-4245. https://dx.doi.org/10.1021/acsjpca7b08966

[48] Hirshfeld FL. Bonded-atom fragments for describing molecular charge densities. Theoret Chim Acta (Berl), 1977, **44**: 129-138.
https://dx.doi.org/10.1007/BF00549096

[49] Nalewajski RF. Entropic measures of bond multiplicity from the information theory. J Phys Chem A, 2000, **104**: 11940-11951.
https://dx.doi.org/10.1021/jp001999f

[50] Nalewajski RF. Entropy descriptors of the chemical bond in Information Theory: I. Basic concepts and relations. Mol Phys 102:531-546; II. Application to simple orbital models. Mol Phys, 2004, **102**: 547-566.
https://dx.doi.org/10.1080/00268970410001675581

[51] Nalewajski RF. Entropic and difference bond multiplicities from the two-electron probabilities in orbital resolution. Chem Phys Lett, 2004, **386**: 265-271.
https://dx.doi.org/10.1016/jcplett2004164

[52] Nalewajski RF. Reduced communication channels of molecular fragments and their entropy/information bond indices, Theoret Chem Acc, 2005, **114**: 4-18.
https://dx.doi.org/10.1007/s00214-005-0638-z

[53] Nalewajski RF. Partial communication channels of molecular fragments and their entropy/information indices. Mol Phys, 2005, **103**: 451-470.
https://dx.doi.org/10.1080/00268970512331316030

[54] Nalewajski RF. Entropy/information descriptors of the chemical bond revisited. J Math Chem, 2011, **49**: 2308-2329.
https://dx.doi.org/10.1007/s10910-011-9888-2

[55] Nalewajski RF. Quantum information descriptors and communications in molecules. J Math Chem, 2014, **52**: 1292-1323.
https://dx.doi.org/10.1007/s10910-014-0311-7

[56] Nalewajski RF. Multiple, localized and delocalized/conjugated bonds in the orbital-communication theory of molecular systems. Adv Quant Chem, 2009, **56**: 217-250.
https://dx.doi.org/10.1016/S0065-32768800405-X

[57] Nalewajski RF, Szczepanik D and Mrozek J. Bond differentiation and orbital decoupling in the orbital communication theory of the chemical bond. Adv Quant Chem, 2011, **61**: 1-48.
https://dx.doi.org/10.1016/B978-0-12-386013-200001-2

[58] Nalewajski RF, Szczepanik D and Mrozek J. Basis set dependence of molecular information channels and their entropic bond descriptors. J Math Chem, 2012, **50**: 1437-1457.
https://dx.doi.org/10.1007/s10910-012-9982-0

[59] Nalewajski RF. Electron communications and chemical bonds. In Frontiers of quantum chemistry, Wjcik M, Nakatsuji H, Kirtman B, Ozaki Y eds). Springer, Singapore, **2017**: 315-351.

[60] Nalewajski RF, Świtka E and Michalak A. Information distance analysis of molecular electron densities. Int J Quantum Chem, 2002, **87**: 198-213.
https://dx.doi.org/10.1002/qua10100

[61] Nalewajski RF and Broniatowska E. Entropy displacement analysis of electron distributions in molecules and their Hirshfeld atoms. J Phys Chem A, 2003, **107**: 6270-6280.
https://dx.doi.org/10.1021/jp030208h

[62] Nalewajski RF. Use of Fisher information in quantum chemistry. Int J Quantum Chem (Jankowski K issue), 2008, **108**: 2230-2252.
https://dx.doi.org/10.1002/qua21752

[63] Nalewajski RF, Köster AM and Escalante S. Electron localization function as information measure. J Phys Chem A, 2005, **109**: 10038-10043.
https://dx.doi.org/10.1021/jp053184i

[64] Becke AD and Edgecombe KE. A simple measure of electron localization in atomic and molecular systems. J Chem Phys, 1990, **92**: 5397-5403.
https://dx.doi.org/10.1063/1458517

[65] Silvi B and Savin A. Classification of chemical bonds based on topological analysis of electron localization functions. Nature, 1994, **371**:683-686.
https://dx.doi.org/10.1038/371683a0

[66] Savin A, Nesper R, Wengert S, *et al*. ELF: the electron localization function. Angew Chem Int Ed Engl, 1997, **36**: 1808-1832.
https://dx.doi.org/10.1002/anie199718081

[67] Nalewajski RF, de Silva P and Mrozek J. Use of nonadditive Fisher information in probing the chemical bonds. J Mol Struct: THEOCHEM, 2010, **954**: 57-74.
https://dx.doi.org/10.1016/jtheochem2010128

[68] Nalewajski RF. Through-space and through-bridge components of chemical bonds. J Math Chem, 2011, **49**: 371-392.
https://dx.doi.org/10.1007/s10910-010-9747-6

[69] Nalewajski RF. Chemical bonds from through-bridge orbital communications in prototype molecular systems. J Math Chem, 2011, **49**: 546-561
https://dx.doi.org/10.1007/s10910-010-9761-8

[70] Nalewajski RF. On interference of orbital communications in molecular systems. J Math Chem, 2011, **49**: 806-815.
https://dx.doi.org/10.1007/s10910-010-9777-0

[71] Nalewajski RF and Gurdek P. On the implicit bond-dependency origins of bridge interactions. J Math Chem, 2011, **49**: 1226-1237.
https://dx.doi.org/10.1007/s10910-011-9815-6

[72] Nalewajski RF. Direct through-space) and indirect through-bridge) components of molecular bond multiplicities. Int J Quantum Chem, 2012, **112**: 2355-2370.
https://dx.doi.org/10.1002/qua23217

[73] Nalewajski RF and Gurdek P. Bond-order and entropic probes of the chemical bonds. Struct Chem, 2012, **23**: 1383-1398.
https://dx.doi.org/10.1007/s11224-012-0060-9

[74] Nalewajski RF, Korchowiec J and Michalak A. Reactivity criteria in charge sensitivity analysis. Topics in Current Chemistry: Density functional theory IV, Nalewajski RF (ed), 1996, **183**: 25-141.
https://dx.doi.org/10.1007/3-540-61131-2_2

[75] Nalewajski RF and Korchowiec J. Charge sensitivity approach to electronic structure and chemical reactivity. World Scientific, Singapore, 1997.
https://dx.doi.org/10.1142/2735

[76] Geerlings P, De Proft F and Langenaeker W. Conceptual density functional theory. Chem Rev, 2003, **103**: 1793-1873.
https://dx.doi.org/10.1021/cr990029p

[77] Nalewajski RF. Sensitivity analysis of charge transfer systems: in situ quantities, intersecting state model and its implications. Int J Quantum Chem, 1994, **49**: 675-703.
https://dx.doi.org/10.1002/qua560490512

[78] Nalewajski RF. Charge sensitivity analysis as diagnostic tool for predicting trends in chemical reactivity. In Proceedings of the NATO ASI on Density Functional Theory Il Ciocco, 1993), Dreizler RM, Gross EKU eds). Plenum, New York, **1995**: 339-389.
https://dx.doi.org/10.1007/978-1-4757-9975-0_15

[79] Chattaraj PK (ed). Chemical reactivity theory: a density functional view. CRC Press, Boca Raton, 2009.
https://dx.doi.org/10.1201/9781420065442

[80] Gatti C and Macchi P. Modern charge-density analysis. Springer, Berlin, 2012.
https://dx.doi.org/10.1007/978-90-481-3836-4

[81] Hammond GS. A correlation of reaction rates. J Am Chem Soc, 1955, **77**: 334-338.
https://dx.doi.org/10.1021/ja01607a027

[82] von Weizscker CF. Zur theorie der kernmassen. Z Phys, 1935, **96**: 431-458.
https://dx.doi.org/10.1007/BF01337700

[83] Nalewajski RF. Density matrix in determining electron communications and resultant information content in molecular states. In Understanding Density Matrices. Nova Science Publishers, New York, submitted, 2019.

[84] Harriman JE. Orthonormal orbitals fort the representation of an arbitrary density. Phys Rev A, 1980, **24**: 680-682.
https://dx.doi.org/10.1103/PhysRevA24680

[85] Zumbach G and Maschke K. New approach to the calculation of density functionals. Phys Rev A, 1983, **28**: 544-554.
https://dx.doi.org/10.1103/PhysRevA28544

[86] Gyftopoulos EP and Hatsopoulos GN. Quantum-thermodynamic definition of electronegativity. Proc Natl Acad Sci USA, 1965, **60**: 786-793.
https://dx.doi.org/10.1073/pnas603786

[87] Perdew JP, Parr RG, Levy M, *et al*. Density functional theory for fractional particle number: derivative discontinuities of the energy. Phys Rev Lett, 1982, **49**:1691-1694.
https://dx.doi.org/10.1103/PhysRevLett491691

[88] Mulliken RS. A new electronegativity scale: together with data on valence states and on ionization potentials and electron affinities. J Chem Phys, 1934, **2**: 782-793.
https://dx.doi.org/10.1063/11749394

[89] Iczkowski RP and Margrave JL. Electronegativity. J Am Chem Soc, 1961, **83**: 3547-3551.
https://dx.doi.org/10.1021/ja01478a001

[90] Parr RG, Donnelly RA, Levy M, *et al*. Electronegativity: the density functional viewpoint. J Chem Phys, 1978, **69**: 4431-4439.
https://dx.doi.org/10.1063/1436185

[91] Parr RG and Pearson RG. Absolute hardness: companion parameter to absolute electronegativity. J Am Chem Soc, 1983, **105**: 7512-7516.
https://dx.doi.org/10.1021/ja00364a005

[92] Parr RG and Yang W. Density functional approach to the frontier-electron theory of chemical reactivity. J Am Chem Soc, 1984, **106**: 4049-4050.
https://dx.doi.org/10.1021/ja00326a036

[93] Von Neumann J. Mathematical foundations of quantum mechanics. Princeton University Press, Princeton, 1955.

[94] Feinberg MJ and Ruedenberg K. Paradoxical role of the kinetic-energy operator in the formation of the covalent bond. J Chem Phys, 1971, **54**: 1495-1512.
https://dx.doi.org/10.1063/11675044

[95] Feinberg MJ and Ruedenberg K. Heteropolar one-electron bond. J Chem Phys, 1971, **55**: 5805-5818.
https://dx.doi.org/10.1063/11675751

[96] Marcus RA. Theoretical relations among rate constants, barriers, and Broensted slopes of chemical reactions. J Phys Chem, 1968, **72**: 891-899.
https://dx.doi.org/10.1021/j100849a019

[97] Agmon N and Levine RD. Energy, entropy and the reaction coordinate: thermodynamic-like relations in chemical kinetics. Chem Phys Lett, 1977, **52**: 197-201.
https://dx.doi.org/10.1016/0009-2614777780523-X

[98] Agmon N and Levine RD. Empirical triatomic potential energy surfaces defined over orthogonal bond-order coordinates. J Chem Phys, 1979, **71**: 3034-3041.
https://dx.doi.org/10.1063/1438709

[99] Miller AR. A theoretical relation for the position of the energy barrier between initial and final states of chemical reactions J Am Chem Soc, 1978, **100**: 1984-1992.
https://dx.doi.org/10.1021/ja00475a002

[100] Ciosowski J. Quantifying the Hammond Postulate: intramolecular proton transfer in substituted hydrogen catecholate anions. J Am Chem Soc, 1991, **113**: 6756-6761.
https://dx.doi.org/10.1021/ja00018a006

[101] Nalewajski RF, Formosinho SJ, Varandas AJC, *et al*. Quantum mechanical valence study of a bond breaking bond forming process in triatomic systems. Int J Quantum Chem, 1994, **52**: 1153-1176.
https://dx.doi.org/10.1002/qua560520504

[102] Nalewajski RF and Broniatowska E. Information distance approach to Hammond postulate. Chem Phys Lett, 2003, **376**: 33-39.
https://dx.doi.org/10.1016/S0009-26143300915-1

[103] Dunning TH Jr. Theoretical studies of the energetics of the abstraction and exchange reactions in H + HX, with X = F-I. J Phys Chem, 1984, **88**: 2469-2477.
https://dx.doi.org/10.1021/j150656a011

Chem Rep, 2019, 1(1): 36-42
DOI: 10.25082/CR.2019.01.004

RESEARCH ARTICLE

In vivo study of gold-nanoparticles using different extracts for kidney, liver function and photocatalytic application

Muhammad Isa Khan[1*] Seemab Dildar[1,4] Tahir Iqbal[1] Muhammad Shakil[1]
Muhammad Bilal Tahir[1] Muhammad Rafique[1] Farooq Aziz[2] Sardar Bibi[3] Mohsin Ijaz[1*]

Abstract: We report novel gold nanoparticles by green method for different fruit extracts have gaining greater attention due to its versatile properties in different applications. In this article, GNPs synthesis is demonstrated successfully using fresh fruit extract of *punica granatum* and *fragaria*. The optical properties, morphology and elemental analysis of samples was done by using) different characterization techniques like SEM EDX and UV-Visible spectroscopy Biocompatibility of GNPs was determined by ALT, AST, ALP, Urea, Creatinine tests and also to investigate the effects of prepared GNPs on the kidney and liver functions. The GNPs prepared by fruit extract of punica granatum have more effects on the rabbits than GNPs prepared from fragaria but this effect normalizes after three days which shows its biocompatibility. To explore the photocatalytic activity of the GNPs the photocatalytic degradation of MB dye is also investigated. The results revealed that GNPs prepared through green synthesis route are found to be efficient enhancement in the degradation of MB dye in visible region due to large surface area. These particles were more active in catalytic reduction due to their high surface energy and in bio-medical applications as biocompatibility.

Keywords: green method, AuNPs, biocompatibility, photocatalytic activity

1 Introduction

Nanoparticles act as a bridge between bulk materials and atomic or molecular structures as they have variety of scientific interest. Now a days, evolution in material sciences are experiencing broad field work by interacting with different scientific disciplines and making strong effect on every fields of life.[1] The Au NPs have discovered their tracks in the disciplines of life sciences or biological sciences in view of their biocompatibility and reaction given by the human body it is because of golds non-poisonous nature and inert core. The color of gold nanoparticles is red because of its property of the surface Plasmon resonance (SPR).[2,3] Gold nanoparticles have high absorption cross sectional area, High solubility, Productive SPR has simple linkage with targeting particles and drug due to its peaks at longer wavelength. These characteristics make GNPs a promising member for cancer thermal treatment and different pathogenic sicknesses.[4] A gold nanoparticle as a result of its optical, physical (Quantifiable) and chemical importance was considerably more useable in the area of life sciences. The inert character of the Au NPs is additionally valuable for the determination of cancer cells, impetuses, utilized in the drug delivery and so forth.[5] Au NPs has extensive vivo biomedical applications (BME) particularly as a malignant cell growth , imaging as well as in treatment.[6] The Au NPs effectively works with targeting biomolecules via thiol-gold conjugation method.[7,8] Gold nanoparticles are used to design conductors from printable inks which print on the electronic chips as used in computers to make their speed fast.[9] In medical, the gold nanoparticles can be used for the diagnosis of heart diseases, infection, tumor and cancers; to detect biomarkers.[10] There reported many strategies for the preparation of Au NPs like reduction method,[11] sol-gel technique,[12] micro emulsion approach,[13] hydrothermal technique,[14] green approach,[15] and so on and numerous different strategies utilized op-down approach resemble sono-chemical

Received: March 22, 2019 **Accepted:** April 8, 2019 **Published:** April 12, 2019

[*] **Correspondence to**: Muhammad Isa Khan, Department of Physics, Faculty of Science, University of Gujrat, Hafiz Hayat Campus, Gujrat, 50700, Pakistan; Email: isaiub@yahoo.com; Mohsin Ijaz, Department of Physics, Faculty of Science, University of Gujrat, Hafiz Hayat Campus, Gujrat, 50700, Pakistan; Email: mohsin@live.no

[1] Department of Physics, Faculty of Science, University of Gujrat, Hafiz Hayat Campus, Gujrat, 50700, Pakistan.

[2] Department of Physics, The Islamia University of Bahawalpur, Bahawalpur, Pakistan.

[3] Department of biotechnology, Virtual University, Pakistan.

[4] University of the Punjab, Physics Lahore, Pakistan.

Citation: Khan MI, Dildar S, Iqbal D, *et al*. *In vivo* study of gold-nanoparticles using different extracts for kidney, liver function and photocatalytic application. *Chem Rep*, 2019, **1**(1): 36-42.

technique, vapor deposition by chemicals, electros pinning, electrophoretic deposition, heating stirring method ,micro-emulsion method, laser ablation, and mechanical milling, *etc*. The green synthesis is another viable technique for the preparation of gold nanoparticles. Malva crispa (mallow) utilized for the amalgamation of Au NPs along with strong antibacterial or antimicrobial agent against a bacterium, virus, or other microorganism and sustenance decay.[16] The Au NPs in range 20-30 nm are reported to be extracted by using aqueous leaves of Acalypha indica.[17] Triangular shaped gold nanoparticles were also prevail through Au ions reduction by the fluid of lemongrass.[18] A reducing and capping agent such as *Cymbopogon citratus* leaf extract is also reported for the synthesis of gold nanoparticles.[19] Biosynthesis of *Zingiber officinale* leaf extract to form 10 nm gold nanoparticle size is also reported earlier.[20] The synthesized nanoparticleshas great capacity to produce the drugs and used against fungal diseases.[21] A solid gold nanoparticle with changing size variable size was procure obtained by with using the extract of the *endophytic fungus* leave synthesis.[22] The *Punica granatum* juice used for the preparation of AuNPs for the application in a cancer targeted drug delivery.[23–25] Quercetin was packed within disulfide-modified mesoporous silica together with GNPs (Q-Au/SiO2) which had voids around GNPs and final materials can refine its packing and efficiency in drug carier.[26] The thermoresponsive hyperbranched polymer functionalized with GNPs synthesize through in-situ chemical reduction method is reported earlier in which, the green preparation method is used with further applications in unusual colorimetric sensor along with energy saving, environmental protection, and sustainable development features.[27] A basic in-situ preparation method was developed to manufacture, complex of Tremella fuciformis (TF) and gold nanoparticles (AuNPs). The intensities of the localized surface plasmon resonance (LSPR) of the complex of TF and GNPs increased due to drying.[28] In Previous research work an substitute method used for making extremely stable GNPs, where an inert Curcuma mangga (CM) which act as stabilizing and reducing agent juice, was used to overcome the previously mentioned requirements. Blood tests were taken which divulge that prepared GNPs with less than 10% of hemolysis without any accumulation of erythrocytes were blood-compatible. The further research reveals that for the preparation of GNPs ,there is great possibilities by involving a CM-extract-based method for anticancer diagnosis and therapy.[29] From literature, Au NPs synthesized from *Punica granatum* was used as a cancer targeted drug delivery. In this study, we reported the same green method from *Punica granatum* with varying ratios. This work additionally reports the green synthesis of AuNPs at ambient temperature nearly equal to 20°C by utilizing natural product concentrate of Fragaria (strawberry) as reducing gent which is another option in writing. The previous results of GNPs from *Punica granatum* has been compared with synthesis of GNPs via using *Fragaria* (strawberry). Previous studies on biomedical applications resulted that GNPs insert into animal bodies get gather together or acquire an increasing number in the liver and kidneys, which could be dangerous. This work includes the animal studies through which GNPs biocompatibility was confirmed so this research work was further helpful for humans due to its biocompatibility.

2 Materials and Methods

The 250 g and 100 g edible grains of *Punica granatum* and *Fragaria* (Strawberry) were clean twice with normal tap water than once with DDW, then cut into small cubes in a blade bleender with 50 mL of DDW until a uniform mixture formed. The prepared solution of *Punica granatum* was centrifuged in order to wash the sample for 2 minutes, with next step of filtering through whatsman filter paper and stored at -18°C for further utilization. Precursor solution was prepared by using 30 wt% Chloroauric acids (HAuCl4) in 50 mL of DDW to form a 0.1 g/L solution. 0.75 mL of fruit extract of *Punica granatum* and *Fragaria* (Strawberry) was added in prepared precursor solution in order to synthesized gold nanoparticles. It was perceive that the color of solution transform into deep purple/red within few seconds under constant stirring at room temperature while slight heating (35°C-40°C) for several minutes were compulsory respectively. The color transformation as shown in figure 1 was due to presence of AuNP, as clarified through UV-vis absorption at 530 nm and 528 nm. (see Figure 1).

Figure 1. Preparation of GNPs (Color changes after 15mins to 30mins)

3 Results and Discussion

3.1 SEM analysis

The SEM examination was follow out with Hitachi S-4500 SEM. For imaging, carbon-coated grid utilize for thin film preparation of samples, coated with carbon were taken in a small amount needed on the grid and extra solution is remove by using paper. Then the film was dried by putting SEM grid under mercury lamp for five minutes and the picture was made. The GNPs has spherical like shape with an average diameter ranging from 25-35 nm as clearly shown in Figure 2(A), which were synthesized at room temperature *using Punica granatum* fruit extract. The SEM images in Figure 2(B) clearly indicates aggregation formation of spherical like GNPs with an average diameter ranging from 30-45nm as prepared by using *Fragaria*. The SEM images clearly illustrate that, prepared GNPs from fruit extract of *Fragaria* are more stabilized than *Punica granatum* due to containing rich primary and secondary metabolisms.

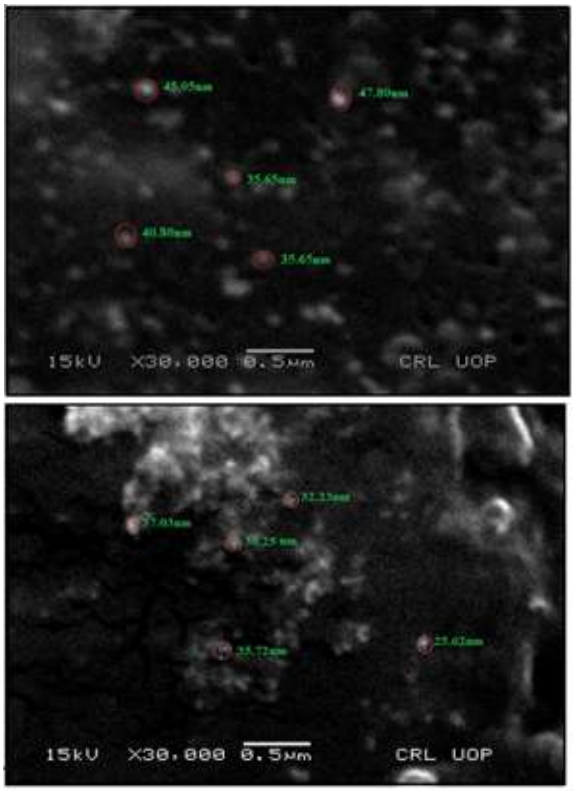

Figure 2. (A) SEM images for the GNPs from *Punica granatum*; (B) SEM images for the GNPs from *Fragaria*

3.2 EDX analysis

The EDX spectroscopy has carried out in order to identify elemental percentage in the GNPs samples. It depends upon the atomic mass of the element which is to be detected. So, if samples have mixed elements with wide range of atomic numbers then detector peals size will not vary with the compositional ratios. The EDX spectra of prepared GNPs using *Punica granatum* and *Fragaria* are appeared in Figure 3(A) and Figure 3(B), respectively. The EDX profile indicated highest signal for GNPs at KeV with some other adjoint elements such as Mg, K and Ca. The organic compounds (carbon and oxygen) are absorbed on the surface of GNPs from fruit extract of *Punica granatum* and *Fragaria,* which plays a great role in the reduction and capping of GNPs. The EDX spectra illustrate that, *Fragaria* have rich capping and reducing capability than *Punica granatum.*

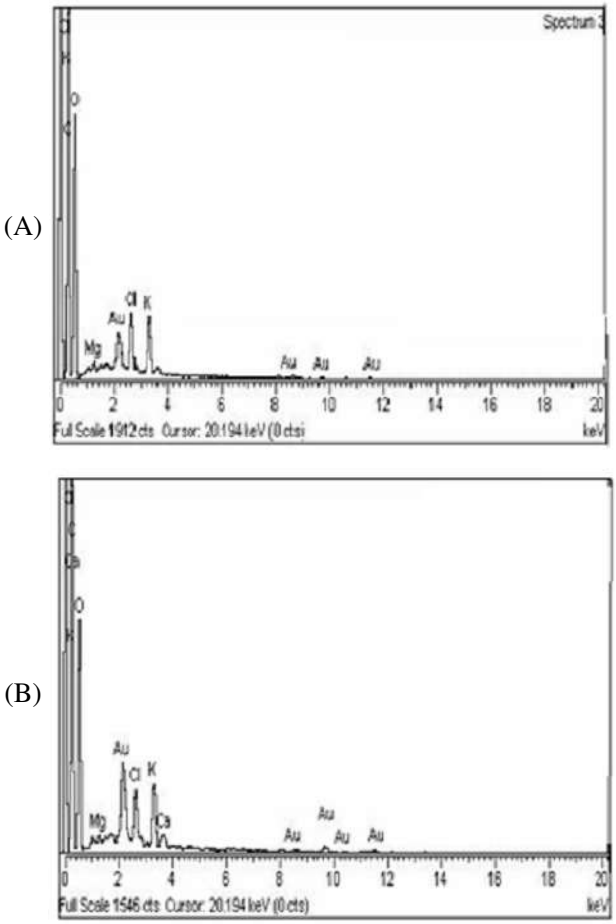

Figure 3. EDX profile of gold nanoparticles prepared from (A) *Punica granatum* (B) *Fragaria*

3.3 UV-Visible spectroscopy analysis

The optical properties and formation of GNPs were explored by using UV-Visible spectroscopy. The UV-Visible spectra for GNPs prepared by using fruit extract of *Punica granatum* and *Fragaria* respectively are shown in Figure 4(A) and Figure 4(B). The maximum

absorption peaks are observed at 528nm and 530 nm, respectively. These peaks clearly indicate thatthe prepared GNPs exhibits surface plasmon resonance phenomena at 528 nm and 530nm. It is worth mentioning that the absorption peak of GNPs prepared by using *Fragaria* are broad than prepared by using *Punica granatum.*

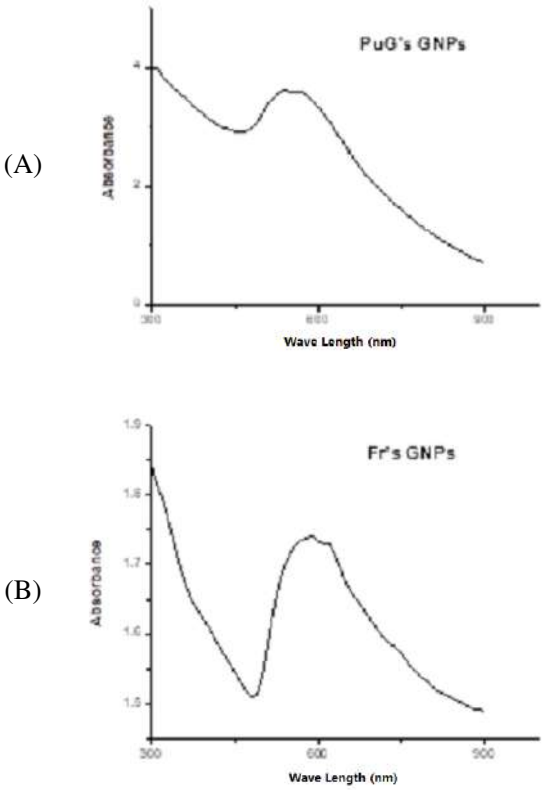

Figure 4. (A) shown UV-Visible spectra of GNPs prepared by using fruit extract of *Punica granatum* at 528nm (B) indicates UV-Visible spectra of GNPs by using fruit extract of *Fragaria*

3.3.1 Animal studies

As indicated by the guidelines and methodology set by the University of Veterinary and Animal Sciences, Lahore (UVAS), the animal care was carried out. Two healthy albino rabbits were chosen. GNPs prepared by *Punica granatum* administrated by one of the rabbits and second one rabbit with GNPs prepared by Fragaria. For this 0.8 mg of gold nanoparticles were scattered in 0.8 ml saline buffer solution. So two injections were prepared, first GNPs prepared from *Punica granatum* sample and second from Fragaria sample These injections were injected in male rabbits through marginal ear vein.

After the two and three days of injection, the blood tests were taken and were broke down for biochemical blood parameters (glucose and cholesterol levels), renal function (blood urea and serum Creatinine, liver function Alanine Transferase [ALT] Alkaline phosphatase [ALP] and aspartate aminotransferase [AST]).(See Figure 5)

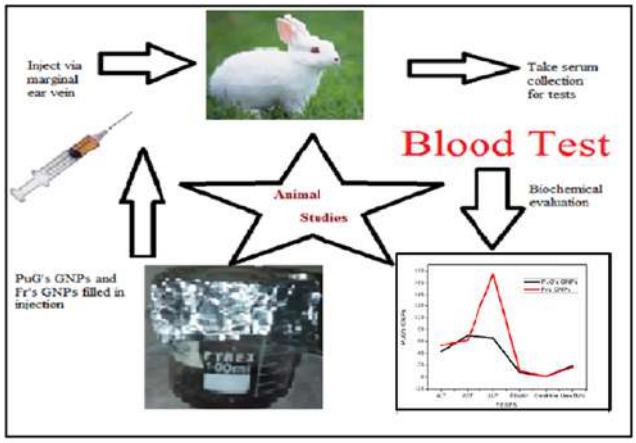

Figure 5. Process for animal studies in albino rabbits. PuG's GNPs means gold nanoparticles prepared from *Punica granatum* and Fr's GNPs from *Fragaria*

Priorly theexaminations about nanoparticles have demonstrated the AuNPs insert in the bodies of animals accumulated within liver and kidneys that would be lethal and results in the demise of animals. This work reported the biocompatibility of GNPs and its consequence on liver and kidney function have been studied in albino rabbits. All rabbits remain alive during the 3-day study period after injection, and no progressions were seen in typical conduct, for example, nourishment utilization and physical capacity.

After injecting prepared gold nanoparticles has shown a slight increase in ALT levels and AST level as in (Figure 6 (A,B)) which decreases slightly after the first Day injection in AST and on the other hand ALT decreases and went normal on third day after injection. For the next 3 days after injection, the statistic information was composed. ALT level at first 2 days tend to get normalize on 3rd day and have no fetal effects and liver destruction. AST and ALP found in the liver and other tissues is look over regularly according to the liver along ALT and bilirubin.

ALP level (Figure 7C) increases on first day and decreases on second and third day. Total bilirubin (Figure 7D) directly decreases after the first day injection then remains same on the second day. The level of total bilirubin endure constant for 2 days than expanded somewhat on the third day in the injected rabbit Fr. GNP. Here, bilirubin is a component of red blood cells, including the liver and ALT is an enzyme that is present just in living.

Renal function is evaluated by blood urea (Figure 8E) and creatinine (Figure 8F) by the kidneys. Our outcomes demonstrated a little bit decreasing of creatinine level

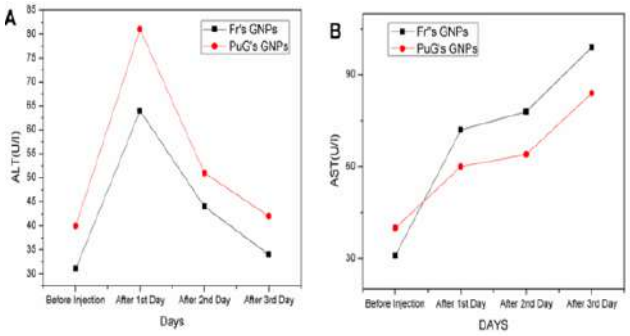

Figure 6. Effect of GNPs on ALT and AST level

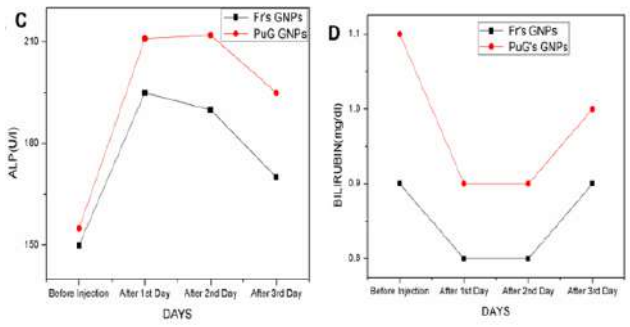

Figure 7. Effects of GNPs on ALP and Bilirubin level

(Figure 8F) following third days of Fragaria GNPsBy result of liver and kidney function, it is noteworthy that the renal function is more influenced by the GNPs of Punica granatum compared to the GNPs of Fragaria. However, in this work, it is obviously seen that both liver and kidney functions are influenced possibly after the two sorts of gold nanoparticles as reported.[30] The present study showed that contrast efficiency of both GNPs from Punica granatum and GNPs from fragaria is in agreement with previous studies.[31–33]

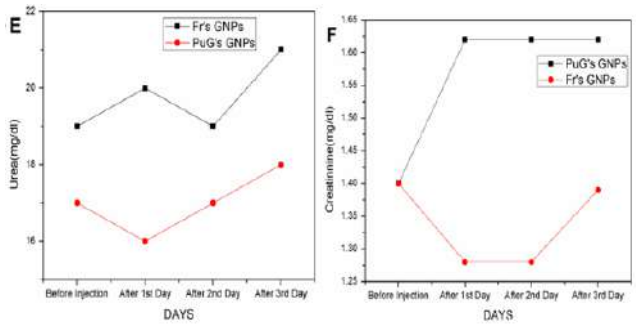

Figure 8. Effects of GNPs on Urea level and Creatinine level

3.4 Photocatalytic Degradation

Zeolite mixtures with gold nanoparticles (AuNPs/zeolite) have been synthesize prior by advancement of zeolite from coal fly fiery remains, strong waste poison, and its transformation to visible light active photoocatalyst via immobilization of GNPs by both in situ and ex situ methods.[34] The 5ppm aqueous solution of methylene blue dye was prepared at room temperature with prepared GNPs (1 g/L) as photocatalyst. It indicates the degradation of MB dye molecules with GNPs photocatalyst was analyzed as function of time. It is observed that, degradation rate was drastically increased with increasing time as well as maximum dye was degraded in 150 mintues of reaction time due to rich availability of active sites (Figure 9). The smaller particles exhibits maximum photo catalytic activity because of increasing surface to volume ratio with maximum number of active sites.

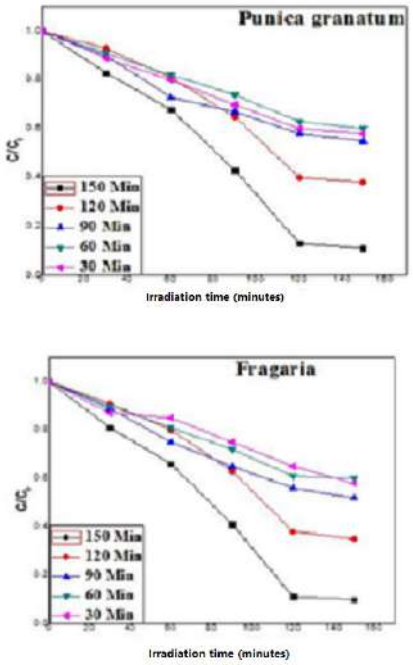

Figure 9. Degradation rate for the activity measurement with GNPs (1 g/L) photocatalyst using different extracts

4 Conclusion

The green synthesis technique is financially savvy, ecofriendly and can create GNPs at room temperature. *Punica granatum* and *Fragaria* fruit extracts have been used for the development of GNPs with spherical shapes. The average size of GNPs crystal by *Punica granatum* was found to be between 25 nm and 35 nm and that for GNPs prepared from Fragaria was of the order of 30 nm to 45 nm. This examination demonstrates the impacts of prepared AuNPs tests on liver and kidney capacities when rabbits were injected intravenously with

0.80 mg/kg body weight per dose of GNPs prepared by *Punica granatum* and *Fragaria* respectively. The impacts of gold nanoparticles on the biochemical parameters were assessed following 1, 2 and 3 days of intravenous (IV) injections, including the profile of liver function and renal (kidney) work. The final products indicates GNPs prepared by *Punica granatum* have more impact on the rabbits as contrast with Fragaria as there was some increase in the level of aspartate amino transferees (AST), antacid phosphate (ALP), and Serum creatinine however that impact normalize following days which demonstrates their biocompatibility. It was observed that the photocatalytic activity of the GNPs could be affected by increasing the number of active sites due to larger surface to volume ratio.

5 Conflict of interest

It is declared that the authors have no conflict of interest.

References

[1] De Jon WH and Borm PJ. Drug delivery and nanoparticles: applications and hazards. International Journal of Nanomedicine, 2008, **3**(2): 133. https://doi.org/10.2147/IJN.S596

[2] Fernandez-Fernandez A, Manchanda R and McGoron AJ. Theranostic applications of nanomaterials in cancer, drug delivery, image-guided therapy, and multifunctional platforms. Applied Biochemistry and Biotechnology Journal, 2011, **165**(7-8): 1628-1651. https://doi.org/10.1007/s12010-011-9383-z

[3] Levy R, Shaheen U, Cesbron Y, *et al*. Gold nanoparticles delivery in mammalian live cells: a critical review. Nano reviews, 2010, **1**(1): 4889.

[4] Welch A. The thermal response of laser irradiated tissue. IEEE Journal of Quantum Electronics, 1984, **20**(12): 1471-1481. https://doi.org/10.1109/JQE.1984.1072339

[5] Jacques SL and Prahl SA. Modeling optical and thermal distributions in tissue during laser irradiation. Lasers in Surgery and Medicine, 1987, **6**(6): 494-503. https://doi.org/10.1002/lsm.1900060604

[6] Merchant B. Gold, the noble metal and the paradoxes of its toxicology. Biologicals Journals, 1998, **26**(1): 49-59. https://doi.org/10.1006/biol.1997.0123

[7] Keren S, Zavaleta C, Cheng Z, *et al*. Noninvasive molecular imaging of small living subjects using Raman spectroscopy. Proceedings of the National Academy of Sciences, 2008, **105**(15): 5844-5849. https://doi.org/10.1073/pnas.0710575105

[8] Qian X, Peng XH, Ansari DO, *et al*. In vivo tumor targeting and spectroscopic detection with surface-enhanced Raman nanoparticle tags. Nature Biotechnology, 2008, **26**(1): 83. https://doi.org/10.1038/nbt1377

[9] Huang D, Liao F, Molesa S, *et al*. Plastic-compatible low resistance printable gold nanoparticle conductors for flexible electronics. Journal of the Electrochemical Society, 2003, **150**(7): 412-417. https://doi.org/10.1149/1.1582466

[10] Peng G, Tisch U, Adams O, *et al*. Diagnosing lung cancer in exhaled breath using gold nanoparticles. Nature Nanotechnology, 2009, **4**(10): 669-673. https://doi.org/10.1038/nnano.2009.235

[11] Johan MR, Chong LC and Hamizi NA. Preparation and stabilization of monodisperse colloidal gold by reduction with monosodium glutamate and poly (methyl methacrylate). International. Journal of Electrochem Sci, 2012, **7**: 4567-4573.

[12] Choi YJ, Chiu CK and Luo TJM. Spontaneous deposition of gold nanoparticle nanocomposite on polymer surfaces through solgel chemistry. Nanotechnology, 2010, **22**(4): 045601. https://doi.org/10.1088/0957-4484/22/4/045601

[13] Lisiecki I and Pileni MP. Synthesis of copper metallic clusters using reverse micelles as microreactors. Journal of the American Chemical Society, 1993, **115**(10): 3887-3896. https://doi.org/10.1021/ja00063a006

[14] Yan W, Chen B, Mahurin SM, *et al*. Preparation and comparison of supported gold nanocatalysts on anatase, brookite, rutile, and P25 polymorphs of TiO2 for catalytic oxidation of CO. The Journal of Physical Chemistry B, 2005, **109**(21): 10676-10685. https://doi.org/10.1021/jp044091o

[15] Gupta N, Singh HP and Sharma RK. Single-pot synthesis: plant mediated gold nanoparticles catalyzed reduction of methylene blue. Journal of Physicochemical and Engineering Aspects, 2010, **367**(1): 102-107. https://doi.org/10.1016/j.colsurfa.2010.06.022

[16] Chandran K, Song S and Yun SI. Effect of size and shape controlled biogenic synthesis of gold nanoparticles and their mode of interactions against food borne bacterial pathogens. Arabian Journal of Chemistry, 2014: S1878535214003189. https://doi.org/10.1016/j.arabjc.2014.11.041

[17] Acalypha indica Linn: Biogenic synthesis of silver and gold nanoparticles and their cytotoxic effects against MDA-MB-231, human breast cancer cells. Biotechnology Reports, 2014, **4**: 42-49. https://doi.org/10.1016/j.btre.2014.08.002

[18] Rai A , Chaudhary M , Ahmad A , *et al*. Synthesis of triangular Au coreAg shell nanoparticles. Materials Research Bulletin, 2007, **42**(7): 1212-1220. https://doi.org/10.1016/j.materresbull.2006.10.019

[19] Murugan K, Benelli G, Panneerselvam C, *et al*. Cymbopogon citratus-synthesized gold nanoparticles boost the predation efficiency of copepod Mesocyclops aspericomis against malaria and dengue mosquitoes. Experimental Parasitology, 2015, **153**: 129-138. https://doi.org/10.1016/j.exppara.2015.03.017

[20] Singh C, Sharma V, Naik PKR, *et al*. A green biogenic approach for synthesis of gold and silver nanoparticles using Zingiber officinale. Digest Journal of Nanomaterials and Biostructures, 2011, **6**(2): 535-542.

[21] Jayaseelan C, Ramkumar R, Rahuman AA, *et al*. Green synthesis of gold nanoparticles using seed aqueous extract of Abelmoschus esculentus and its antifungal activity. Industrial Crops and Products, 2013, **45**(45): 423-429.

[22] Shankar SS, Ahmad A, Pasricha R, *et al*. Bioreduction of chloroaurate ions by geranium leaves and its endophytic fungus yields gold nanoparticles of different shapes. Journal of Materials Chemistry, 2003, **13**(7): 1822. https://doi.org/10.1039/b303808b

[23] Ganeshkumar, Moorthy, Ponrasu, *et al*. Spontaneous ultra fast synthesis of gold nanoparticles using Punica;granatum for cancer targeted drug delivery. Colloids Surf B Biointerfaces, 2013, **106**(3): 208-216. https://doi.org/10.1016/j.colsurfb.2013.01.035

[24] Glazer ES, Zhu C, Hamir AN, *et al*. Biodistribution and acute toxicity of naked gold nanoparticles in a rabbit hepatic tumor model. Nanotoxicology Journal, 2011, **5**(4): 459-468. https://doi.org/10.3109/17435390.2010.516026

[25] Bednarski M, Dudek M, Knutelska J, *et al*. The influence of the route of administration of gold nanoparticles on their tissue distribution and basic biochemical parameters: in vivo studies. Journal of Pharmacol Reports, 2015, **67**(3): 405-409. https://doi.org/10.1016/j.pharep.2014.10.019

[26] Rahmatolahzadeh R , Hamadanian M , Shagholani H , *et al*. Synthesis of Au/SiO2 Nanoparticles with Highly Porous Structure as a pH-Sensitive Targeting Drug Carrier. Iranian Journal of Pharmaceutical Research, **2017**: 21-24.

[27] Liu X, Zhu C, Xu L, *et al*. Green and Facile Synthesis of Highly Stable Gold Nanoparticles via Hyperbranched Polymer In-Situ Reduction and Their Application in Ag+ Detection and Separation. Polymers, 2018, **10**: 42.

[28] Tang B, Liu J, Fan L, *et al*. Green preparation of gold nanoparticles with, Tremella fuciformis, for surface enhanced Raman scattering sensing. Applied Surface Science, 2017: S0169433217323218.

[29] Yiing F, Vengadesh P, Lik K, *et al*. Curcuma mangga-Mediated Synthesis of Gold Nanoparticles: Characterization, Stability, Cytotoxicity, and Blood Compatibility. Nanomaterials, 2017, **7**: 123.

[30] Farooq A, Ayesha I, Alia N, *et al*. Novel route synthesis of porous and solid gold nanoparticles for investigating their comparative performance as contrast agent in computed tomography scan and effect on liver and kidney function. International Journal of Nanomedicine, 2017, **12**: 1555-1563. https://doi.org/10.2147/IJN.S127996

[31] Hainfeld JF, Slatkin DN, Focella TM, *et al*. Gold nanoparticles: a new X-ray contrast agent. The British Journal of Radiology, 2006, **79**(939): 248-253. https://doi.org/10.1259/bjr/13169882

[32] Jain S, Hirst DG and O'Sullivan JM. Gold nanoparticles as novel agents for cancer therapy. The British Journal of Radiology, 2012, **85**(1010): 101-113. https://doi.org/10.1259/bjr/59448833

[33] Lusic H and Grinstaff MW. Xray-ComputedTomography Contrast Agents. Chemical Reviews, 2013, **113**(3): 1641-1666. https://doi.org/10.1021/cr200358s

[34] Anusha JV, Nambi AB and Subramanian E. In Situ and Ex Situ Immobilization of Nano Gold Particles in Zeolite Framework and a Comparison of Their Photocatalytic Activities. Journal of Inorganic and Organometallic Polymers and Materials, **2017**: 1-12.

Chem Rep, 2019, 1(1): 43-50
DOI: 10.25082/CR.2019.01.005

RESEARCH ARTICLE

Comparison of ethanolic extracts of phytoestrogenic *Dendrolobium lanceolatum* and non-phytoestrogenic *Raphanus sativus* to mediate green syntheses of silver nanoparticles

Kamchan Bamroongnok[1] Arunrat Khmahaengpol[2] Sineenat Siri[1*]

Abstract: Green synthesis of silver nanoparticles (AgNPs) mediated by plant extracts has drawn many research interests due to its simple, cost-effective, and eco-friendly approach. However, the extracts derived from phytoestrogenic plants that produce high phenolic-based compounds exhibiting the estrogenic activity have not yet investigated. This work reported the comparison of ethanolic extracts derived from phytoestogenic *Dendrolobium lanceolatum* and non-phytoestrogenic *Raphanus sativus* to facilitate the green synthesis of AgNPs. The total phenolic content and the reducing activity of *D. lanceolatum* extract were significantly higher than those of *R. sativus* extract. In addition, the formation of AgNPs could detect in the reaction using *D. lanceolatum* extract, but not *R. sativus* extract, as determined by the characteristic surface plasmon resonance peak of AgNPs at 416 nm. The synthesized AgNPs were spherical with an average diameter of 74.60±17.11 nm, which their face-centered cubic structure of silver was confirmed by X-ray diffraction analysis. Moreover, the synthesized AgNPs exhibited the antibacterial activity against both Gram-negative *Escherichia coli* and Gram-positive *Staphylococcus aureus*. The results of this work, thus, suggested the potential uses of phytoestrogenic plants as a good source of reducing and stabilizing agents for the production of AgNPs and other metallic nanoparticles.

Keywords: antibacterial activity, phenolic content, plant extract, reducing activity, silver nanoparticles

1 Introduction

Silver nanoparticles (AgNPs) have received many research interests of the scientific community due to their remarkable antibacterial property, which their applications can be seen in various daily commercial products such as textiles, personal cares and food storages.[1] In general, mass production of AgNPs is obtained by using chemical and physical synthesis approaches, which have some drawbacks on a use of hazardous solvents, a generation of toxic by-products and a requirement of high energy.[2] Green synthesis of AgNPs, therefore, has drawn a lot of interests as an alternative eco-friendly and cost-effective approach. A green synthesis refers to a method that reduces or eliminates a use or generation of hazardous substances in reaction processes. In general, it involves the use of less dangerous and low environmental-toxic capping substances, reducing agents and solvents. By this method, the use of natural biomolecules as an alternative reducing and capping agents has received increasing interest for green production of AgNPs. These natural biomolecules include polysaccharides,[3] proteins,[4] and phytochemicals.[5] In addition, green synthesis of nanoparticles can be carried out by living organisms such as bacteria, yeasts and fungi.[6]

In the past few years, plant extracts have been received many research interests for green production of AgNPs, due to the simple and cost-effective process. Phytochemicals and biomolecules in plant extracts can facilitate the formation and stabilization of zero valence silver.[7] Many works reported on the uses of plant extracts derived from many species and various parts of plants for the green synthesis of AgNPs including leaf, latex, stem, root and fruit of edible, ornamental and medicinal plants. The examples were holy basil (*Ocimum sanctum*),[8] garlic (*Allium sativum*),[9] bamboo (*Bambusa arundinacea* and *Bambusa nutans*),[10] *Acalypha hispida*,[11] *Verbesina encelioides*,[12] red ball snake gourd (*Trichosanthes tricuspidata*)[13] and bitter melon (*Mo-*

Received: March 25, 2019 **Accepted:** April 8, 2019 **Published:** April 10, 2019

*Correspondence to: Sineenat Siri, School of Biology, Institute of Science, Suranaree University of Technology, Nakhon Ratchasima 30000, Thailand; Email: ssinee@sut.ac.th
[1] School of Biology, Institute of Science, Suranaree University of Technology, Nakhon Ratchasima 30000, Thailand.
[2] Curriculum and Instruction Program, Faculty of Education, Sakon Nakhon Rajabhat University, Sakon Nakhon 47000, Thailand.

Citation: Bamroongnok K, Khmahaengpol A and Siri S. Comparison of ethanolic extracts of phytoestrogenic *Dendrolobium lanceolatum* and non-phytoestrogenic *Raphanus sativus* to mediate green syntheses of silver nanoparticles. *Chem Rep*, 2019, **1**(1): 43-50.

mordica charantia).[14] The phytochemicals in these plant extracts, such as alkaloids, tannins, phenolics, saponins, terpenoids, proteins, vitamins and polysaccharides, were proposed to serve as reducing agents, while the complex molecules could assist a stabilization of the synthesized AgNPs.[15]

One interesting group of plants that can be an excellent source of active reducing and stabilizing agents for green synthesis of AgNPs is phytoestrogenic plants, which their active biomolecules are phytoestrogens, the phenolic containing phytochemicals with estrogenic agonists and/or antagonists in animals and human that have been used in many food supplements and cosmetic products.[16] Phytoestrogens are divided into three major classes; coumestans, prenylflavonoids and isoflavones. They have the chemical structure, especially phenolic ring and hydroxylation pattern, similar to estrogen, thus providing high affinity for binding to estrogen receptors.[17] Due to the high contents of phenolic compounds in phytoestrogenic plants, whether they exhibit greater activity to facilitate synthesis of AgNPs has been not investigated and compared with the non-phytoestrogenic plants. In Thailand, the dried root of *Dendrolobium lanceolatum*, the flowering plant in the legume family, is commonly used for the folkloric treatment of diuretic and urinary diseases. Our preliminary result revealed that its ethanolic extract exhibited a high estrogenic activity as determined by a yeast two-hybrid system. Thus, in this work, we studied the use of the root extract of *D. lanceolatum* to mediate a green synthesis of AgNPs. In addition, the white radish (*Raphanus sativus*) that contains no phytoestrogenic activity was also used as the comparison.

2 Materials and methods

2.1 Chemicals

Folin-Ciocalteu reagent and gallic acid were obtained from Sigma-Aldrich (St. Louis, MO, USA). Silver nitrate was purchased from QRC chemical (Auckland, New Zealand). All chemicals used were of analytical grade.

2.2 Preparation of plant extracts

Tuberous roots of *D. lanceolatum* (phytoestrogenic plant) and *R. sativus* (non-phytoestrogensic plant) were purchased from a local market in Nakhon Ratchasima, Thailand. Samples were sliced in small pieces and dried in a hot-air oven at 70°C. The dried samples were extracted with 80% ethanol at a ratio of 1:10 (w/v) in a shaker at 80 rpm at ambient temperature for 3 days. After passing through a Whatman No. 1 filter paper, the evaporation of the extract was at 60 °C in a rotary evaporator. Crude plant extracts were kept in a tightly-capped tube and stored at -70°C.

2.3 Total phenolic assay

The total phenolic content (TPC) was determined by the Folin-Ciocalteu assay with some modifications.[18] Briefly, 50 μL of each plant extract (31.25-500 mg/L) or the standard solution of gallic acid (1-500 μg/mL) were mixed with 750 μL of 20% sodium carbonate, 250 μL of 1 M Folin-Ciocalteu reagent and 3.95 mL of distilled water. A reagent blank was used the distilled water instead of the plant extract. The mixture was incubated at 50 °C for 2 h with light protection. The absorbance against the reagent blank was measured at 765 nm using an UV-Visible Specord® 250 Plus spectrophotometer (Analytik-Jena, Jena, Germany). The TPC was expressed as milligram gallic acid equivalent per gram of dried plant extract (mg GAE/g dry weight).

2.4 Reducing activity assay

The reducing activity of the plant extracts was determined using the slightly modified method from the previous publication[19] . The *D. lanceolatum* extract (2.5 mL) of various concentrations (0-1 mg/mL) was mixed with 2.5 mL of 200 mM sodium phosphate buffer (pH 6.6) and 2.5 mL of 1% potassium ferricyanide. The mixture was incubated at 50 °C for 20 min. After adding 2.5 mL of 10% trichloroacetic acid (w/v), the mixture was centrifuged at 3000 ×g for 10 min. The upper layer of the solution (1.25 mL) was removed to a new tube before mixing with distilled water (1.25 mL) and a freshly prepared 0.1% ferric chloride (0.25 mL). The reducing power of the tested samples was evaluated by the color changes and the measured absorbance at 700 nm. All determinations were from five replications and the results were expressed as mean±standard deviation.

2.5 Synthesis and characterization of AgNPs

The reaction (10 mL) to synthesize AgNPs contained 8.6 mL of 200 mg/mL plant extract (D. lanceolatum or R. sativus) and 1.4 mL of 300 mM silver nitrate. The reaction was carried out at 60 °C with the light protection for 24 h. The formation of AgNPs was monitored from the reaction color change to dark brown and the presence of the characteristic surface plasmon resonance (SPR) peak of silver by measuring the absorbance at the wavelengths of 300-900 nm. The reactions containing silver nitrate and various concentrations (20-200 mg/mL) of D. lanceolatum extract were carried out at 60 °C at 12

h to study the effect of the extract concentrations. In addition, to study the effect of reaction times, the formation of AgNPs was monitored in a time course of 48 h, which the reactions contained silver nitrate and the plant extract (200 mg/mL) and incubated at 60°C.

To determine their crystalline structure, the synthesized AgNPs were subjected to X-ray diffraction (XRD; Bruker, Bremen, Germany) analysis using D8 Advance diffractometer with Cu Kα radiation, λ=1.54 $\mathring{A}$ in the 2θ range of 30°-80°. The instrument was calibrated by using the lanthanum hexaboride (LaB_6) before analysis.

The morphology and size of AgNPs were determined from the taken scanning electron microscope (SEM) images using a JSM 7800F SEM (JEOL, Tokyo, Japan) provided with a Schottky type field emission and lower electron detector at an accelerating voltage of 15 kV. The suspension of AgNPs was dropped on a carbon tape, allowed to completely dry at room temperature and sputter-coated with gold immediately before observing. An average diameter of AgNPs was determined from the SEM images at random locations (n=300) using the ImageJ open-access software.[20]

2.6 Antibacterial Assay

The antibacterial activity of the produced AgNPs against bacteria was evaluated by the minimum inhibitory concentration (MIC) and the minimum bactericidal concentration (MBC). The representative Gram-negative and Gram-positive bacteria in this work were Escherichia coli (ATCC 25922) and Staphylococcus aureus (ATCC 25923), respectively. The MIC referred to the minimum concentration of AgNPs that inhibited bacterial growth. The MBC referred to the minimum concentration of AgNPs that completely killed the bacteria. The stock suspension of AgNPs was serially two-fold diluted by Mueller-Hinton (MH) broth (0.81-26.0 μg/mL) and incubated with the tested bacteria at a concentration of 5×10^5 colony-forming units/mL (CFU/mL) at 37 °C for 24 h. The bacterial growth was measured by the optical density at 600 nm to determine the MIC. To determine the MBC, the cultures (100 μL) at MIC and two above concentrations were cultured on MH-agar plates at 37°C for 24 h. The MBC was determined by the concentration of AgNPs showing no bacterial growth on the culture plate.[21]

2.7 Statistical analysis

The statistical analysis of two data groups was performed using the independent-samples t-test. The analysis of more than two data groups was performed using the one-way analysis of variance (ANOVA) with SPSS 18.0 for Windows software (SPSS Inc., Chicago, Illinois, USA). The multiple comparisons among data groups were analyzed by Tukey's honest significant test. The significant difference among groups was considered at a level of $P<0.05$.

3 Results and Discussion

3.1 Total phenolic content and reducing activity of the plant extracts

The tuberous roots of *D. lanceolatum* (phytoestrogenic plant) and *R. sativus* (non-phytoestrogenic plant) were extracted in 80% ethanol, which their extraction yields were 1.00±0.01 and 5.10±0.01 g/100g dried weight of the plants, respectively. The total phenolic contents (TPC) of the plant extracts are shown in Figure 1A. The TPC of the *D. lanceolatum* extract was 423.3±19.3 mg GAE/g dry weight, which was approximately 14.7 folds higher than that of the *R. sativus* extract (28.8±3.6 mg GAE/g dry weight). The major phenolic compounds of the *D. lanceolatum* extract, especially ones possessing phytoestrogenic activity, are likely in the groups of prenylflavonoids and dibenzocycloheptene derivatives.[22]

The reducing activities of *D. lanceolatum* and *R. sativus* extracts are shown in Figure 1B, which both extracts exhibited the reducing activity in a dose-dependent manner. However, the reducing activity of the *D. lanceolatum* extract was significantly higher than that of the *R. sativus* extract. At the concentration of 1 mg/mL, the reducing activity of the *D. lanceolatum* extract was approximately 3.4 folds higher than that of the *R. sativus* extract, well corresponding to the different TPCs of both plant extracts. It is likely that the hydroxyl groups of the phenolic compounds of these plant extracts may play a crucial role as the radical scavengers.[23] Thus, they exhibited the reducing activity but at different levels according to their phenolic compound contents.

3.2 Synthesis and characterization of AgNPs

The *D. lanceolatum* and *R. sativus* extracts were used to synthesize AgNPs by incubating with silver nitrate at 60°C for 24 h without the addition of other chemical reducing and stabilizing agents. The UV-Vis spectra of the reactions are shown in Figure 2. The color of the reaction changing from orange to dark brown color suggested the formation of AgNPs. In addition, the presence of synthesized AgNPs was determined by the characteristic surface plasmon resonance (SPR) peak of AgNPs at 416 nm.[24] In this reaction, it is likely that the phenolic compounds of the *D. lanceolatum* extract serving as the reducing agents to reduce Ag^+ into Ag^0 and eventually

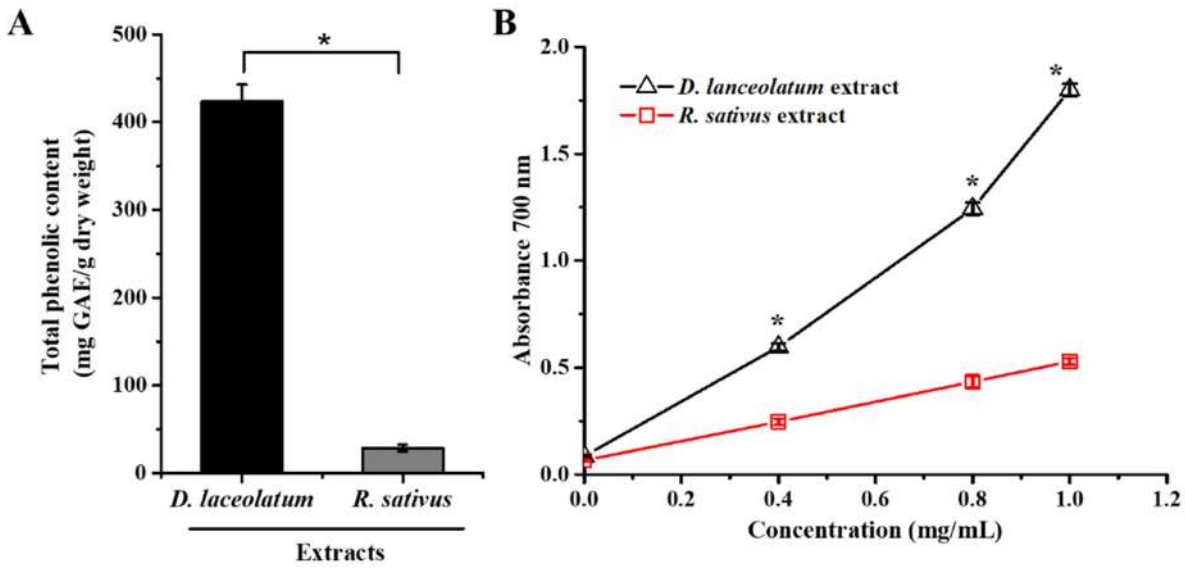

Figure 1. The total phenolic contents (A) and the reducing activities (B) of the *D. lanceolatum* and *R. sativus* extracts

form AgNPs, while the complex structure of proteins and carbohydrates of the extract assists the stabilization of colloidal AgNPs in an aqueous environment.[25] In contrast to, this characteristic SPR peak was not detected in the reaction containing the *R. sativus* extract, suggesting that the *R. sativus* extract was unable to promote the synthesis of AgNPs at this condition. It was noted that the presence of the absorption peak at 350 nm of both reactions was probably due to the absorption of phenolic compounds of the extracts.[26]

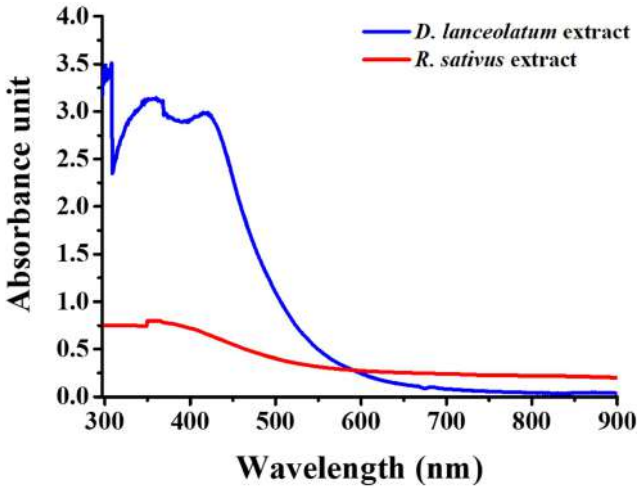

Figure 2. Different UV-Vis spectra of the reactions to synthesize AgNPs that were mediated by *D. lanceolatum* and *R. sativus* extracts

The effects of the concentration of *D. lanceolatum* extract and the reaction time on the synthesis of AgNPs were also studied. The UV-Vis spectra of the reactions containing various concentrations (20-200 mg/mL) of the *D. lanceolatum* extract at 12 h of incubation are shown in Figure 3A. The formation of AgNPs as indicated by the characteristic SPR peak was observed only in the reactions containing 100 and 200 mg/mL of *D. lanceolatum* extract. The SPR peak intensity was increased according to the increased concentrations of *D. lanceolatum* extract, suggesting that the formation of AgNPs depended on the concentration of the extract. The phenolic compounds of the *D. lanceolatum* extract might play the significant role to reduce Ag^{+} to Ag^{0} for a formation of silver nuclei via the protein and electron transfer mechanisms as well as to stabilize the antioxidant molecules in the reaction. In addition, the phenolic compounds could facilitate the growth of AgNPs via the binding to the silver clusters and assist the reduction of silver ions at the surface of the clusters to form AgNPs.[27]

In addition, the effect of the reaction time on the synthesis of AgNPs was studied. The formation of AgNPs in the reaction containing the *D. lanceolatum* extract (200 mg/mL) was monitored in a time course of 48 h (Figure 3B). The formation of AgNPs was detected in the reactions at 12-48 h as determined by the characteristic SPR peak of AgNPs and the changes of reaction color (light yellow to dark brown). The production yield of AgNPs in a time course of 48 h was increased in a dose-dependence as indicated by the SPR peak intensity.

The shape and size of the synthesized AgNPs were determined by the taken SEM images. Figure 4A shows the representative SEM image revealing the spherical morphology of the synthesized AgNPs. The diameters

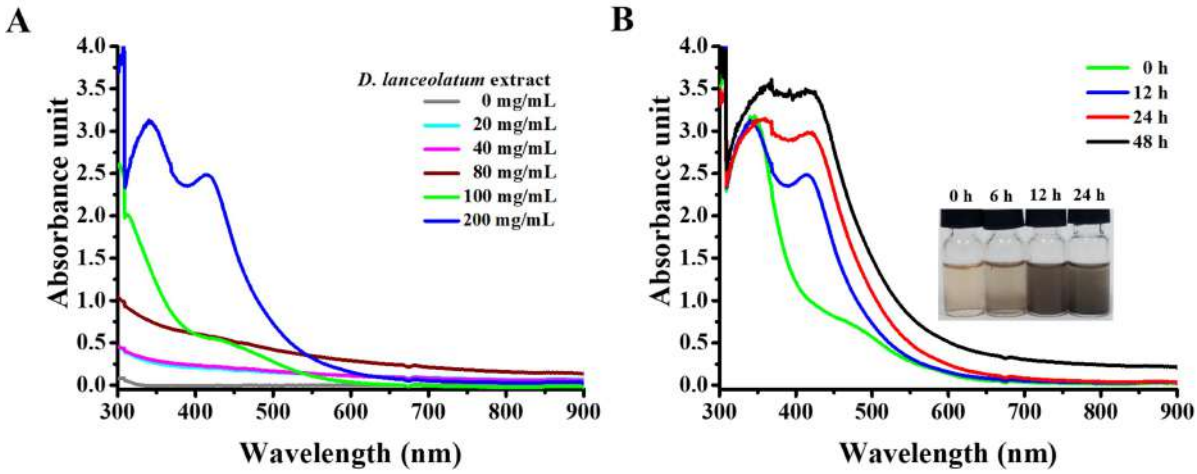

Figure 3. The UV-Vis spectra of the formation of AgNPs using different concentrations of *D. lanceolatum* extract (A) and different reaction times (B)

of 300 particles, randomly picked, were in a range of 40.8-134.0 nm (Figure 4B), which their average size was 74.60±17.11 nm. Although the formation of spherical AgNPs has not fully understood, it speculates that the binding between Ag^+ and biomolecules derived from the *D. lanceolatum* extract leads to isotropic growth of the silver clusters and formation of spherical nanoparticles.[28]

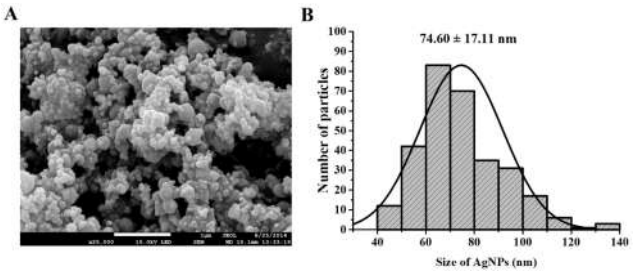

Figure 4. The representative SEM image (A) and the histogram of size distribution (B) of the synthesized AgNPs

In Figure 5, the XRD pattern shows the numbers of Bragg reflections with 2 theta values of 38.11°, 44.30°, 64.44° and 77.39° corresponding to the (111), (200), (220) and (311) lattice planes, indicating the face-centered cubic structure (fcc) of silver according to the JCPDS file No. 03-065-287.[29] Two unassigned peaks observed in the XRD pattern were likely the crystallization of bioorganic phases derived from the plant extract that occurred on the surface of the nanoparticles.[30]

3.3 Antibacterial Activity

The antibacterial activity of the synthesized AgNPs mediated by the *D. lanceolatum* extract was determined by a microbroth dilution method against the representative Gram-negative *E. coli* and Gram-positive *S. aureus*. The growths of both bacterial strains in response to various concentrations of AgNPs was monitored in a time course of 24 h. As seen in Figure 6, AgNPs exhibited the antibacterial activity against both bacterial strains in a dose-dependent response, which the increased concentrations of AgNPs resulted in more growth reduction of both bacterial strains. The minimal concentrations of AgNPs causing the inhibition of the *E. coli* and *S. aureus* growths (MICs) were equally at 6.5 μg/mL. The minimal concentrations of AgNPs that completely killed the bacteria (MBCs) were higher than the MICs, which the MBCs of AgNPs against *E. coli* and *S. aureus* were 13.0 and 26.0 μg/mL, respectively. The less susceptibility of *S. aureus* to AgNPs as compared with *E. coli* was reported to relate to the thicker peptidoglycan layer of

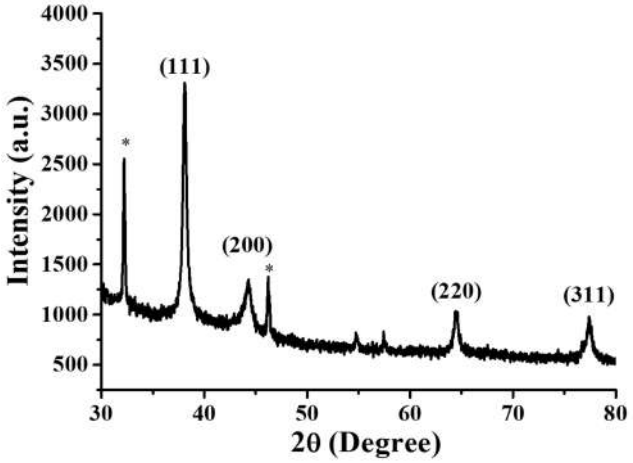

Figure 5. XRD analysis of the synthesized AgNPs. Unassigned peaks indicated as *

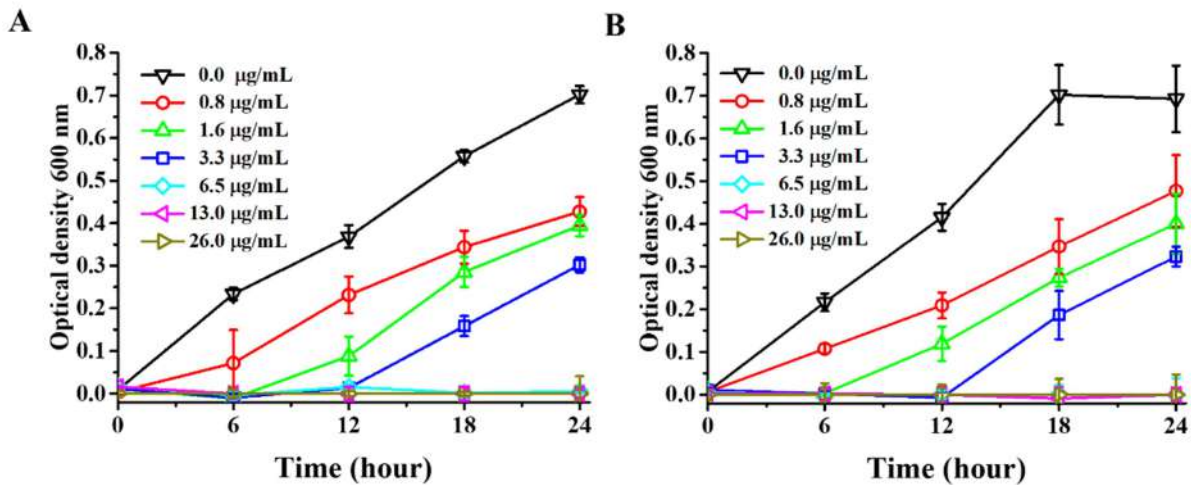

Figure 6. The growth curves of *E. coli* (A) and *S. aureus* (B) in response to different concentrations of AgNPs in a time course of 24 h

the Gram-positive bacteria.[31] The penetration of AgNPs inside the bacterial cells is proposed via direct diffusion and endocytosis, depending on their sizes.[32] AgNPs with the diameters in a range of 10-100 nm can enter the cells via the endocytosis mechanism, while AgNPs of less than 10 nm prefer to penetrate the cell wall via direct diffusion since their lower adhesion and stretching energy are not sufficient for endocytosis.[33] The penetrated AgNPs can disrupt bacterial enzyme function, interfere DNA transcription, interrupt DNA replication and eventually cause cell death.[34] In addition, some AgNPs attached on the cell surface can damage and disrupt the cell permeability and respiration as well as cause a formation of reactive oxygen species (ROS) in bacterial cells.[35]

4 Conclusion

This work demonstrated that the extract derived from phytoestrogenic *D. lanceolatum* actively induced the formation of AgNPs as its biomolecules, especially phenolic compounds, served as the reducing agents and the complex structural compounds stabilized the formed AgNPs. In comparison with the extract derived from the non-phytoestrogenic *R. sativus*, at the same condition, no formation of AgNPs was detected as determined by the presence of the characteristic SPR peak of AgNPs, which was likely due to the less TPC and reducing activity of the *R. sativus* extract. The synthesized AgNPs were spherical with an average diameter of 74.60±17.11 nm. The identity of the synthesized particles was confirmed by XRD analysis, which the crystalline structure of the synthesized particles was the face-centered cubic geometry of silver. The produced AgNPs exhibited the antibacterial activity against both *E. coli* and *S. aureus*. However, *E. coli* was more susceptible to AgNPs than *S. aureus* as indicated by the MBCs, well corresponding to the different thickness of their cell walls.

Acknowledgement

This work is supported by Suranaree University of Technology (SUT1-104-57-24-20).

References

[1] Chen Y, Fan Z, Zhang Z, *et al*. Two-dimensional metal nanomaterials: synthesis, properties, and applications. Chemical Reviews, 2018, **118**(13): 6409-6455. https://doi.org/10.1021/acs.chemrev.7b00727

[2] Iravani S, Korbekandi H, Mirmohammadi S, *et al*. Synthesis of silver nanoparticles: chemical, physical and biological methods. Research in Pharmaceutical Sciences, 2014, **9**(6): 385-406.

[3] Huang H and Yang X. Synthesis of polysaccharide-stabilized gold and silver nanoparticles: a green method. Carbohydrate Research, 2004, **339**(15): 2627-2631. https://dx.doi.org/10.1016/j.carres.2004.08.005

[4] Murawala P, Phadnis SM, Bhonde RR, *et al*. In situ synthesis of water dispersible bovine serum albumin capped gold and silver nanoparticles and their cytocompatibility studies. Colloids & Surfaces B Biointerfaces, 2009, **73**(2): 224-228. https://dx.doi.org/10.1016/j.colsurfb.2009.05.029

[5] Shankar SS, Rai A, Ahmad A, *et al*. Rapid synthesis of Au, Ag, and bimetallic Au coreAg shell nanoparticles using Neem (Azadirachta indica) leaf broth. Journal of Colloid and Interface Science, 2004, **275**(2): 496-502. https://dx.doi.org/10.1016/j.jcis.2004.03.003

[6] Thakkar KN, Mhatre SS and Parikh RY. Biological synthesis of metallic nanoparticles. Nanomedicine, 2010, **6**(2): 257-262. https://dx.doi.org/10.1016/j.nano.2009.07.002

[7] Jafari A, Pourakbar L, Farhadi K, *et al*. Biological synthesis of silver nanoparticles and evaluation of antibacterial

and antifungal properties of silver and copper nanoparticles. Turkish Journal of Biology, 2015, **39**(4): 556-561. https://doi.org/10.3906/biy-1406-81

[8] Brahmachari G, Sarkar S, Ghosh R, *et al*. Sunlight-induced rapid and efficient biogenic synthesis of silver nanoparticles using aqueous leaf extract of Ocimum sanctum Linn. with enhanced antibacterial activity. Bioorganic and Medicinal Chemistry Letters, 2014, **4**(1): 1-10. https://dx.doi.org/10.1186/s13588-014-0018-6

[9] Ahamed M, Khan MAM, Siddiqui MKJ, *et al*. Green synthesis, characterization and evaluation of biocompatibility of silver nanoparticles. Physica E, 2011, **43**(6): 1266-1271. https://dx.doi.org/10.1016/j.physe.2011.02.014

[10] Kalaiarasi K, Prasannaraj G, Sahi SV, *et al*. Phytofabrication of biomolecule-coated metallic silver nanoparticles using leaf extracts of in vitro-raised bamboo species and its anticancer activity against human PC3 cell lines. Turkish Journal of Biology, 2015, **39**(2): 223-232. https://doi.org/10.3906/biy-1406-10

[11] Sithara R, Selvakumar P, Arun C, *et al*. Economical synthesis of silver nanoparticles using leaf extract of Acalypha hispida and its application in the detection of Mn(II) ions. Journal of Advanced Research, 2017, **8**(6): 561-568. https://doi.org/10.1016/j.jare.2017.07.001

[12] Bhati-Kushwaha H and Malik CP. Biopotential of Verbesina encelioides (stem and leaf powders) in silver nanoparticle fabrication. Turkish Journal of Biology, 2013, **37**(6): 645-654. https://doi.org/10.3906/biy-1212-7

[13] Yuvarajan R, Natarajan D, Ragavendran C, *et al*. Photoscopic characterization of green synthesized silver nanoparticles from Trichosanthes tricuspidata and its antibacterial potential. Journal of Photochemistry and Photobiology B: Biology, 2015, **149**: 300-307. https://dx.doi.org/10.1016/j.jphotobiol.2015.04.032

[14] Ajitha B, Reddy YAK and Reddy PS. Biosynthesis of silver nanoparticles using Momordica charantia leaf broth: evaluation of their innate antimicrobial and catalytic activities. Journal of Photochemistry and Photobiology B: Biology, 2015, **146**: 1-9. https://dx.doi.org/10.1016/j.jphotobiol.2015.02.017

[15] Koduru JR, Kailasa SK, Bhamore JR, *et al*. Phytochemical-assisted synthetic approaches for silver nanoparticles antimicrobial applications: A review. Advances in Colloid and Interface Science, 2018, **256**: 326-339. https://doi.org/10.1016/j.cis.2018.03.001

[16] Albertazzi P and Purdie DW. The nature and utility of the phytoestrogens: a review of the evidence. Maturitas, 2002, **42**(3): 173-185. https://dx.doi.org/10.1016/S0378-5122(02)00024-5

[17] Raheja S, Girdhar A, Lather V, *et al*. Biochanin A: A phytoestrogen with therapeutic potential. Trends in Food Science and Technology, 2018, **79**: 55-66. https://doi.org/10.1016/j.tifs.2018.07.001

[18] Martins S, Aguilar CN, Teixeira JA, *et al*. Bioactive compounds (phytoestrogens) recovery from Larrea tridentata leaves by solvents extraction. Separation and Purification Technology, 2012, **88**: 163-167. https://dx.doi.org/10.1016/j.seppur.2011.12.020

[19] Özkan A, Gübbük H, Güneş E, *et al*. Antioxidant capacity of juice from different papaya (Carica papaya L.) cultivars grown under greenhouse conditions in Turkey. Turkish Journal of Biology, 2011, **35**(5): 619-625.

[20] Schneider CA, Rasband WS and Eliceiri KW. NIH Image to ImageJ: 25 years of image analysis. Nature methods, 2012, **9**(7): 671-675. https://doi.org/10.1038/nmeth.2089

[21] Chen Y, Deng Y, Pu Y, *et al*. One pot preparation of silver nanoparticles decorated TiO2 mesoporous microspheres with enhanced antibacterial activity. Materials Science and Engineering. C, Materials for Biological Applications, 2016, **65**: 27-32. https://dx.doi.org/10.1016/j.msec.2016.04.028

[22] Kanokmedhakul S, Kanokmedhakul K, Nambuddee K, *et al*. New bioactive prenylflavonoids and dibenzocycloheptene derivative from roots of Dendrolobium lanceolatum. Journal of Natural Products, 2004, **67**(6): 968-972. https://doi.org/10.1021/np030519j

[23] Ebrahimzadeh MA, Pourmorad F and Hafezi S. Antioxidant activities of Iranian corn silk. Turkish Journal of Biology, 2008, **32**(1): 43-49.

[24] John J, Aravindakumar C and Thomas S. Green synthesis of silver nanoparticles using phyto-constituents of Ficus auriculata Lour. Scholarena Journal of Biotechnology, 2018, **4**(103): 19-21.

[25] Corciova A and Ivanescu B. Biosynthesis, characterization and therapeutic applications of plant-mediated silver nanoparticles. Journal of the Serbian Chemical Society, 2018, **83**(5): 515-538. https://doi.org/10.2298/JSC170731021C

[26] Vachali PP, Li B, Besch BM, *et al*. Protein-flavonoid interaction studies by a Taylor dispersion surface plasmon resonance (SPR) Technique: A novel method to assess biomolecular interactions. Biosensors, 2016, **6**(1): 6-15. https://doi.org/10.3390/bios6010006

[27] Clarke G, Ting K, Wiart C, *et al*. High correlation of 2,2-diphenyl-1-picrylhydrazyl (DPPH) radical scavenging, ferric reducing activity potential and total phenolics content indicates redundancy in use of all three assays to screen for antioxidant activity of extracts of plants from the Malaysian rainforest. Antioxidants, 2013, **2**(1): 1-10. https://doi.org/10.3390/antiox2010001

[28] Chandran SP, Chaudhary M, Pasricha R, *et al*. Synthesis of gold nanotriangles and silver nanoparticles using Aloevera plant extract. Biotechnology Progress, 2006, **22**(2): 577-583. https://doi.org/10.1021/bp0501423

[29] Andas J and Adam F. One-pot synthesis of nanoscale silver supported biomass-derived silica. Materials Today: Proceedings, 2016, **3**(6): 1345-1350. https://doi.org/10.1016/j.matpr.2016.04.013

[30] Singhal G, Bhavesh R, Kasariya K, *et al*. Biosynthesis of silver nanoparticles using Ocimum sanctum (Tulsi) leaf extract and screening its antimicrobial activity. Journal of Nanoparticle Research, 2011, **13**(7): 2981-2988. https://doi.org/10.1007/s11051-010-0193-y

[31] Jokar M, Rahman RA, Ibrahim NA, *et al*. Melt production and antimicrobial efficiency of low-density polyethylene (LDPE)-silver nanocomposite film. Food and Bioprocess Technology, 2012, **5**(2): 719-728. https://doi.org/10.1007/s11947-010-0329-1

[32] Leroueil PR, Hong S, Mecke A, *et al*. Nanoparticle interaction with biological membranes: does nanotechnology present a janus face? Accounts of Chemical Research, 2007, **40**(5): 335-342. https://doi.org/10.1021/ar600012y

[33] Rajendran L, Knlker HJ and Simons K. Subcellular targeting strategies for drug design and delivery. Nature Reviews Drug Discovery, 2010, **9**: 29-42. https://doi.org/10.1038/nrd2897

[34] Raffi M, Hussain F, Bhatti T, *et al*. Antibacterial characterization of silver nanoparticles against E. coli ATCC-15224. Journal of Materials Science and Technology, 2008, **24**(2): 192-196.

[35] Morones JR, Elechiguerra JL, Camacho A, *et al*. The bactericidal effect of silver nanoparticles. Nanotechnology, 2005, **16**(10): 2346-2353. https://doi.org/10.1088/0957-4484/16/10/059

Chemical Reports is an
independent open access journal published
by Syncsci Publishing. Pte. Ltd.

Syncsci Publishing. Pte. Ltd.
50 Chin Swee Road
#09-04 Thong Chai Bldg
Singapore 169874
Tel : (+65) 68264112; (+65)98107233
Email : editorial@syncsci.com
Website: www.syncsci.com

ISSN 2591-7943

9 772591 794316 01

Print Version USD 75.00